Investigation of tropical climate variations in the Indian Ocean based on the transfer routes of wave energy

（波エネルギーの伝達経路に基づくインド洋の熱帯気候変動の考察）

LI, Zimeng

（李 梓萌）

A dissertation for the degree of Doctor of Science

Department of Earth and Environmental Sciences,

Graduate School of Environmental Studies, Nagoya University

（名古屋大学大学院環境学研究科地球環境科学専攻学位論文　博士（理学））

2023

Abstract

In traditional atmosphere-ocean research, when analyzing the role of large-scale waves, the tropical-subtropical interactions cannot be examined on a unified metric. This is because the equatorial dynamics and mid-latitude dynamics have been formulated in separate systems. In order to find a solution to this problem, a new scheme was recently derived that can seamlessly diagnose the energy cycle without the limitation of latitudinal zones. In this study, as the first application of this scheme, I investigated wind-driven surface wave dynamics in the Indian Ocean (IO) on seasonal and interannual scales.

Concerning seasonal variations in the IO, chapters 2 and 3 illustrate the transfer routes of wave energy in the surface and deep layers, respectively. Chapter 2 provides a new perspective for the life-cycle of annual waves in the IO through the wave energy cycle. The well-defined circulation routes of wave energy demonstrate that Kelvin waves (KWs) and Rossby waves (RWs) interconnect at the zonal boundaries of the IO. This study identifies two sets of cyclonic circulations of wave energy in each hemisphere based on an annual-mean analysis. The first of these represents a localized cyclonic circulation close to the African coasts, while the other is a large-scale cyclonic circulation over the eastern IO. For the wave energy transfer event, it is effective to analyze the energy flux calculated by the new scheme applying the Hovmöller diagrams at the equator. Focusing on the second baroclinic mode, the eastward transfer of wave energy associated with equatorial KWs appears four times a year. This corresponds to westerly winds generated KWs and monsoonal winds generated KWs appearing on the ocean surface layer twice a year in the equatorial IO, respectively.
Chapter 3 applies a new diagnostic scheme for the vertical transfer of wave energy and examined the effects from the surface layer to the intermediate and deep layers. As an example, this study focuses on the southern Bay of Bengal where the wave energy reaches the deepest point in the IO, and examines its image and origin. The spatio-temporal

distribution of the energy flux reveals the different timing of the peak at the equator in the surface and intermediate layers. In the surface layer, the amplitude of the equatorial KWs maximizes in May, while in the intermediate layer, maximized in August. The southwesterly monsoon winds trigger the coastal KWs in the Arabian Sea, which wrap around the mid-depth layer from the western IO coast to the equatorial layer. These mid-depth equatorial KW packets subsequently arrive at the eastern boundary of the IO and are diffracted poleward, carrying energy downwards in November and December in the southern Bay of Bengal. The vertical structure of equatorial and off-equatorial waves can be treated continuously is the advantage of this study.

The objective of chapter 4 is to reinforce our understanding of interannual variability in the tropical IO through the perspective of the wave energy cycle. This study has conducted a set of 61-year hindcast experiments to examine the mechanism of a remarkable positive IO dipole event that occurred in 1994. Two sets of westward transfer episodes in the energy flux associated with RWs are identified along the equator during 1994. This chapter focuses on the image and origin of these RWs. One set represents the same phase speed as the linear theory of equatorial RWs. This set of RWs originates from the reflection of the equatorial KWs on the eastern side of the IO. The second set of westward energy flux is slightly slower than the theoretical phase speed. The appearance of the slower group velocity of westward energy flux is found to be associated with off-equatorial RWs generated by southeasterly winds in the southeastern IO. This study considers an empirical orthogonal function (EOF) analysis to combine the time series of energy-flux streamfunction and potential. The first EOF mode reveals the intense westward signals of energy flux are attributed to off-equatorial RWs associated with predominant wind input in the southeastern IO. This kind of characteristic distribution can be viewed as the dominant dynamic factor in a positive IOD event.

This study has examined the seasonal and interannual variabilities in the tropical Indian Ocean through a new perspective of the wave energy cycle. The diagnostic procedures in this study can be used to improve our understanding of dynamical processes not only in the IO but also in the Pacific and Atlantic Oceans.

Contents

List of Tables

List of Figures

Abbreviations

EACC	East African Coast Current
ECMWF ERA-40	European Centre for Medium-Range Weather Forecasts Re-analysis
ENSO	El Niño-Southern Oscillation
EOF	Empirical orthogonal function
GEBCO	General Bathymetric Chart of the Oceans
IGWs	inertia-gravity waves
IO	Indian Ocean
JRA55	Japanese 55-year Reanalysis
KWs	Kelvin waves
NMC	North Monsoon Current
OGCM	Ocean General Circulation Model
OFES	OGCM For the Earth Simulator
ORAS3	Ocean Reanalysis series 3
PF	pressure flux
RWs	Rossby waves
RGWs	Rossby-gravity waves
SBoB	southern Bay of Bengal
SC	Somali Current
SEC	South Equatorial Current
SECC	South Equatorial Counter Current
SGS	subgrid-scale
SSH	sea surface height
SST	sea surface temperature

Chapter 1 General Introduction

1.1 Background of the Indian Ocean

Major oscillations in the Indian Ocean (IO) are attributed to seasonal monsoon (Schott and McCreary, 2001). During the boreal winter monsoon, northeasterly winds in the Arabian Sea and the Bay of Bengal induce the North Monsoon Current (NMC) which flows westward that feeds a southward flow, called the Somali Current (SC) along the African coasts. This southward flowing boundary current meets the northward flowing East African Coast Current (EACC) in equatorial regions around 2–4°S. These currents in both hemispheres converge and furnish the South Equatorial Counter Current (SECC) that flows eastward along the equator (Düing and Schott, 1978; Swallow *et al.,* 1991; Schott and McCreary, 2001; Beal *et al.,* 2013). During the boreal summer monsoon, southwesterly winds in the Arabian Sea induce a strong northward EACC that originated from the South Equatorial Current (SEC) along the African coasts. As the EACC crosses the equator, a portion of it turns offshore and starts to flow eastward at about 4°N towards the Bay of Bengal (Schott and McCreary, 2001; Nagura and Masumoto, 2015). At the equator, westerly winds in spring and fall cause semi-annual appearance of Wyrtki (1973) jet as well as equatorial KWs which propagate eastward.

An important coupled atmosphere-ocean phenomenon, the IO Dipole (IOD, Saji *et al.*, 1999) plays a crucial role in the climate changes of countries that surrounding the IO by changing the temperature pattern loading on the western and eastern pole of the IO. During IOD positive phases, the warm water covers the western regions with thermocline deepening and the cool water dominates in the south-eastern regions with thermocline shallowing triggered by the southeasterly winds, leading to the heavy precipitation in African coasts and severe drought over Australia continents. IOD negative phases are excited by the westerly

winds along the equator, which show the opposite pattern of sea surface temperature than that of positive phases. This could result in the severe drought over western IO and heavy rainfall in eastern IO. The IOD is the unique inherent coupled atmosphere-ocean phenomenon in the IO. It is well known that the IO is adjacent to the Pacific Ocean, the transfer signals of Indonesian Throughflow along the Indonesian Archipelago travel poleward and radiate into the southern IO (Cai *et al.,* 2005) associated with Rossby waves (RWs), referred to as interpretation for the energy transmission from the Pacific Ocean to the IO. The IOD also has a link with the El Niño-Southern Oscillation (ENSO) through Indonesian Throughflow.

The mechanism of tropical climate variations is closely linked to the characteristics of equatorial Kelvin waves (KWs) and RWs (Mark and Huang, 2004; Rahul *et al.,* 2004; Yamagata *et al.,* 2004; Nagura and McPhaden, 2010; Rao *et al.,* 2010; Ishizaki *et al.,* 2014; Delman *et al.,* 2016). These synoptic-scale waves in the atmosphere-ocean system play an important role in the development, termination, and teleconnection of the phenomena, such as Madden-Julian Oscillation, ENSO, and IOD. In order to improve the climate prediction, it is relevant to investigate how these waves are linked to each other and where these waves originate from, without being bothered by the difference of tropical and subtropical dynamics.

1.2 Schemes for tracing the transfer routes of wave energy

There are at least three existing schemes for diagnosing the geographical transfer routes of wave energy. Here we explain three schemes, the pressure flux scheme (Cummins and Oey, 1997), the Orlanski and Sheldon (1993, hereafter OS93) scheme, and the Aiki *et al.* (2017, hereafter AGC17) scheme that have been proposed for diagnosing the group-velocity-based transfer routes of wave energy.

Wave energy $E^{(n)}$ for the n-th baroclinic mode may be defined as,

$$E^{(n)} \equiv \rho_0 \left[u^{(n)2} + v^{(n)2} + (p^{(n)}/c^{(n)})^2 \right]/2, \tag{1.1a}$$

where $u^{(n)}$ and $v^{(n)}$ indicate the zonal and meridional components of velocity, respectively, and $p^{(n)}$ is geopotential. The symbols ρ_0 and $c^{(n)}$are constants for the reference density of seawater and nonrotating gravity wave speed, respectively. An equation for the development of wave energy may be derived using (1.1a)–(1.1c) to yield,

$$\partial_t \overline{E^{(n)}} + \rho_0 \nabla \cdot \ll \overline{u^{(n)} p^{(n)}}, \overline{v^{(n)} p^{(n)}} \gg = S_{in} + S_{dis}, \tag{1.1b}$$

where $\nabla \cdot \ll A, B \gg = \partial_x A + \partial_y B$ is the horizontal divergence operator (A and B are arbitrary quantities). The overbar denotes a phase average. The horizontal coordinates x and y increase eastward and northward, respectively. Energy input by wind forcing is written as

$$S_{in} = \frac{\alpha^{(n)}}{\sqrt{H_{mix} H_{bottom}}} \left(\overline{u^{(n)} \tau^x_{wind}} + \overline{v^{(n)} \tau^y_{wind}} \right), \tag{1.1c}$$

where wind stress vector (τ^x_{wind}, τ^y_{wind}) is the seasonal anomaly component of monthly climatology between September 1957 and August 2002 used in chapters 2 and 3 and the interannual anomaly component of monthly winds from 1958–2018 used in chapter 4. Energy dissipation is written as

$$S_{dis} = \rho_0 \left(\overline{u^{(n)} SGS^x} + \overline{v^{(n)} SGS^y} \right), \tag{1.1d}$$

where the subgrid-scale (SGS) terms represent the effect of lateral eddy viscosity based on the Smagorinsky *et al.* (1965) scheme with a nondimensional coefficient of 0.1 after squaring. In our model, the SGS terms have been expressed as

$$SGS^x = \partial_x \left[\kappa (2 u^{(n)}_x) \right] + \partial_y \left[\kappa (u^{(n)}_y + v^{(n)}_x) \right], \tag{1.1e}$$

$$SGS^y = \partial_x \left[\kappa (u^{(n)}_y + v^{(n)}_x) \right] + \partial_y \left[\kappa (2 v^{(n)}_y) \right], \tag{1.1f}$$

where κ is the coefficient of lateral eddy viscosity. Substitution of (1.1e–f) to (1.1d) yields,

$$S_{dis} = S_{dis:div} + S_{dis:nd}, \tag{1.1g}$$

$$S_{dis:div} = \rho_0 \partial_x \left[\overline{2\kappa u^{(n)} (u^{(n)}_x) + \kappa v^{(n)} (u^{(n)}_y + v^{(n)}_x)} \right] + \rho_0 \partial_y \left[\overline{\kappa u^{(n)} (u^{(n)}_y + v^{(n)}_x) + 2\kappa v^{(n)} (v^{(n)}_y)} \right], \tag{1.1h}$$

$$S_{dis:nd} = -\rho_0 \overline{\kappa \left[2 (u^{(n)}_x)^2 + (u^{(n)}_y + v^{(n)}_x)^2 + 2 (v^{(n)}_y)^2 \right]}, \tag{1.1i}$$

where the dissipation term has been separated into the divergent and negative-definite parts.

The expression of energy flux in (1.1b) may be referred to as pressure flux scheme,

$$\ll \overline{u^{(n)}p^{(n)}}, \overline{v^{(n)}p^{(n)}} \gg. \tag{1.2}$$

If applied to the diagnosis of inertia-gravity waves, the pressure flux becomes identical to group velocity times wave energy (Cummins and Oey, 1997). The pressure flux scheme cannot represent the direction of group velocity for mid-latitude RWs.

Without affecting the result of the divergence in the energy budget equation (1.1b), one may add a rotational flux to read,

$$\ll \overline{u^{(n)}p^{(n)}} + \left[\overline{p^{(n)2}}/(2f)\right]_y, \overline{v^{(n)}p^{(n)}} - \left[\overline{p^{(n)2}}/(2f)\right]_x \gg, \tag{1.3}$$

which becomes identical to group velocity times wave energy for mid-latitude RWs.
The expression of the energy flux in (1.3) is referred to as OS93 scheme. The OS93 scheme becomes singular at the equator owing to the Coriolis parameter in the denominator.

AGC17 have derived a seamless expression for the energy flux that can represent the direction of group velocity for both gravity and planetary waves at all latitudes. What they call the level-0 (i.e. exact) version of the AGC energy flux may be written as,

$$\ll \overline{u^{(n)}p^{(n)}} + (\overline{p^{(n)}\varphi^{(n)}}/2 + \overline{u_{tt}^{(n)}\varphi^{(n)}}/\beta)_y, \overline{v^{(n)}p^{(n)}} - (\overline{p^{(n)}\varphi^{(n)}}/2 + \overline{u_{tt}^{(n)}\varphi^{(n)}}/\beta)_x \gg, \tag{1.4a}$$

where β is the meridional gradient of the Coriolis parameter. The scalar quantity $\varphi^{(n)}$ is given by solving an inversion equation associated with Ertel's potential vorticity (PV) to read,

$$\nabla^2\varphi^{(n)} - (f/c^{(n)})^2\varphi^{(n)} - (3/{c^{(n)}}^2)\varphi_{tt}^{(n)} = q^{(n)}, \tag{1.4b}$$

$$q^{(n)} \equiv v_x^{(n)} - u_y^{(n)} - (f/{c^{(n)}}^2)p^{(n)}, \tag{1.4c}$$

where $\nabla^2 = \partial_{xx} + \partial_{yy}$.

Inversion equation (1.4b) contains a second-order time derivative term associated with $\varphi_{tt}^{(n)}$, which makes it difficult to get the solution of $\varphi^{(n)}$. AGC17 have presented an approximated version of the energy flux to read,

$$\ll \overline{u^{(n)}p^{(n)}} + (\overline{p^{(n)}\varphi^{app}}/2)_y, \overline{v^{(n)}p^{(n)}} - (\overline{p^{(n)}\varphi^{app}}/2)_x \gg, \tag{1.5a}$$

$$\nabla^2\varphi^{app} - (f/c^{(n)})^2\varphi^{app} = q^{(n)}, \tag{1.5b}$$

which has been referred to as level-2 expression. AGC17 have suggested that the quantity φ^{app} reduces to geostrophic streamfunction in off-equatorial regions. This new scheme is a powerful tool for understanding the life-cycle (generation, propagation, dissipation process) of disturbance energy in the atmosphere and ocean without limitation of latitudes.

We consider the Helmholtz decomposition of the AGC17 level-2 flux to read,

$$-R_y - D_x = \rho_0\overline{u^{(n)}p^{(n)}} + \rho_0(\overline{p^{(n)}\varphi^{app}}/2)_y, \tag{1.6a}$$

$$+R_x - D_y = \rho_0\overline{v^{(n)}p^{(n)}} - \rho_0(\overline{p^{(n)}\varphi^{app}}/2)_x, \tag{1.6b}$$

where the scalar quantities R and D are associated with the rotational and divergent components of the energy flux, respectively, and have a unit of W/m. Taking the curl of (1.6a)–(1.6b) yields

$$\nabla^2 R = \rho_0\left(\overline{v^{(n)}p^{(n)}}\right)_x - \rho_0\left(\overline{u^{(n)}p^{(n)}}\right)_y - \rho_0\nabla^2(\overline{p^{(n)}\varphi^{app}}/2), \tag{1.6c}$$

which has been numerically solved to obtain the distribution of R. Taking the convergence of (1.6a)–(1.6b) yields

$$\nabla^2 D = -\rho_0\left(\overline{u^{(n)}p^{(n)}}\right)_x - \rho_0\left(\overline{v^{(n)}p^{(n)}}\right)_y, \tag{1.6d}$$

which has been numerically solved to obtain the distribution of D. The scalar quantities R and D may be referred to as energy-flux streamfunction and energy-flux potential, respectively.

1.3 Extension of the formulation of diagnostic scheme

AGC17 employed a single-layer system based on the shallow-water equations to derive depth-independent expressions for the energy flux. As it has the advantage of a smooth tropical-subtropical transition, the AGC17 scheme can effectively determine the horizontal distribution of the energy flux pointing in the group-velocity direction of the waves. The AGC17 scheme allowed Ogata and Aiki (2019), Li and Aiki (2020, 2022), Li *et al.* (2021), Song and Aiki (2020), and Toyoda *et al.* (2021) to obtain wholly new perspectives on the horizontal transfer routes of waves in the tropical oceans. Aiki *et al.* (2021) have extended the formulation of AGC17 to cover the case of a baroclinic system in the atmosphere. Their essential contribution is the derivation of an exact expression for the vertical component of the energy flux (this is not described in the present manuscript). The expressions given below for the horizontal component of the depth-dependent energy flux represent a straightforward extension of the content of AGC17 and are summarized in what follows by the adoption of an oceanic framework that the general reader should find convenient.

In order to investigate the vertical structure of energy transfers, we aim to derive depth-dependent expressions for the energy flux. We use the primitive equations for a Boussinesq fluid on an equatorial β-plane (Gill, 1982) appropriate for linear waves propagating in a rotating frame of reference and with zero mean flow. The subscripts, x, y, z, and t, define independent variables in a Cartesian co-ordinate system in which x, y and z increase eastward, northward, and vertically upward respectively. The parameters u, v and w represent the corresponding three-dimensional components of velocity. The governing equations (1.7a)–(1.7f) in the main text may then be written as

$$\frac{\partial u}{\partial t} - fv + \frac{\partial \Phi}{\partial x} = 0, \tag{1.7a}$$

$$\frac{\partial v}{\partial t} + fu + \frac{\partial \Phi}{\partial y} = 0, \tag{1.7b}$$

$$\frac{\partial \Phi}{\partial z} = -g\frac{\rho}{\rho_0}, \tag{1.7c}$$

$$w = \frac{-1}{N^2}\frac{\partial^2}{\partial z \partial t}, \tag{1.7d}$$

$$N^2 = -\frac{g}{\rho_0}\frac{d\bar{\rho}}{dz}, \tag{1.7e}$$

$$\frac{\partial u}{\partial x} + \frac{\partial v}{\partial y} + \frac{\partial w}{\partial z} = 0, \tag{1.7f}$$

where $f = f_0 + \beta y$ is the Coriolis parameter, $\Phi = \Phi(x, y, z, t)$ corresponds to geopotential, $\rho = \rho(x, y, z, t)$ is the perturbation of potential density. The symbols $N = N(Z)$ and g are the buoyancy frequency and the acceleration owing to gravity. The symbols ρ_0 and $\bar{\rho}(z)$ represent the reference density and the background density, respectively. Manipulation of (1.7a)–(1.7f) yields a prognostic equation for potential vorticity (symbolized as q) to read

$$\frac{\partial}{\partial t}\underbrace{\left[\frac{\partial v}{\partial x} - \frac{\partial u}{\partial y} + \frac{\partial}{\partial z}\left(\frac{f}{N^2}\frac{\partial \Phi}{\partial z}\right)\right]}_{\equiv q} + v\beta = 0. \tag{1.8}$$

This relation is generally applicable for waves at all latitudes, such as midlatitude RWs, midlatitude inertia-gravity waves (IGWs), and equatorial waves (i.e. equatorial RWs and IGWs), equatorial Rossby-gravity waves (RGWs, i.e., Yanai waves) and equatorial KWs (Matsuno, 1966; Yanai and Maruyama, 1966), on the understanding that $f_0 = 0$ for an equatorial β-plane. We let A represent an arbitrary variable (and its associated physical dimension). Equatorial KWs (i.e., $v = 0$) are characterized by $q = 0$. From (1.7a)–(1.7c), the wave energy density may be represented in prognostic fashion by

$$\frac{\partial}{\partial t}\frac{1}{2}\left[\overline{u^2 + v^2 + \frac{1}{N^2}\left(\frac{\partial \Phi}{\partial z}\right)^2}\right] +$$

$$\nabla \cdot \langle\langle \overline{u\Phi}, \overline{v\Phi}, \overline{w\Phi} \rangle\rangle = 0, \tag{1.9a}$$

where $\nabla \equiv \langle\langle \frac{\partial}{\partial x}, \frac{\partial}{\partial y}, \frac{\partial}{\partial z} \rangle\rangle$ and the overbar signifies phase-averaging (i.e., for a sinusoidal wave, $\bar{A} = 0$ for $A = u$, v, w and Φ), or low-pass time filtering. Thus we retain the local time

derivative in (1.9a), thereby permitting slow time variations in the general case. The energy flux vector in (1.9a)

$$\overline{\mathrm{U}\Phi} = \langle\langle \overline{u\Phi}, \overline{v\Phi}, \overline{w\Phi} \rangle\rangle, \tag{1.9b}$$

is codirectional with the group velocity for midlatitude IGWs in the atmosphere and ocean (Gill, 1982).

However, for midlatitude RWs, the energy flux of (1.9b) is not aligned with wave group velocity (Longuet-Higgins, 1964). In order to obtain an expression for the energy flux that is codirectional with group velocity for all wave types, we now revisit the equations defining the energy flux transmitted by equatorial waves. As before, we assume linear waves on an equatorial β-plane and zero mean flow. Following Matsuno (1966) and Gill (1982), we use a horizontal length scale $\sqrt{NH/\beta}$, a vertical length scale H, and a time scale $1/\sqrt{NH\beta}$ in order to non-dimensionalize equations (1.9a)–(1.9f) giving

$$x = \left(\sqrt{NH\beta}\right)\tilde{x}, y = \left(\sqrt{NH\beta}\right)\tilde{y}, z = H\tilde{z}, t = (1/\sqrt{NH\beta})\tilde{t},$$

$$u = (NH)\tilde{u}, v = (NH)\tilde{v}, w = (\sqrt{NH^3\beta})\tilde{w}, \Phi = (NH)^2\tilde{\Phi}, \tag{1.10}$$

and

$$\tilde{u}_t - \tilde{y}\tilde{v} + \tilde{\Phi}_x = 0, \tag{1.11a}$$

$$\tilde{v}_t + \tilde{y}\tilde{u} + \tilde{\Phi}_y = 0, \tag{1.11b}$$

$$\tilde{u} = -\tilde{\Phi}_{tz}, \tag{1.11c}$$

$$\tilde{u}_x + \tilde{v}_y + \tilde{w}_z = 0. \tag{1.11d}$$

where subscripts x, y, z, and t indicate partial differentials in terms of $\tilde{x}$, $\tilde{y}$, $\tilde{z}$, and $\tilde{t}$, respectively. Hereafter symbols with a tilde indicate non-dimensionalized quantities.

Equations (1.11a)–(1.11c) can then be manipulated to give the following prognostic equations for potential vorticity (PV: symbolized as q) and wave energy in de-dimensionalized form:

$$\frac{\partial}{\partial \tilde{t}}\underbrace{\left(\tilde{v}_x - \tilde{u}_y + \tilde{y}\widetilde{\Phi}_{zz}\right)}_{\equiv \tilde{q}} + \tilde{v} = 0, \tag{1.12}$$

$$\frac{\partial}{\partial \tilde{t}}\left(\overline{\frac{\tilde{u}^2 + \tilde{u}^2 + \widetilde{\Phi}_z^2}{2}}\right) + \nabla \cdot \langle\langle \overline{\tilde{u}\widetilde{\Phi}}, \overline{\tilde{v}\widetilde{\Phi}}, \overline{\tilde{w}\widetilde{\Phi}}\rangle\rangle = 0, \tag{1.13}$$

where $\nabla \equiv \langle\langle \frac{\partial}{\partial \tilde{x}}, \frac{\partial}{\partial \tilde{y}}, \frac{\partial}{\partial \tilde{z}}\rangle\rangle$.

In the following we take $\tilde{v} \not\equiv 0$, as is appropriate for waves other than equatorial KWs such as equatorial RWs, RGWs, and IGWs. We then assume zonally and vertically propagating free waves varying as $\tilde{v} \propto \cos\mu$, $\tilde{u} \propto \sin\mu$ and $\widetilde{\Phi} \propto \sin\mu$ where $\mu = k\tilde{x} + m\tilde{z} - \omega\tilde{t}$ is wave phase and k, m and ω are the zonal and vertical wavenumbers, and wave frequency, respectively. Substituting into equations (1.11a)–(1.11d), and with further manipulation, we obtain an equation characterizing the meridional structure of $\tilde{v}$ as,

$$\tilde{v}_{yy} + (w^2m^2 - k^2 - k/\omega - m^2y^2)\tilde{v} = 0. \tag{1.14}$$

Let the Hermite polynomial for *j*-th meridional mode be defined as

$$\frac{dH^{(j,m)}}{d\tilde{y}} = 2m^{\frac{1}{2}}jH^{(j-1,m)}, \tag{1.15a}$$

$$H^{(j+1,m)} = 2m^{\frac{1}{2}}\tilde{y}H^{(j,m)} - 2jH^{(j-1,m)}, \tag{1.15b}$$

which yields

$$H^{(0,m)} = 1, \tag{1.15c}$$

$$H^{(1,m)} = 2m^{\frac{1}{2}}\tilde{y}, \tag{1.15c}$$

$$H^{(2,m)} = 4m\tilde{y}^3 - 2, \tag{1.15d}$$

$$H^{(3,m)} = 8m^{\frac{3}{2}}\tilde{y}^3 - 12m^{\frac{1}{2}}\tilde{y}, \tag{1.15e}$$

$$H^{(4,m)} = 16m^2\tilde{y}^4 - 48m\tilde{y}^2 + 1, \tag{1.15f}$$

and

$$\frac{dG^2}{d\tilde{y}^2} + m(2j+1)G - m^2\tilde{y}^2G = 0, \tag{1.15g}$$

for $G = \exp(-m\tilde{y}^2)H^{(n,m)}$. A solution for the system of equations (1.11a)–(1.11d) and (1.14) was obtained by Matsuno (1966) as

$$\tilde{v} = \mathcal{A}\cos\mu \exp\left(-\frac{m\tilde{y}^2}{2}\right)H^{(j,m)}, \tag{1.16a}$$

$$\tilde{u} = \frac{\omega m^2 \tilde{y}\tilde{v}_\mu - k\tilde{v}_{y\mu}}{(\omega^2 m^2 - k^2)}, \tag{1.16b}$$

$$\widetilde{\Phi} = \frac{k\tilde{y}\tilde{v}_\mu - \omega\tilde{v}_{y\mu}}{\omega^2 m^2 - k^2}, \tag{1.16c}$$

$$\widetilde{w} = -\widetilde{\Phi}_{tz} = \omega\widetilde{\Phi}_{\mu z} = -\omega m\widetilde{\Phi}, \tag{1.16d}$$

where $\mathcal{A}$ is wave amplitude. The subscript μ signifies the partial derivative with respect to wave phase [i.e., $\tilde{v}_\mu \equiv \partial\tilde{v}/\partial\mu = -\mathcal{A}\sin\mu\exp(-m\tilde{y}^2/2)H^{(j,m)}$].

Substitution of (1.16a) into (1.14) yields,

$$\omega^3 m^3 - (k^2 + 2mj + m)\omega - k = 0. \tag{1.17}$$

This latter dispersion relation provides a unified description for equatorial RWs, RGWs, and IGWs. A unified expression for the group velocity of equatorial waves can then be obtained through partial differentiation of (1.17) with respect to wavenumber k yielding

$$\frac{\partial\omega}{\partial k} = \frac{2k\omega + 1}{3\omega^2 m^2 - (k^2 + 2mj + m)} = \frac{2\omega^2 + \omega/k}{2\omega^3 m^2/k + 1}, \tag{1.18}$$

where the term $2\omega^3 m^2/k$ in the denominator has generally been ignored in earlier studies which focus on low-frequency equatorial waves (e.g. equatorial RWs; Gill, 1982).

In order to identify the additional rotational flux associated with the horizontal energy flux, we investigate the zonal component of the energy flux associated with (1.11a)–(1.11d). For equatorial waves, the meridional integral of $\overline{\tilde{u}\widetilde{\Phi}}$ equals the product of the group velocity and the meridional integral of the wave energy density (Philander, 1989):

$$\int_{-\infty}^{+\infty}\overline{\tilde{u}\widetilde{\Phi}}\,d\tilde{y} = \int_{-\infty}^{+\infty}(\partial\omega/\partial k)(\overline{\tilde{u}^2 + \tilde{v}^2 + \widetilde{\Phi}_z^2})/2\;d\tilde{y}. \tag{1.19a}$$

Note that identity (1.19a) only holds after the meridional integration i.e.

$$\overline{\tilde{u}\tilde{\Phi}} \neq (\partial\omega/\partial k)(\overline{\tilde{u}^2 + \tilde{v}^2 + \tilde{\Phi}_z^2})/2. \tag{1.19b}$$

However, for our purposes, the derivation of an analytical expression for the difference between the two sides of (1.19b) provides a useful basis for discussion. As a first step towards specifying this difference, the geopotential flux $\overline{\tilde{u}\tilde{\Phi}}$ can be divided into two parts, the first of which determines the meridional integral itself while the second part makes zero contribution to it:

$$\begin{aligned}
&\overline{\tilde{u}\tilde{\Phi}} \\
&= \frac{\tilde{y}^2\overline{\tilde{v}\tilde{v}}(\omega k m^2) - \tilde{y}\overline{\tilde{v}_y\tilde{v}}(\omega^2 m^2 + k^2) + \overline{\tilde{v}_y\tilde{v}_y}(\omega k)}{(\omega^2 m^2 - k^2)^2} \\
&= \frac{\overline{\tilde{v}\tilde{v}}(2\omega k + 1)}{2(\omega^2 m^2 - k^2)} - \frac{\left(\omega\overline{\tilde{u}\tilde{v}_\mu} + k\overline{\tilde{\Phi}\tilde{v}_\mu}\right)_y}{2(\omega^2 m^2 - k^2)}.
\end{aligned} \tag{1.19c}$$

Thus the meridional integral of the second of these two terms is zero (as $\tilde{v}$ and $\tilde{y}\tilde{v}$ tend to zero with increasing distance from the equator).

The wave energy density can be similarly decomposed into two parts on the basis of whether there is a meridional-integral contribution or not [the factor $\partial\omega/\partial k$ required to calculate the energy density flux is inserted in (1.19e)]. We then have

$$\begin{aligned}
&(\overline{\tilde{u}^2 + \tilde{v}^2 + \tilde{\Phi}_z^2})/2 \\
&= \frac{\overline{\tilde{v}\tilde{v}}(2\omega^2 m^2 + k/\omega)}{2(\omega^2 m^2 - k^2)} - \frac{\left(\omega m^2\overline{\tilde{\Phi}\tilde{v}_\mu} + k\overline{\tilde{u}\tilde{v}_\mu}\right)_y}{2(\omega^2 m^2 - k^2)}.
\end{aligned} \tag{1.19d}$$

As before, the second of these two terms makes zero contribution to the meridional integral. Using (1.19c)–(1.19d), the required analytical expression for the difference between the right and left hand sides of (1.19b) can be derived as,

$$\begin{aligned}
&\frac{\partial\omega}{\partial k}\left(\frac{\overline{\tilde{u}^2 + \tilde{v}^2 + \tilde{\Phi}_z^2}}{2}\right) - \overline{\tilde{u}\tilde{\Phi}} \\
&= \frac{-(\overline{\tilde{\Phi}\tilde{v}_\mu})_y - (\overline{2\tilde{u}_{tt}\tilde{v}_\mu})_y}{2k(1 + 2\omega^3 m^2/k)},
\end{aligned} \tag{1.19e}$$

where the right-hand side has been written as the meridional gradient of scalar quantities. In the case of equatorial waves with decaying meridional structures, the meridional integral of (1.19e) vanishes, consistent with (1.19a).

On the basis of (1.19e), the product of the zonal component of group velocity and the wave energy density can be rewritten as,

$$\frac{\partial \omega}{\partial k}\left(\overline{\frac{\tilde{u}^2+\tilde{v}^2+\tilde{\Phi}_z^2}{2}}\right)=\overline{\tilde{u}\tilde{\Phi}}+\left(\overline{\frac{\tilde{\Phi}\tilde{\varphi}}{2}}+\overline{\tilde{u}_{tt}\tilde{\varphi}}\right)_y, \tag{1.20a}$$

$$\tilde{\varphi}\equiv-\frac{\tilde{v}_\mu}{k+2\omega^3m^2}, \tag{1.20b}$$

where we have introduced the scalar quantity φ, as in AGC17. We note that, for any type of equatorial wave, there is a precise identity between the meridional profile of the zonal energy flux on the right hand side of (1.20a) and the quantity $(\partial\omega/\partial k)(\overline{\tilde{u}^2+\tilde{v}^2+\tilde{\Phi}_z^2})/2$. The depth-independent framework of AGC17 has here been extended to a depth-dependent framework.

The definition of φ in (1.20b) makes use of a Fourier expansion. AGC17 have shown in a depth-independent form that (1.20b) can be reformulated such that the parameters μ, k, m and ω are absent, thereby yielding an inversion equation for PV. The latter inversion equation is here extended to a depth-dependent form to read,

$$\begin{aligned}\tilde{q}&=-\tilde{v}_\mu/\omega\\&=(k/\omega+2\omega^3m^2)\tilde{\varphi}\\&=\tilde{\varphi}_{yy}+(3\omega^2m^2-k^2-m^2y^2)\tilde{\varphi}\\&=(\partial_{xx}+\partial_{yy})\tilde{\varphi}-m^2\tilde{y}^2\tilde{\varphi}-3m^2\tilde{\varphi}_{tt}\\&=(\partial_{xx}+\partial_{yy})\tilde{\varphi}+(\tilde{y}^2\tilde{\varphi}+3\tilde{\varphi}_{tt})_{zz},\end{aligned} \tag{1.21a}$$

where the first and second lines have been derived using equations (1.12) and (1.20b), respectively [i.e., $\tilde{q}_t=-\omega\tilde{q}_\mu=-\tilde{v}$ and thus $-\omega\tilde{q}_{\mu\mu}=\omega\tilde{q}=-\tilde{v}_\mu$]. The depth-dependent

inversion equation (1.21a) for PV forms the foundation of this present work since it suggests the possibility that the scalar quantity φ can be estimated via an iterative numerical method. The inversion equation (1.21a) can be presented in dimensional form as,

$$\left(\frac{\partial^2}{\partial x^2}+\frac{\partial^2}{\partial y^2}\right)\varphi+\frac{\partial}{\partial z}\left[\left(\frac{1}{N^2}\right)\frac{\partial}{\partial z}\left(f^2\varphi+3\frac{\partial^2}{\partial t^2}\varphi\right)\right]=q, \tag{1.21b}$$

where q has been defined at (1.5b). The depth-dependent inversion equations (1.21a)–(1.21b) of PV correspond to the depth-independent inversion equations (1.12) and (1.13), respectively, of AGC17 and are referred to as level-0 (i.e. exact) expression.

AGC17 considered eliminating the term representing the second order time derivative in their exact inversion equation for PV [this corresponds to (1.21b) in the present study]. Let φ^{app} be the solution of the approximated PV inversion equation to read,

$$\left(\frac{\partial^2}{\partial x^2}+\frac{\partial^2}{\partial y^2}\right)\varphi^{app}+\frac{\partial}{\partial z}\left(\frac{f^2}{N^2}\frac{\partial}{\partial z}\varphi^{app}\right)=q, \tag{1.22a}$$

which may be solved using the set of a Dirichlet boundary condition ($\varphi^{app}=0$) at coastlines and bottom topography and a Neumann boundary condition ($\partial\varphi^{app}/\partial z=0$) at the sea surface. What AGC17 have called level-2 (i.e. approximate) expression for the energy flux may be extended here to a depth-dependent form as,

$$\overline{\mathrm{U}\Phi}+\langle\langle\frac{\partial}{\partial y}\left(\frac{\overline{\varphi^{app}\Phi}}{2}\right),-\frac{\partial}{\partial x}\left(\frac{\overline{\varphi^{app}\Phi}}{2}\right),0\rangle\rangle, \tag{1.22b}$$

which has been used in the overall model analyses of the present study.

The energy flux of equatorial KWs has not so far been investigated. As the latter are gravity waves, $\overline{\mathrm{U}\Phi}$ becomes identical to the product of group velocity and wave energy. In particular, no term for additional rotational flux is present. Since a characteristic of KWs is that the term $q=0$, the expression for the KW energy flux given in (1.22b) reduces to $\overline{\mathrm{U}\Phi}$. This result is consistent with the nature of gravity waves.

1.4 Research objectives and thesis structure

The main objective of this study is to clarify the mechanism of tropical climate variations in the IO based on the transfer routes of wave energy. The development of wave energy is poorly understood owing to the lack of an appropriate diagnostic scheme for tracing group velocity vectors. The pressure flux scheme is suitable for IGWs but is not applicable for mid-latitude RWs. This shortcoming is filled up by OS93 scheme, which is successful to trace the transfer episodes of westward energy flux. A recently proposed seamless diagnostic scheme described in AGC17 has the advantage for tracing the all waves without the limitation of latitudes (Ogata and Aiki, 2019; Li and Aiki, 2020; Song and Aiki, 2020; Li *et al.*, 2021; Song and Aiki, 2021; Toyoda *et al.*, 2021; Li and Aiki, 2022). The AGC17 allow us to have a better understanding of the development process (generation, propagation, reflection and diffraction) of wave energy.

This dissertation consists of 5 chapters which are organized as follows. Chapter 1 gives a general introduction of the seasonal and interannual variations in the tropical IO and describes the diagnostic scheme for tracing transfer routes of wave energy in horizontal and vertical planes, respectively. In chapter 2, we compared the performance of three diagnostic schemes described in section 1.2 and examine the life-cycle of wave energy in the tropical IO in response to the climatological monsoon winds. Chapter 3 is an extension of chapter 2, which focuses on the vertical distribution of wave energy in the tropical IO and analyses the development process in vertical plane using AGC17 scheme. Chapter 4 looks insight into the interannual timescales in the tropical IO. The evolution of wave energy during a pure positive IOD in 1994 has been examined by tracing the transfer episodes of wave energy in chapter 4. Chapter 5 presents a general discussion based on the finding of above chapters. Chapter 6 summarizes the results of this dissertation and give some suggestions for future researches about wave energy.

Table 1.1 List of symbols used in the present study, where A is arbitrary quantities written dimensionally. The coordinate axes x, y, z increase eastward, northward, and vertically upward, respectively.

$f = f_0 + \beta y$	Coriolis parameter
$N = \sqrt{-(g/\rho_0)(d\bar{\rho}/dz)}$	buoyancy frequency
H	vertical scale of the ocean (constant)
x, y, z, t	Cartesian coordinates
$\langle\langle a, b, c\rangle\rangle$	vector with x, y and z-axis components a, b and c
$\mathrm{U} \equiv \langle\langle u, v, w\rangle\rangle$	velocity vector
$\nabla \equiv \langle\langle \partial_x, \partial_y, \partial_z\rangle\rangle$	gradient operator
Φ	geopotential
q	potential vorticity $q \equiv v_x - u_y + [(f/N^2)\Phi_z]_z$
φ	solution of (1.21b)
φ^{app}	solution of (1.22a)
μ	wave phase
k	zonal wavenumber
m	vertical wavenumber
ω	wave frequency
$H^{(j,m)}$	Hermite polynomial
j	meridional mode number of free equatorial waves
$\bar{A}$	phase-average of A

Chapter 2

The life-cycle of annual waves in the Indian Ocean as identified by seamless diagnosis of the energy flux

2.1 Introduction

Significant annual and semi-annual variations in currents and large-scale waves take place in the IO. At the equator, westerly winds in spring and autumn cause the semi-annual appearance of a Wyrtki (1973) jet as well as equatorial KWs, which propagate eastward (Schott and McCreary, 2001, hereafter SM01). The strong westerly winds have a decisive effect on the development and termination of IO Dipole events (Saji *et al.,* 1999; Rao and Yamagata, 2004). Further south, trade winds are persistent in regions around 10°S, while transient signals of heat content associated with westward propagating RWs are often found in the southern IO (at latitudes of 8–15°S), which may be partly attributed to wind-forcing in the Pacific Ocean during ENSO events (Huang and Kinter, 2002; Ummenhofer *et al.,* 2017).

In the IO, annual and semi-annual oscillations and also climate variations are closely linked to the propagation of KWs and RWs (Mark and Huang, 2004; Rahul *et al.,* 2004; Rao *et al.,* 2010). As a packet of oceanic equatorial KWs strikes the eastern boundary, it is refracted backwards and is also deflected polewards and becomes the source of both equatorial and mid-latitude RWs which then propagate westward along the flanks of the equator (Schopf *et al.*, 1981; McPhaden and Ripa, 1990; Yu *et al.,* 1991; Ogata *et al.*, 2017). Wave reflection and diffraction at the zonal boundaries of the IO induce interactions between tropical and subtropical regions. It is therefore important to investigate how these waves are linked to each other and where they originate from, without subdividing the description in order to reflect the differences in dynamics between the tropical and subtropical regions (Fukutomi *et al.,* 2002). This issue is explained in the next paragraph.

The aim of the present study is to clarify the mechanical links between the various wave constituents of the IO. At least three existing schemes based on group-velocity analysis are in use for diagnosing the geographical routes along which wave energy is transferred (note that these schemes do not rely on Fourier analysis or on ray theory, explained later in the manuscript). The pressure-flux scheme can be used for inertia-gravity waves (Cummins and Oey, 1997), the quasi-geostrophic scheme can be used for mid-latitude RWs (Orlanski and Sheldon, 1993, hereafter OS93) though not for equatorial waves or for coastal regions, while Aiki *et al.* (2017, hereafter abbreviated as AGC17) have developed a diagnostic scheme that tracks the movement of wave energy at all latitudes while satisfying coastal boundary conditions. The latter represents a powerful new tool for understanding the life-cycle (generation, propagation, dissipation process) of disturbance energy in the atmosphere and ocean and is applicable generally rather than to a specific range of latitudes (Ogata and Aiki, 2019).

This study represents the first application of the seamless AGC17 scheme and forms part of a comprehensive investigation of the transfer routes of wave energy in the IO. This initial paper will focus primarily on the seasonal variations. Results from an investigation of interannual variations will be presented in a future study. This manuscript is organized as follows. In section 2.2, we carry out a set of numerical experiments using a shallow-water equation model associated with the fundamental baroclinic modes that are forced by climatological monsoon winds in the IO. We analyze the transfer routes of wave energy in the IO in section 2.3 and summarize our results in section 2.4.

2.2 Materials and Method

2.2.1 Preliminary analysis

Using the vertical profiles of annual mean salinity and temperature given in the World Ocean Atlas, we have estimated the gravity wave speed $c^{(n)}$ for the *n*-th baroclinic mode in the tropical IO (20°S–20°N, 40°E–110°E) based on the bottom-pressure decoupling theory of Tailleux and McWilliams (2001). This eigenvalue problem yields 2.99, 1.69, and 1.03 m/s for the first, second, and third baroclinic modes, respectively (see Table 2.1 for the corresponding values of equatorial deformation radius and equatorial inertial period). To travel back and forth through a zonal distance L of the IO at the equator (from 45°E to 100°E) takes 0.26, 0.46 and 0.75 years (hereafter referred to as basin-mode periods) for the first, second, and third baroclinic mode, respectively. These periods have been estimated as $L/c^{(n)} + 3L/c^{(n)}$, on the understanding that the phase speeds of equatorial KWs and long equatorial RWs are written as $c^{(n)}$(eastward) and $c^{(n)}/3$ (westward), respectively. It is well known that, given the basin-mode period of about half a year, the second baroclinic mode is best suited to show the response of the tropical IO to semi-annual wind-forcing.

2.2.2 Model setup

We have performed a set of 20-year climatological experiments associated with the three fundamental baroclinic modes. The model has been discretized in a spherical coordinate system with a grid spacing of 1/4 degree in both zonal and meridional directions. The model domain extends from 35°E–120°E and from 25°S–20°N, and adopts realistic coastlines except for the lack of connection to the Southern Ocean and the Pacific Ocean. For simplicity, all equations in the present manuscript are written in Cartesian coordinates with positive *x* and *y* representing the eastward and northward directions. We have used a shallow-water equation model that has been written for the development of zonal velocity $u^{(n)}$, meridional velocity $v^{(n)}$, and geopotential $p^{(n)}$ for the *n*-th baroclinic mode as

$$u_t^{(n)} - fv^{(n)} + p_x^{(n)} = \alpha^{(n)} \frac{\tau_{wind}^x}{\rho_0 \sqrt{H_{mix} H_{bottom}}} + SGS^x, \quad (2.1a)$$

$$v_t^{(n)} + fu^{(n)} + p_y^{(n)} = \alpha^{(n)} \frac{\tau_{wind}^y}{\rho_0 \sqrt{H_{mix} H_{bottom}}} + SGS^y, \quad (2.1b)$$

$$p_t^{(n)} + (c^{(n)})^2 (u_x^{(n)} + v_y^{(n)}) = 0, \quad (2.1c)$$

where subscripts *x*, *y* and *t* represent partial derivatives associated with the horizontal coordinates and time. Wind stress vector has been calculated by two steps as follows. First we have applied the bulk formula of Large and Pond (1981) to 10-m wind velocity in the European Centre for Medium-Range Weather Forecasts Re-analysis (ECMWF ERA-40) data on 2.5×2.5 degree grids. Here we have used the absolute wind velocity rather than the relative wind velocity (i.e. the difference of the wind velocity and oceanic surface velocity) to calculate the wind stress vector for simplicity. Then we have computed the monthly climatology of wind stress vector and subtracted a climatological annual mean component over the long-term from 1957 to 2002. Thus, the wind stress ($\tau_{wind}^x, \tau_{wind}^y$) in the present study represents the seasonal anomaly component of monthly climatology between 1957 and 2002. Use of the seasonal anomaly while excluding the annual mean enables us to focus on the climatological annual and semi-annual variations of waves related to the monsoon in the IO. Further important influences from both wave-mean flow interactions and interannual variability will be addressed in a later study.

Wind-induced momentum input to the mixed-layer is partitioned into each baroclinic mode and has been estimated here by a non-dimensional parameter $\alpha^{(n)}$ = 0.35, 0.44, and 0.27 in (2.1a)-(2.1b) for the first, second and third baroclinic modes, respectively. $\rho_0 =$ 1027 kg/m^3 in (2.1a)-(2.1b) is the reference density of seawater, H_{mix}= 35.0 m is the annual mean value of the mixed-layer depth based on a temperature difference of 0.2℃ (as estimated from Argo data gathered in the tropical IO), and H_{bottom}= 5500 m is the reference value of water depth in the tropical IO. The subgrid-scale (SGS) terms in (2.1a)-(2.1b) represent the

effect of lateral eddy viscosity based on the Smagorinsky *et al.* (1965) scheme and use a non-dimensional coefficient of 0.1 after squaring. We have performed a total of three experiments for the three fundamental baroclinic modes, each of which has been integrated for 20 years, including spin-up from the state of no motion. We have confirmed that a climatologically equilibrium state has been reached (not shown) in the course of the model integration of each experiment, for which all 100 snapshots (with an output interval of 3.65 days) during the last year are used in the following overall analysis.

The nondimensional parameter $\alpha^{(n)}$ in (2.1a)-(2.1b) in the main manuscript represents the ratio of wind-induced momentum input to the *n*-th baroclinic mode. For simplicity, here we assume a horizontally uniform ocean and let $u = u(z,t)$ and $v = v(z,t)$ be the zonal and meridional components of velocity, respectively. The tendency term and the turbulent mixing term in the horizontal component of momentum equations may be written as,

$$\rho_0 \partial_t u + \cdots = \cdots + \partial_z(\tau^x_{turb}), \tag{2.2a}$$

$$\rho_0 \partial_t v + \cdots = \cdots + \partial_z(\tau^y_{turb}), \tag{2.2b}$$

where ρ_0 is the reference density of seawater. The symbols $\tau^x_{turb} = \tau^x_{turb}(z,t)$ and $\tau^y_{turb} = \tau^y_{turb}(z,t)$ represent vertical stress for the horizontal components of momentum associated with wind-induced turbulence in the surface mixed-layer. The present study assumes that the turbulent stress has a linear vertical profile at depths in the surface mixed-layer and vanishes underneath (Fig. 2.1),

$$\tau^x_{turb} = \tau^x_{wind} S, \tag{2.3a}$$

$$\tau^y_{turb} = \tau^y_{wind} S, \tag{2.3b}$$

$$S = S(z) = \begin{cases} z/H_{mix} + 1 & \text{for } -H_{mix} \le z \le 0, \\ 0 & \text{for } -H_{bottom} \le z < -H_{mix}, \end{cases} \tag{2.3c}$$

where the sea surface is located at $z = 0$. The symbols $\tau^x_{wind} = \tau^x_{wind}(t)$ in (2.3a) and $\tau^y_{wind} = \tau^y_{wind}(t)$ in (2.3b) represent the zonal and meridional components of wind stress

applied at the sea surface, respectively. The vertical divergence of the turbulent stress acts as a body force in the momentum equations (2.2a)–(2.2b), which has a stepped vertical profile in the present study (Fig. 2.1b). Namely, both the zonal and meridional components of the wind-induced force are vertically constant (τ^x_{wind}/H_{mix} and τ^y_{wind}/H_{mix}, respectively) at depths in the surface mixed-layer and vanish underneath. To be useful later in this section, we take the depth integral of the zonal and meridional components of the wind-induced force (i.e., the vertical divergence of the turbulent stress) to yield

$$\int_{-H_{bottom}}^{0} \partial_z(\tau^x_{turb})\, dz = (\tau^x_{wind}/H_{mix})H_{mix} = \tau^x_{wind}, \tag{2.4a}$$

$$\int_{-H_{bottom}}^{0} \partial_z(\tau^y_{turb})\, dz = (\tau^y_{wind}/H_{mix})\, H_{mix} = \tau^y_{wind}. \tag{2.4b}$$

Likewise, we take the depth integral of the square of each of the zonal and meridional components of the wind-induced force to yield

$$\int_{-H_{bottom}}^{0} (\partial_z(\tau^x_{turb}))^2\, dz = (\tau^x_{wind}/H_{mix})^2 H_{mix} = (\tau^x_{wind})^2/H_{mix}, \tag{2.5a}$$

$$\int_{-H_{bottom}}^{0} (\partial_z(\tau^y_{turb}))^2\, dz = (\tau^y_{wind}/H_{mix})^2 H_{mix} = (\tau^y_{wind})^2/H_{mix}. \tag{2.5b}$$

We shall decompose the wind-induced force, mentioned above, to baroclinic normal modes. Let $F^{(n)} = F^{(n)}(z)$ and n be the eigenfunction and its order of the Sturm-Liouville problem associated with the vertical profile of buoyancy frequency $N = N(z)$ in the ocean to read,

$$\partial_z((\partial_z F^{(n)})/N^2) = -F^{(n)}/(c^{(n)})^2, \tag{2.6a}$$

$$\int_{-H_{bottom}}^{0} (F^{(n)})^2\, dz = H_{bottom}, \tag{2.6b}$$

$$\partial_z F^{(n)} = 0 \text{ and } F^{(n)} > 0 \text{ at } z = 0, \tag{2.6c}$$

$$F^{(n)} = 0 \text{ at } z = -H_{bottom}, \tag{2.6d}$$

where $c^{(n)}$ is the speed of nonrotating gravity waves for the *n*-th baroclinic mode. The wind-induced force (i.e., the vertical divergence of the turbulent stress) may be decomposed using a set of nondimensional coefficients $\alpha^{(n)}$ associated with the *n*-th baroclinic mode to read,

$$\partial_z(\tau^x_{turb}) = A^x \sum_n \alpha^{(n)} F^{(n)}, \tag{2.7a}$$

$$\partial_z(\tau^y_{turb}) = A^y \sum_n \alpha^{(n)} F^{(n)}, \tag{2.7b}$$

$$\sum_n {\alpha^{(n)}}^2 = 1, \tag{2.7c}$$

where the symbols $A^x = A^x(t)$ and $A^y = A^y(t)$ represent mode-independent amplitudes associated with the zonal and meridional directions. Using (2.6a)–(2.6d) and (2.7a)–(2.7c), we revisit the depth integral of the square of each of the zonal and meridional components of the wind-induced force to yield,

$$\int_{-H_{bottom}}^{0} (\partial_z(\tau^x_{turb}))^2 \, dz = (A^x)^2 H_{bottom} \left(\sum_n {\alpha^{(n)}}^2 \right) = (A^x)^2 H_{bottom}, \tag{2.8a}$$

$$\int_{-H_{bottom}}^{0} (\partial_z(\tau^y_{turb}))^2 \, dz = (A^y)^2 H_{bottom} \left(\sum_n {\alpha^{(n)}}^2 \right) = (A^y)^2 H_{bottom}. \tag{2.8b}$$

The set of (2.5a)–(2.5b) and (2.8a)–(2.8b) determines an analytical expression for the mode-independent amplitudes as follows,

$$A^x = \tau^x_{wind} / \sqrt{H_{mix} H_{bottom}}, \tag{2.9a}$$

$$A^y = \tau^y_{wind} / \sqrt{H_{mix} H_{bottom}}. \tag{2.9b}$$

We now project the vertical profile of the wind-induced force based on (2.7a)–(2.7b) to the eigenfunction of each baroclinic mode to read,

$$\int_{-H_{bottom}}^{0} (\partial_z(\tau^x_{turb})) F^{(n)} \, dz = A^x H_{bottom} \alpha^{(n)} = \tau^x_{wind} \sqrt{H_{bottom}/H_{mix}} \, \alpha^{(n)}, \tag{2.10a}$$

$$\int_{-H_{bottom}}^{0} (\partial_z(\tau^y_{turb})) F^{(n)} \, dz = A^y H_{bottom} \alpha^{(n)} = \tau^x_{wind} \sqrt{H_{bottom}/H_{mix}} \, \alpha^{(n)}, \tag{2.10b}$$

where (2.6b) and (2.9a)–(2.9b) have been used. Substitution of (2.3a)–(2.3c) to (2.10a)–(2.10b) yields an analytical expression for the nondimensional coefficient $\alpha^{(n)}$ to read,

$$\alpha^{(n)} = \int_{-H_{mix}}^{0} F^{(n)} \, dz / \sqrt{H_{bottom} H_{mix}}, \tag{2.11}$$

which has been estimated in the present study using the set of eigenfunctions associated with the climatological annual-mean stratification of the tropical IO (see Fig. 2.3c) to yield 0.35, 0.44, and 0.27 for the first, second, third baroclinic modes, respectively, as listed in Table 2.1.

2.2.3 Definition of nondimensional parameter $\alpha^{(n)}$

The nondimensional parameter $\alpha^{(n)}$ in (2.1a)-(2.1b) in the main manuscript represents the ratio of wind-induced momentum input to the *n*-th baroclinic mode. For simplicity, here we assume a horizontally uniform ocean and let $u = u(z,t)$ and $v = v(z,t)$ be the zonal and meridional components of velocity, respectively. The tendency term and the turbulent mixing term in the horizontal component of momentum equations may be written as,

$$\rho_0 \partial_t u + \cdots = \cdots + \partial_z(\tau^x_{turb}), \tag{2.12a}$$

$$\rho_0 \partial_t v + \cdots = \cdots + \partial_z(\tau^y_{turb}), \tag{2.12b}$$

where ρ_0 is the reference density of seawater. The symbols $\tau^x_{turb} = \tau^x_{turb}(z,t)$ and $\tau^y_{turb} = \tau^y_{turb}(z,t)$ represent vertical stress for the horizontal components of momentum associated with wind-induced turbulence in the surface mixed-layer. The present study assumes that the turbulent stress has a linear vertical profile at depths in the surface mixed-layer and vanishes underneath (Fig. A1a in Supporting Information),

$$\tau^x_{turb} = \tau^x_{wind} S, \tag{2.13a}$$

$$\tau^y_{turb} = \tau^y_{wind} S, \tag{2.13b}$$

$$S = S(z) = \begin{cases} z/H_{mix} + 1 & \text{for } -H_{mix} \le z \le 0, \\ 0 & \text{for } -H_{bottom} \le z < -H_{mix}, \end{cases} \tag{2.13c}$$

where the sea surface is located at $z = 0$. The symbols $\tau^x_{wind} = \tau^x_{wind}(t)$ in (2.13a) and $\tau^y_{wind} = \tau^y_{wind}(t)$ in (2.13b) represent the zonal and meridional components of wind stress applied at the sea surface, respectively. The vertical divergence of the turbulent stress acts as a body force in the momentum equations (2.2a)-(2.2b), which has a stepped vertical profile in

the present study (Fig. 2.1b). Namely, both the zonal and meridional components of the wind-induced force are vertically constant (τ^x_{wind}/H_{mix} and τ^y_{wind}/H_{mix}, respectively) at depths in the surface mixed-layer and vanish underneath. To be useful later in this section, we take the depth integral of the zonal and meridional components of the wind-induced force (i.e., the vertical divergence of the turbulent stress) to yield

$$\int_{-H_{bottom}}^{0} \partial_z(\tau^x_{turb})\, dz = (\tau^x_{wind}/H_{mix})H_{mix} = \tau^x_{wind}, \tag{2.14a}$$

$$\int_{-H_{bottom}}^{0} \partial_z(\tau^y_{turb})\, dz = (\tau^y_{wind}/H_{mix})\, H_{mix} = \tau^y_{wind}. \tag{2.14b}$$

Likewise, we take the depth integral of the square of each of the zonal and meridional components of the wind-induced force to yield

$$\int_{-H_{bottom}}^{0} (\partial_z(\tau^x_{turb}))^2\, dz = (\tau^x_{wind}/H_{mix})^2 H_{mix} = (\tau^x_{wind})^2/H_{mix}, \tag{2.15a}$$

$$\int_{-H_{bottom}}^{0} (\partial_z(\tau^y_{turb}))^2\, dz = (\tau^y_{wind}/H_{mix})^2 H_{mix} = (\tau^y_{wind})^2/H_{mix}. \tag{2.15b}$$

We shall decompose the wind-induced force, mentioned above, to baroclinic normal modes. Let $F^{(n)} = F^{(n)}(z)$ and n be the eigenfunction and its order of the Sturm-Liouville problem associated with the vertical profile of buoyancy frequency $N = N(z)$ in the ocean to read,

$$\partial_z((\partial_z F^{(n)})/N^2) = -F^{(n)}/(c^{(n)})^2, \tag{2.16a}$$

$$\int_{-H_{bottom}}^{0} (F^{(n)})^2\, dz = H_{bottom}, \tag{2.16b}$$

$$\partial_z F^{(n)} = 0 \text{ and } F^{(n)} > 0 \text{ at } z = 0, \tag{2.16c}$$

$$F^{(n)} = 0 \text{ at } z = -H_{bottom}, \tag{2.16d}$$

where $c^{(n)}$ is the speed of nonrotating gravity waves for the *n*-th baroclinic mode. The wind-induced force (i.e., the vertical divergence of the turbulent stress) may be decomposed using a set of nondimensional coefficients $\alpha^{(n)}$ associated with the *n*-th baroclinic mode to read,

$$\partial_z(\tau^x_{turb}) = A^x \sum_n \alpha^{(n)} F^{(n)}, \tag{2.17a}$$

$$\partial_z(\tau^y_{turb}) = A^y \sum_n \alpha^{(n)} F^{(n)}, \tag{2.17b}$$

$$\sum_n \alpha^{(n)^2} = 1, \tag{2.17c}$$

where the symbols $A^x = A^x(t)$ and $A^y = A^y(t)$ represent mode-independent amplitudes associated with the zonal and meridional directions. Using (2.16a)-(2.16d) and (2.17a)-(2.17c), we revisit the depth integral of the square of each of the zonal and meridional components of the wind-induced force to yield,

$$\int_{-H_{bottom}}^{0} (\partial_z(\tau^x_{turb}))^2 \, dz = (A^x)^2 H_{bottom} \left(\sum_n \alpha^{(n)^2} \right) = (A^x)^2 H_{bottom}, \tag{2.18a}$$

$$\int_{-H_{bottom}}^{0} (\partial_z(\tau^y_{turb}))^2 \, dz = (A^y)^2 H_{bottom} \left(\sum_n \alpha^{(n)^2} \right) = (A^y)^2 H_{bottom}. \tag{2.18b}$$

The set of (2.15a)-(2.15b) and (2.18a)-(2.18b) determines an analytical expression for the mode-independent amplitudes as follows,

$$A^x = \tau^x_{wind} / \sqrt{H_{mix} H_{bottom}}, \tag{2.19a}$$

$$A^y = \tau^y_{wind} / \sqrt{H_{mix} H_{bottom}}. \tag{2.19b}$$

We now project the vertical profile of the wind-induced force based on (2.17a)-(2.17b) to the eigenfunction of each baroclinic mode to read,

$$\int_{-H_{bottom}}^{0} (\partial_z(\tau^x_{turb})) F^{(n)} \, dz = A^x H_{bottom} \alpha^{(n)} = \tau^x_{wind} \sqrt{H_{bottom}/H_{mix}} \, \alpha^{(n)}, \tag{2.20a}$$

$$\int_{-H_{bottom}}^{0} (\partial_z(\tau^y_{turb})) F^{(n)} \, dz = A^y H_{bottom} \alpha^{(n)} = \tau^x_{wind} \sqrt{H_{bottom}/H_{mix}} \, \alpha^{(n)}, \tag{2.20b}$$

where (2.16b) and (2.19a)-(2.19b) have been used. Substitution of (2.13a)-(2.13c) to (2.20a)-(2.20b) yields an analytical expression for the nondimensional coefficient $\alpha^{(n)}$ to read,

$$\alpha^{(n)} = \int_{-H_{mix}}^{0} F^{(n)} \, dz / \sqrt{H_{bottom} H_{mix}}, \tag{2.21}$$

which has been estimated in the present study using the set of eigenfunctions associated with the climatological annual-mean stratification of the tropical IO (see Fig. 2.1c) to yield 0.35, 0.44, and 0.27 for the first, second, third baroclinic modes, respectively, as listed in Table 2.1.

2.3 Results and Discussion

2.3.1 Simulated results

We first present a brief overview of the results of our numerical experiments in order to understand how they reproduce or differ from the actual variations taking place in the IO. Figure 2.2 shows a set of Hovmöller diagrams at the equator for all three baroclinic modes. The Wyrtki jets are simulated in the second baroclinic mode (Fig. 2.2c, g) as shown by the time evolution of zonal velocity, with eastward wind-forcing peaks present in both April–June and October–December (contours in the left panels of Fig. 2.3) (Gent *et al.,* 1983, Nagura and McPhaden, 2010). The second baroclinic mode has a basin-mode period of 0.46 years (Table 2.1) and so is able to respond to the semi-annual wind-forcing at the equator. While the time evolution of zonal velocity shows more westward propagating signals at the equator (color shading in the left panels of Fig. 2.3), the time evolution of the geopotential anomaly shows some of eastward propagating signals at the equator (color shading in the right panels of Fig. 2.3). The significance of simulated Yanai waves (also known as mixed RGWs) (Yanai and Maruyama, 1966) may be verified by looking at the time evolution of the meridional velocity (contours in the right panels of Fig. 2.3) in which these waves are shown to be less relevant than RWs and KWs in the equatorial region of our model experiments. Hereafter our explanation focuses on either KWs or RWs.

The horizontal distributions of experimental results for the second baroclinic mode (Fig. 2.1) illustrate the annual variations taking place in the IO. The model results reproduce the SC along the African coasts. The variations of the SC are related to the interactions in the tropical-extratropical IO. The results also illustrate how a large-scale monsoon leads to the formation of the SC. In boreal winter along the African coasts (Fig. 2.1a), the southward signals of the SC originate from the NMC while the northward signals of the EACC originate from the SEC (SM01; Schott, 1986; Nagura and Masumoto, 2015). These equatorward

boundary currents meet each other around the equator to turn eastward as the SECC (Düing and Schott, 1978; Swallow *et al.,* 1991), in such a way as to relax negative geopotential anomaly in the western equatorial region (Fig. 2.1b). With the onset of the boreal summer monsoon, southwesterly winds induce a strong northward EACC flowing along the African coasts (Fig. 2.1e). As this crosses the equator, it turns offshore and starts to flow eastward towards the Arabian Sea. The southwesterly winds give rise to coastal upwelling near the African coasts, as shown by negative geopotential anomaly in Fig. 2.1f. These results demonstrate that several of the basic features of the climatological circulation and wave evolution in the IO have been captured by our model experiments.

2.3.2 Transfer routes of wave energy

We have analyzed the directionality of wave group velocity vectors in order to understand the transfer routes of wave energy throughout the IO. Figure 2.4 shows energy flux vectors associated with the second baroclinic mode (left panels), and the third baroclinic mode (right panels), all of which have been calculated by applying an annual average to all 100 snapshots during the 20th year of model integrations. This figure allows us to compare the performance of the pressure-flux scheme, the OS93 scheme, and the AGC17 scheme. The pressure-flux scheme (Fig. 2.4a, b) does not show the westward transfers of wave energy associated with mid-latitude RWs, while the OS93 scheme (Fig. 2.4c, d) cannot reveal energy fluxes in the vicinities of the equator or coastlines. In contrast, the AGC17 scheme (Fig. 2.4e, f) is able to show both westward energy fluxes associated with mid-latitude RWs and eastward energy fluxes associated with equatorial KWs. The AGC17 scheme is also able to identify the equatorward energy fluxes along the coastlines of the African continent. Contours in Fig. 2.4 show an annual-mean input of wave energy by wind-forcing. The wind input has a positive peak north of the equator at around 85°E in both second and third baroclinic modes (see contours in Fig. 2.4). This result indicates that mid-latitude RWs in this

region are revived by local wind-forcing. The wind input shows alternating signals in the other regions, owing to the phase relationship between waves and annual forcing. Further details of the wind input are provided later in the manuscript.

Based on this annual-mean analysis (Fig. 2.5a, b), our results suggest the presence of two sets of cyclonic circulations of wave energy in each hemisphere (green arrows in Fig. 2.5c). These are listed as:

- Localized cyclonic circulation close to the African coasts.
- Large-scale cyclonic circulation in the eastern side of the basin.

Near the western boundary of the IO, the seasonal variations of both the SC and the EACC generate equatorward energy fluxes along the African coasts, forming a localized cyclonic energy circulation in each hemisphere. Identification of this energy circulation has been facilitated by the fact that the AGC17 scheme has the advantage of satisfying the coastal boundary conditions. Thus the AGC17 scheme generates no energy flux in the direction normal to model coastlines, which stands in contrast to the OS93 scheme. The net equatorward transports of wave energy at the western boundary of the IO in the northern and southern hemispheres have been estimated as –3.59 and 2.07 GW (giga watts), respectively. As equatorial KWs arrive at the eastern boundary, they bifurcate polewards along the coasts of the Indonesian Peninsula and Islands and then radiate mid-latitude RWs to form a basin-scale cyclonic circulation of wave energy in each hemisphere (Fig. 2.5a–c). The net transports of wave energy bifurcating northward and southward at the eastern boundary of the IO have been estimated as –0.87 and 0.96 GW, respectively. These values indicate that about 1/3 ($\approx$ (0.87+0.96)/(3.59+2.07)) of the wave power from the western boundary continues eastward across the zonal extent of the IO at the equator. The northward branch at the eastern boundary reaches the Andaman Sea, and then turns westward into the Bay of Bengal, while the southward branch at the eastern boundary reaches the coasts of Australia, and then turns

northwestwards into the southern IO. The distribution of the energy-flux divergence (color shading in Fig. 2.5d) shows meridionally alternating signals that correspond to the distribution of wave energy input by wind forcing (Fig. 2.5e). The energy-flux divergence is nearly zero in the eastern equatorial regions (Fig. 2.5d), indicating that KW energy is transferred polewards rather than dissipated locally. Indeed, energy dissipation is significant near the western boundaries where the horizontal scale of the disturbances is relatively small, owing to the presence of coastal currents (Fig. 2.5f). The details of these issues will be investigated in a future study based on both regional statistics and model intercomparisons.

The eastward energy fluxes along the equator in Fig. 2.4 are attributed to equatorial KWs. These warrant further investigation because eastward propagating signals are less pronounced in both the Hovmöller diagrams of zonal velocity and geopotential anomaly (i.e. raw quantities from the model output) in Fig. 2.3. We have computed the energy quantities without a time average to analyze the time evolution of energy flux at the equator and at 5°N, as shown in Fig. 2.6. The AGC17 scheme can identify the eastward transfers of wave energy that are consistent with the group velocity of equatorial KWs (see solid blue lines in Fig. 2.6). In relation to the seasonal evolution in the second baroclinic mode (Fig. 2.6c), eastward signals are found to culminate (four times per year with a maximum in April–May) when zonal velocity exhibits eastward and westward peaks as dictated by the monsoon winds. The timings of wind input at the equators (see contours in Fig. 2.6c) are such as to intensify the eastward energy fluxes associated with equatorial KWs in the central basin. Signals indicating eastward energy fluxes are found to span the full zonal extent of the tropical IO, which may be traced back to the reflection of RWs at the western boundary. For the first and third baroclinic modes, eastward signals can be recognized in the eastern and western regions of the basin, respectively. In the western basin, all three baroclinic modes indicate wave energy input by wind forcing, with semi-annual peaks that are attributed to the influence of

the monsoon. This wind forcing near the African coast modulates strengths among four KW beams in a year.

Likewise, when used without a time average, the AGC17 scheme can identify the westward transfers of wave energy that are consistent with the group velocity of both long equatorial RWs (see solid blue lines in the left panels of Fig. 2.6) and mid-latitude/off-equatorial RWs (the right panels of Fig. 2.6). Overall, the westward energy fluxes (appearing four times per year) are less powerful than the eastward energy fluxes. Equatorial RWs in the western basin originate from wind input in the central basin. Namely wind input at the equator induces both KWs and RWs at the same time. The fact is that KWs reflected from the western boundary arrive at the central basin at times of wind input is explained by the basin mode period of about half a year in the second baroclinic mode. Figure 2.6 clearly resolves both wave reflection at the western boundary and wave diffraction at the eastern boundary. The wind input at 5°N (contours in Fig. 2.6d) is more significant than at the equator (contours in Fig. 2.6c) in the central basin, the former of which corresponds to the wind input peak surrounding the Maldives (from 60°E to 80°E) in the horizontal distribution based on an annual average (color shading in Fig. 2.5e). The presence of wind input in this region may be confirmed by positive signals in the energy-flux potential (contours in Fig. 2.5d). These results illustrate how oceanic waves are linked to each other and where these waves originate from. Reflection and diffraction at the zonal boundaries yield the cyclonic circulations of wave energy in each hemisphere, and in turn these lead to tropical-extratropical exchanges of wave energy.

2.4 Conclusion

The exchange of wave energy in tropical-extratropical regions has so far remained poorly understood owing to the lack of appropriate diagnostic techniques. The present study has compared three diagnostic schemes to identify the transfer routes of wave energy that

theoretically follow group velocity vectors. The pressure-flux scheme cannot represent the westward energy flux of mid-latitude RWs, the quasi-geostrophic scheme can be used for mid-latitude RWs though not for equatorial KWs or coastal regions. Only the AGC17 scheme has enabled a unified treatment of RWs and KWs, and thus allowed us to determine the horizontal transfer routes of wave energy with a smooth transition between tropical and subtropical regions. We conclude that the AGC17 scheme is the most appropriate for tracing the processes of reflection and diffraction of all waves and at all latitudes, while also satisfying the coastal boundary conditions.

This is the first time that the new seamless diagnostic scheme for tracing wave-energy fluxes has been used to investigate realistic circulations and waves in the IO. We have focused here on the well-defined seasonal variations associated with the monsoon, and performed a set of shallow-water model experiments using climatological wind-forcing. In the Hovmöller diagrams of both zonal velocity and geopotential anomaly at the equator (Fig. 2.3), eastward signals related to KWs are less pronounced while westward signals related to RWs are clearly revealed. Near the western boundary of the IO, the seasonal variations of both the SC and EACC are found to generate equatorward energy fluxes along the African coasts, forming a previously undetermined localized cyclonic energy circulation in each hemisphere. About 1/3 of this western-boundary wave power continues eastward across the zonal extent of the IO at the equator. Near the eastern boundary of the IO, the incoming signals of equatorial KWs bifurcate polewards along the coasts of the Indonesian Peninsula and Islands and then transmit mid-latitude RWs, forming a basin-scale cyclonic energy circulation in each hemisphere. Application of the AGC17 scheme without a time average yields eastward transfers of wave energy associated with KWs that are consistent with the theoretical value of group velocity. Interestingly, the eastward energy fluxes of equatorial KWs appear when zonal current anomalies exhibit eastward and westward peaks (four times

per year in response to the cycle of the monsoon winds) with a maximum in April–May. The details of these issues will be investigated in a future study based on both regional statistics and model intercomparisons. For example, the impact of the Indonesian Throughflow on wave energetics presents an important challenge for the future. Our analysis of annual and semi-annual waves provides a basis for a future investigation of waves that vary on interannual timescales and so should lead to a better understanding of tropical-extratropical interactions during, for example, periods when the IO Dipole is active. Such research themes/topics have a direct relevance to the issue of climate variation.

Table 2.1 List of experiment parameters. The basin-mode period is defined as $4L/c^{(n)}$ where L= 6110 km is the zonal distance of the Indian Ocean at the equator (from 45°E–100°E). The wind-coupling thickness is defined as $\sqrt{H_{mix}H_{bottom}}/\alpha^{(n)}$.

baroclinic mode	1st	2nd	3rd
gravity wave speed (m/s)	2.99	1.69	1.03
equatorial deformation radius (km)	362	272	212
equatorial inertial period (day)	8.8	11.7	15.0
basin-mode period (year)	0.26	0.46	0.75
$\alpha^{(n)}$ (non-dimensional)	0.35	0.44	0.27
wind-coupling thickness (m)	1264	991	1653

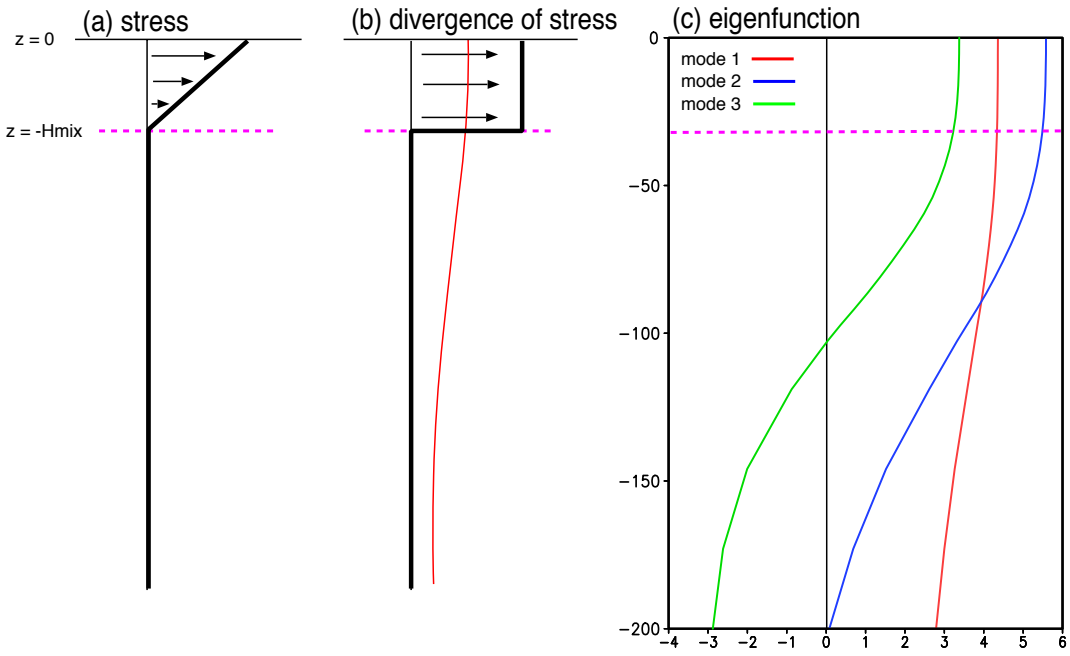

Figure 2.1 Schematic illustration for the vertical profiles of quantities associated with momentum input by wind forcing. (a) Idealized vertical stress caused by three-dimensional turbulence in the surface mixed-layer where H_{mix} is the mixed-layer depth. (b) The vertical divergence of the turbulent stress that may be interpreted as a vertically stepped body force to the horizontal component of momentum. (c) Eigenfunctions associated with the first (red line), second (green line), and third (blue line) baroclinic modes in the tropical Indian Ocean, calculated by solving the Sturm-Liouville problem.

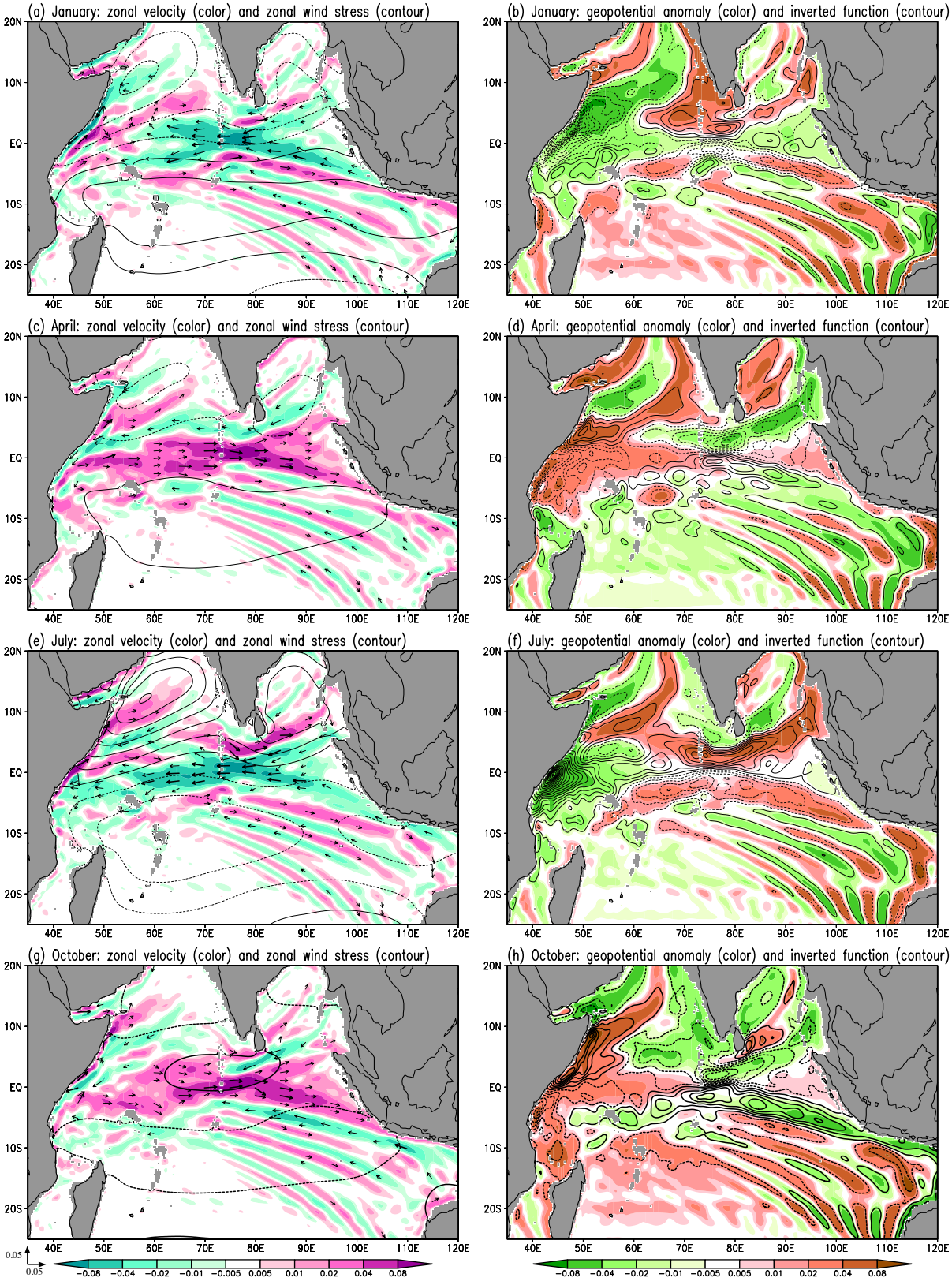

Figure 2.2 Snapshots in the middle of (a, b) January, (c, d) April, (e, f) July, and (g, h) October during the 20th year of the model experiment for the second baroclinic mode. Left panels: simulated velocity vectors with the magnitude being indicated by either the length of arrows (for ranges less than

0.05 m/s) or thick arrows with a constant length (for greater ranges) and the zonal component of simulated velocity (color shading with a unit of meter per second). Contours in the left panels show the zonal component of wind stress (solid and dotted contours for eastward and westward anomalies, respectively, with an interval of 0.02 N/m^2). Right panels: simulated geopotential anomaly (color shading with a unit of meter per second, rescaled as $p^{(n)}/c^{(n)}$ to follow the definition of gravitational potential energy) and the PV-inverted function calculated from Eq. (16b) (solid and dotted contours represent positive and negative values, respectively, with an interval of 2,000 m^2/s). The PV-inverted function may be interpreted as geostrophic stream function in off-equatorial regions.

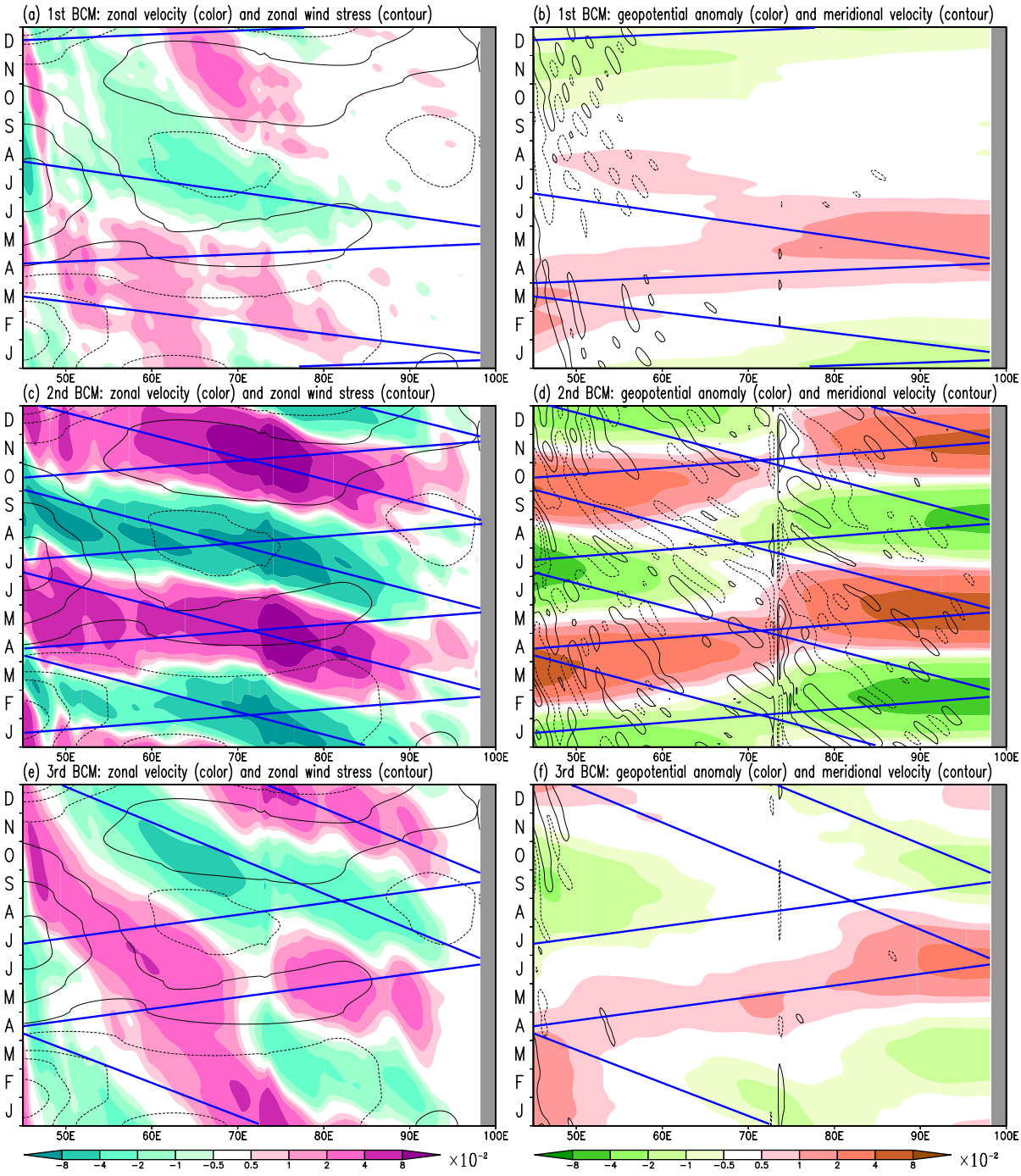

Figure 2.3 Hovmöller diagrams at the equator for the results of model experiments associated with (a, b) the first baroclinic mode, (c, d) the second baroclinic mode, and (e, f) the third baroclinic mode. Left panels (a, c, e): the zonal component of simulated velocity (color shading with a unit of m/s) and the zonal component of wind stress (solid- and dotted-contours for positive and negative values, respectively, with an interval of 0.01 N/m^2) as the part of the model forcing. Right panels (b, d, f): simulated geopotential anomaly (color

shading with a unit of m/s, rescaled as $p^{(n)}/c^{(n)}$ to follow the definition of gravitational potential energy) and the meridional component of simulated velocity (solid- and dotted-contours represent positive and negative values, respectively, with an interval of 0.02 m/s). Blue-solid lines indicate the theoretical phase speeds of both KWs and equatorial long RWs for each baroclinic mode.

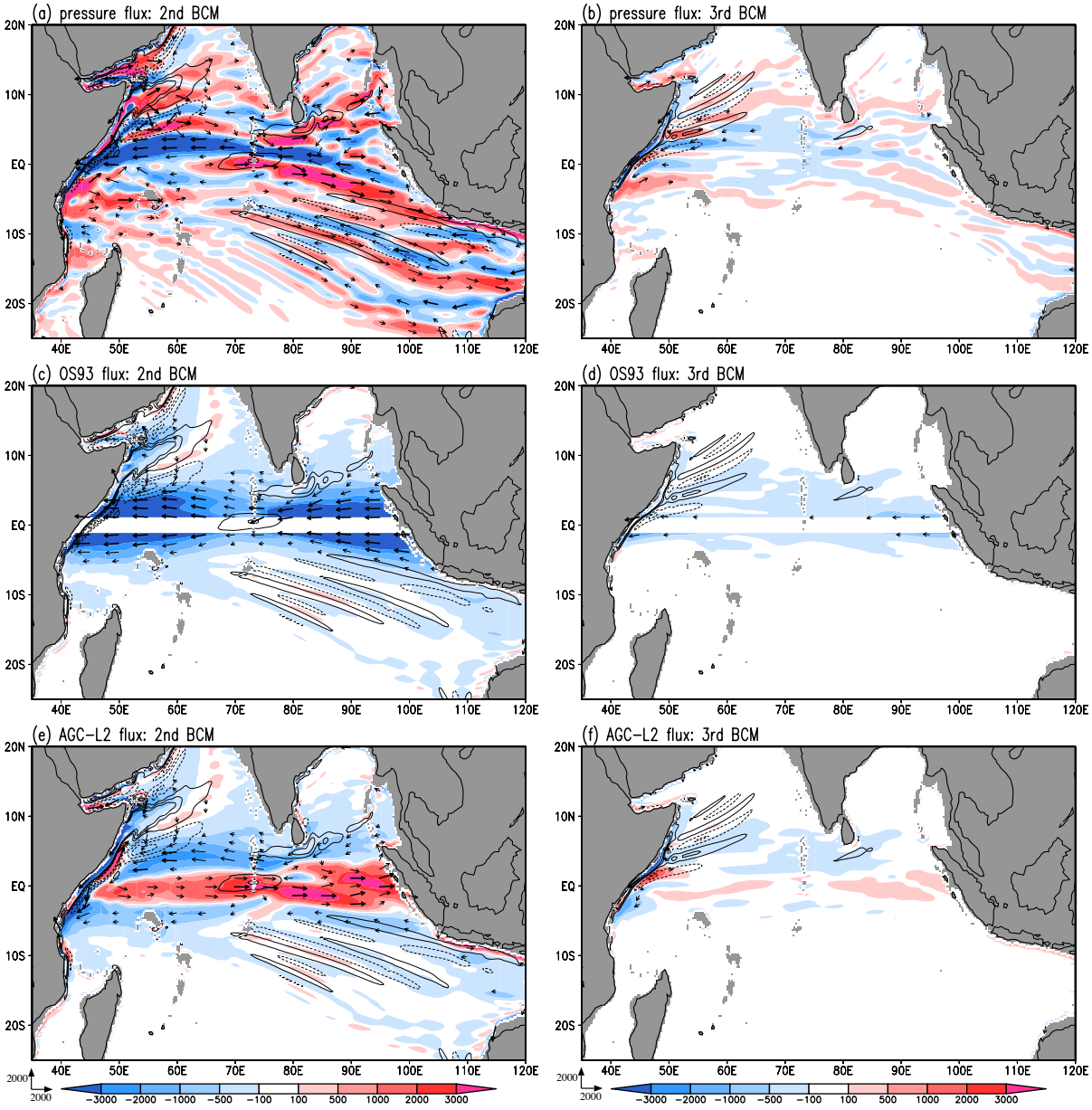

Figure 2.4 Arrows: energy flux vectors estimated using (a, b) the pressure flux scheme, (c, d) the Orlanski and Sheldon scheme, and (e, f) the Aiki, Greatbatch, and Claus scheme (level-2) with magnitude being indicated by either the length of arrows (for ranges less than 2000 W/m) or thick arrows with a constant length (for greater than 2000 W/m). Left panels (a, c, e): the second baroclinic mode. Right panels (b, d, f): the third baroclinic mode. Color shading shows the zonal component of energy flux with a unit of W/m. Contours indicate wave energy input by wind-forcing (solid- and dotted-contours for positive and negative

values, respectively, with an interval of 0.002 W/m^2). All quantities in all panels have been calculated using an annual average.

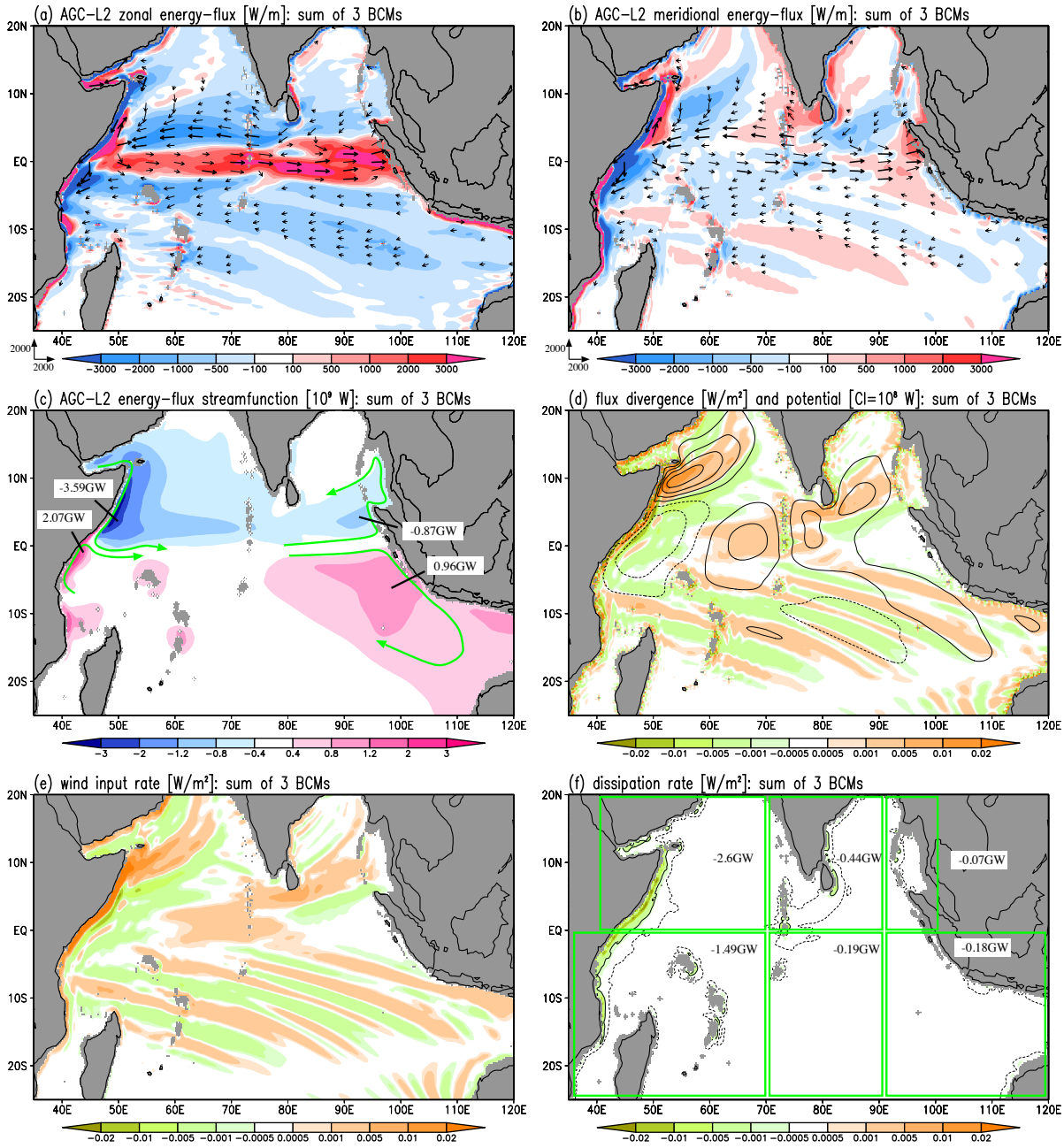

Figure 2.5 Energy quantities based on an annual average and the sum of fundamental three baroclinic modes. (a) Energy flux vectors with magnitude indicated by either the length of arrows (for ranges less than 2000 W/m) or thick arrows with a constant length (for greater ranges) and the zonal component of the energy flux (color shading with a unit of W/m) that have been estimated using the AGC17 scheme (level-2). (b) Same as (a) except for color shading showing the meridional component of the energy flux. (c) Energy-flux streamfunction R (color shading with a unit of 10^9 W= giga watts), with four numbers

indicating locally peak values. Green arrows in (c) represent schematic illustrations for the cyclonic circulations of wave energy in each hemisphere. (d) Energy-flux divergence and energy-flux potential D (solid- and dotted-contours for positive and negative values, respectively, with an interval of 10^8 W= 0.1 giga watts), (e) energy input rate by wind forcing calculated from Eq. (1.1c), and (f) energy dissipation rate calculated from Eq. (1.1d) (color shading with a unit of W/m^2). Solid- and dotted-contours in (f) indicate dissipation rates of $-10^{-3}$and -10^{-4} W/m^2, respectively. Spatially integrated values of the dissipation rate are noted for the boxed subdomains in (f).

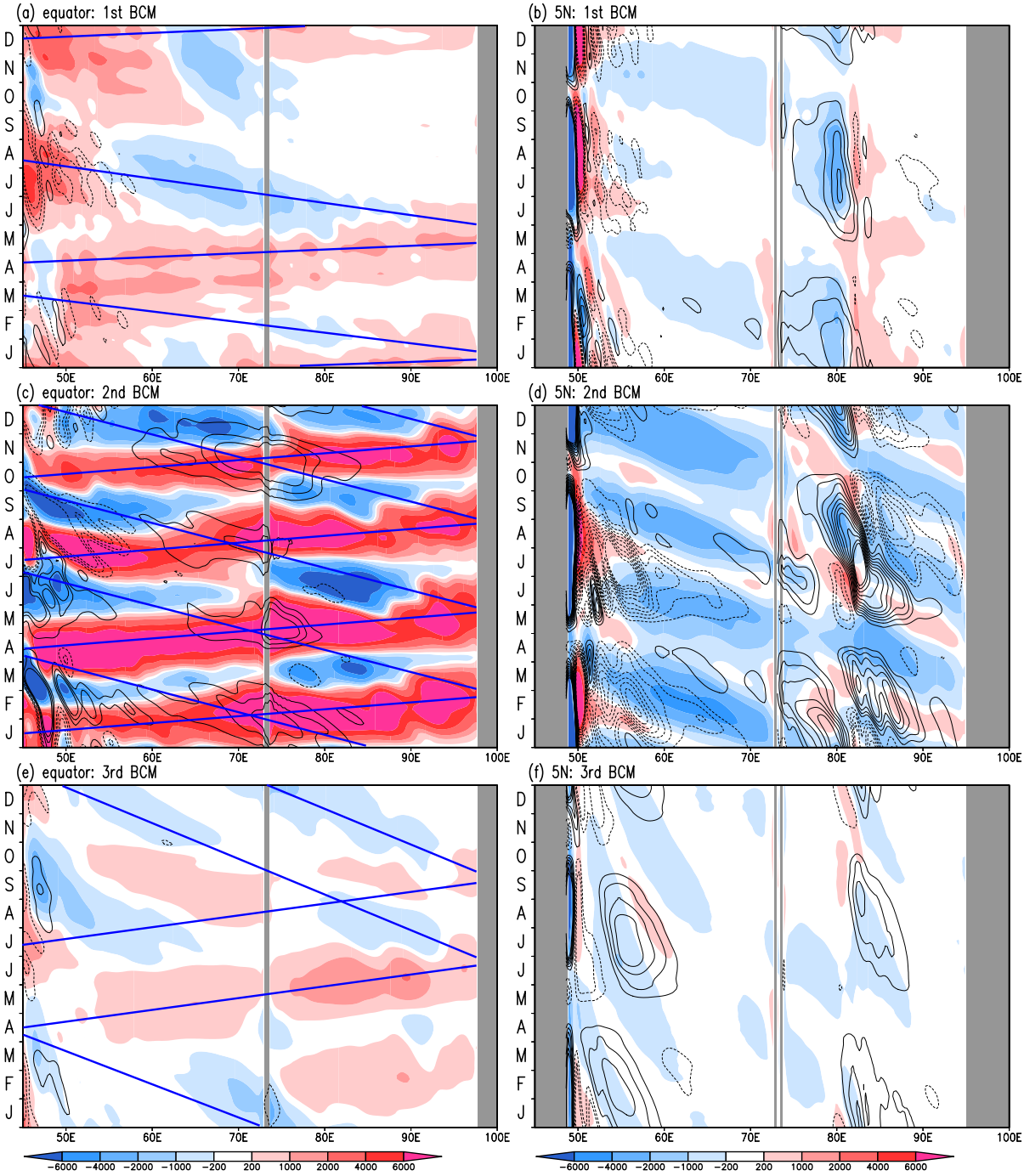

Figure 2.6 Hovmöller diagrams at the equator (left panels) and at 5°N (right panels) for the results of model experiments associated with (a, b) the first baroclinic mode, (c, d) the second baroclinic mode, and (e, f) the third baroclinic mode. Color shading shows the zonal component of the energy flux (color shading with a unit of W/m) computed using the AGC17 scheme (level-2) without a time average. Solid blue lines in the left panels indicate the

theoretical phase speeds of both KWs and equatorial long RWs for each baroclinic mode. Contours show energy input by wind-forcing (solid- and dotted-contours for positive and negative values, respectively, with an interval of 0.002 W/m^2).

Chapter 3

The vertical structure of annual wave energy flux in the tropical Indian Ocean

3.1 Introduction

In the tropical regions, the dynamics of the atmosphere-ocean interactions dictating the growth and morphology of large-scale surface currents strongly depend on subsurface oceanic structure. In turn, variability in the surface currents themselves can induce deep and persistent flows which remain trapped along the equator (Luyten and Swallow, 1976; Hayes and Milburn, 1979; McCreary, 1984; Rothstein *et al.,* 1985; Kessler and McCreary, 1993; Dewitte and Reverdin, 2000). In the central equatorial IO, wind forcing develops on a semiannual timescale. Further to the west and in the regions off equator, the monsoonal phase transition produces a seasonal cycle in wind forcing (Reppin *et al.,* 1999; Schott and McCreary, 2001). The former semiannual wind forcing induces equatorial KWs with a downwelling phase in the surface layer in both boreal spring and autumn and a corresponding upwelling phase in both boreal winter and summer, leading to an eastward transfer of wave energy four times per year (Li and Aiki, 2020, hereafter LA20). Striking the eastern boundary of the tropical IO, KWs are first retro-reflected, then diffracted poleward and subsequently radiate westward-propagating equatorial and midlatitude RWs (Mark and Huang, 2004; Han, 2005; Fu, 2007).

Previous studies have investigated the vertical propagation of equatorial KWs and RWs in the Pacific and Atlantic Oceans on intraseasonal to interannual time scales (McPhaden, 1982; Lucas and Firing, 1985; McPhaden and Ripa, 1990; Kessler and McCreary, 1993; Brandt and Eden, 2005; Thierry *et al.,* 2006; Ishizaki *et al.,* 2014). Vertically propagating waves are also observed in the tropical IO. Owing to the dominance of

semiannual wind forcing, variability in mid-depth of the equatorial IO below the main pycnocline is characterized by semiannual variability (Luyten and Roemmich, 1982; Nagura and McPhaden, 2016; Huang *et al.*, 2018a, 2018b; Zanowski and Johnson, 2019; Chen *et al.,* 2020). They consist of equatorial KWs and long RWs, which carry energy to the east and to the depth, and to the west and to the depth, respectively. Waves are reflected at the eastern and western boundaries of the IO, and boundary generated waves further propagate downward (Nagura and McPhaden, 2016; Huang *et al.,* 2020). In particular, mooring observations in the southern Bay of Bengal (SBoB) at 5°N, 90.5°E show a robust half-year cycle between 200 and 1200 m depth (Huang *et al.,* 2019). The subsurface mooring at the same location used in Chen *et al.* (2017) reveals remarkable intraseasonal meridional currents across SBoB that are attributed to westward-propagating RWs. In the off-equatorial region, variability below the pycnocline has annual periodicity, owing to the predominance of annual wind forcing related to monsoon (Johnson, 2011; Nagura, 2018; Huang *et al.,* 2020).

These previous studies examined vertical propagation of waves using ray tracing technique and/or vertical mode decomposition. Ray tracing technique requires the assumption that the WKB approximation is valid, i.e., the vertical scale of variation in buoyancy frequency is larger than vertical wavelength of waves. This assumption is generally satisfied below the pycnocline, but not in and above the pycnocline. Owing to this, energy propagation cannot be traced from the surface, where winds excite wave energy, to the depth below the pycnocline using ray tracing technique. This raises an essential difficulty in interpreting the generation mechanism of mid-depth waves. Vertical mode decomposition does not require such an assumption, but vertically propagating waves consist of multiple baroclinic modes, and examination of each baroclinic mode is not informative about vertical propagation. An alternative is sensitivity experiments using a numerical model, but this method is relatively expensive computationally.

These problems can be solved by the use of energy flux newly defined by Aiki *et al.* (2017; hereafter AGC17) and Aiki *et al.* (2021; hereafter JAS21). Their scheme does not use the WKB approximation and is applicable seamlessly to depths above, in and below the pycnocline. It does not require quasi-geostrophy and covers variability both in the equatorial and subtropical regions. It does not require Fourier transform either and thus can be used in coastal regions. The scheme is diagnostic and provides a computationally cheaper way compared to sensitivity experiments using an elaborated numerical model. The AGC17 scheme allowed Ogata and Aiki (2019), LA20, Song and Aiki (2020), and Toyoda *et al.* (2021) to obtain wholly new perspectives on the horizontal transfer routes of waves in the tropical oceans. We extend their work to a three-dimensional system and describe vertical wave propagation.

The depth-dependent version of the seamless AGC17 scheme has not been applied to the analysis of oceanic waves before the present study. Our initial focus will mainly be on seasonal variability in the IO, while interannual variations will be investigated in future work. The manuscript is laid out in the following fashion: section 3.2 describes the formulation of an adopted model, method for energy flux computation and temporal and spatial characteristics of simulated fields. Section 3.3 provides an analysis of the vertical structure of energy fluxes associated with KWs and RWs, while section 3.4 gives a summary of the main results.

3.2 Materials and methods

AGC17 employed a single-layer system based on the shallow-water equations to derive depth-independent expressions of the energy flux. As it has the advantage of a smooth tropical-subtropical transition, the AGC17 scheme can effectively determine the horizontal distribution of energy flux pointing in the direction of group velocity of waves. JAS2021 have extended the formulation of AGC17 to cover the case of a baroclinic system in the

atmosphere. Their essential contribution is the derivation of the exact expression of the vertical component of energy flux (this is not described in the present manuscript). The expressions given below for the horizontal component of depth-dependent energy flux represent a straightforward extension of the content of AGC17 and are summarized below by the adoption of an oceanic framework that the general reader should find convenient.

3.2.1 Model set-up

We simulated climatological variability in the IO using a linear ocean model (LOM). The model has been discretized in a spherical coordinate system with a grid spacing of (1/4)° in both zonal and meridional directions. The model domain extends from 35°–120°E and from 25°S–20°N and adopts realistic coastlines except for the lack of connection to the Southern Ocean and the Pacific Ocean. The LOM is written for the development of zonal velocity $u^{(n)}(x, y, t)$, meridional velocity $v^{(n)}(x, y, t)$, and geopotential $\Phi^{(n)}(x, y, t)$ associated with the generic *n*-th baroclinic mode. For each baroclinic mode these are related through

$$u_t^{(n)} - fv^{(n)} + \Phi_x^{(n)} = \alpha^{(n)} \frac{\tau^x}{\rho_0 \sqrt{H_{mix} H_{bottom}}} + \mathrm{SGS}^x, \tag{3.1a}$$

$$v_t^{(n)} + fu^{(n)} + \Phi_y^{(n)} = \alpha^{(n)} \frac{\tau^y}{\rho_0 \sqrt{H_{mix} H_{bottom}}} + \mathrm{SGS}^y, \tag{3.2b}$$

$$\Phi_t^{(n)} + (c^{(n)})^2 (u_x^{(n)} + v_y^{(n)}) = 0, \tag{3.3c}$$

where horizontal and temporal partial derivatives are denoted by subscripts *x*, *y* and *t* respectively. *f* denotes the Coriolis coefficient. $\rho_0 = 1027$ kg/m^3 is the reference value of water density. The vector (τ^x, τ^y) represents wind stress. The mode-dependent parameters $\alpha^{(n)}$ and $c^{(n)}$ have been calculated in the present study using the climatological annual-mean stratification of the tropical IO (explained later in this section). The definition of $\alpha^{(n)}$ is described in detail in section 2.2.3. The values of $\alpha^{(n)}$ and $c^{(n)}$ used in the present study are

given in Table 3.1. The present study defines the mixed layer depth as the depth where temperature is lower than the surface by 0.2°C and calculated it using Argo float data. From the resulting annual mean of mixed layer depth in the tropical IO, we set $H_{mix} = 35\ m$. H_{bottom}= 5500 m represents the reference depth of the bottom of the ocean in the tropical IO. The subgrid-scale terms, which are labelled as SGS in (3.1a) and (3.1b), indicate the effect of lateral eddy viscosity applying the Smagorinsky *et al.* (1965) scheme with a nondimensional coefficient of 0.1 after squaring.

Reconstruction of vertical profile based on the output of LOM is done by using the eigen vectors, as in previous studies. While LA20 executed a series of numerical experiments focusing on the first three baroclinic modes which assumed no motion at the bottom, the present study has investigated the first six baroclinic modes under the assumption of a free-slip bottom boundary (Chelton and Schlax, 1996; see below). The first six modes explain about 80% of baroclinic kinetic energy fraction in the equatorial regions of a global ocean reanalysis, as shown by Fig. 1 in Toyoda *et al.* (2021). The Sturm-Liouville equation for the baroclinic normal-mode decomposition associated with a stratified ocean may be written as

$$(F_z^{(n)}/N^2)_z = \frac{-1}{(c^{(n)})^2} F^{(n)}, \tag{3.2}$$

where $F^{(n)} = F^{(n)}(z)$ and $c^{(n)}$are the eigenfunction and non-rotating gravity wave speed, respectively, of the *n*-th baroclinic mode. The symbol $N = N(z)$ in (3.2) is the buoyancy frequency which we have given based on the vertical profiles of climatological annual mean salinity and temperature in the tropical IO (20°S–20°N, 40°E–110°E) from the World Ocean Atlas. We have solved (3.2) using a Neumann boundary condition, $F_z^{(n)} = 0$, at both the surface and bottom of the ocean and obtained $c^{(n)}$ =2.63 m/s, 1.57 m/s, 0.956 m/s, 0.706 m/s, 0.557 m/s, 0.467 m/s for the first six baroclinic modes. The vertical profiles of the eigenfunctions are shown in Fig. 3.1 where $\int_{-H_{bottom}}^{0} (F^{(n)})^2\, dz = H_{bottom}$ and bottom depth

$H_{bottom} = 5500$ m. The parameter $\alpha^{(n)}$ of wind forcing partition in (3.1a)–(3.1b) has been determined in the same manner as that in LA20.

McCreary (1984) demonstrated that the vertical propagation related to equatorial waves can be described by the sum of baroclinic modes. The present study has reconstructed the vertical structure of the tropical IO by using the results of model experiment associated with fundamental six baroclinic modes. Quantities in the depth coordinate, such as geopotential $\Phi(x, y, z, t)$, zonal velocity $u(x, y, z, t)$, meridional velocity $v(x, y, z, t)$, and vertical velocity $w(x, y, z, t)$, are obtained as,

$$\Phi(x, y, z, t) = \sum_n \Phi^{(n)}(x, y, t) F^{(n)}(z), \tag{3.3a}$$

$$u(x, y, z, t) = \sum_n u^{(n)}(x, y, t) F^{(n)}(z), \tag{3.3b}$$

$$v(x, y, z, t) = \sum_n v^{(n)}(x, y, t) F^{(n)}(z), \tag{3.3c}$$

$$w(x, y, z, t) = \sum_n \frac{-1}{N^2} [\frac{\partial}{\partial t} \Phi^{(n)}(x, y, t)][\frac{\partial}{\partial z} F^{(n)}(z)], \tag{3.3d}$$

and have been applied to each of the 100 snapshots obtained from the final year of model output.

The LOM model yields both the three-dimensional and baroclinic-mode profiles of velocity vector and geopotential, that is aimed at facilitating our analysis of simulated wave dynamics. This kind of model has been used by previous studies to examine vertical propagation of waves (Huang *et al.,* 2018a, 2019, 2020; Chen *et al.,* 2020) and is dynamically consistent with our formulation of energy flux that is derived from linear equations. The wind forcing for the model is derived from the 10-m wind data of the European Centre for Medium-Range Weather Forecasts Re-analysis (ECMWF ERA-40) by applying the Large and Pond (1981) bulk formula to wind data from September 1957 to August 2002. While the experiments described in LA20 assumed no motion near the ocean bottom and examined the first three baroclinic modes, here we assume a free-slip bottom boundary condition (Chelton and Schlax, 1996) as in traditional studies and focus on the first six baroclinic modes. This

change of model setup is required in order to investigate the vertical propagation of waves in the present study. Each of our six numerical experiments involved integration over a period of 20 years (inclusive of the spin-up phase from a state of no motion). Investigation of the fundamental baroclinic modes begins when the system reaches a confirmed climatological equilibrium. The subsequent analysis is then based on the final 100 "snapshots" of model output. Since these are separated by 3.65 days, we make use of data from the last year of each run. Below, all results are shown in the depth coordinate, which are reconstructed from the model outputs of the first six baroclinic modes. The result of the LOM experiment is justified in the next subsection by comparing with the output from a high-resolution climatological Ocean General Circulation Model (OGCM) simulation for the semi-global ocean. We have used monthly current and wind stress data derived from the OGCM For the Earth Simulator (OFES) forced by National Centers for Environmental Prediction winds (Masumoto *et al.,* 2004). OFES is on the basis of Modular Ocean Model version 3. The output is monthly mean during the last six years (from 45yr to 50yr) of 50-year climatological integration with a horizontal resolution of $0.1° \times 0.1°$ and 54 vertical levels.

3.2.2 Diagnostic scheme of wave energy flux

In order to investigate the vertical structure of energy transfers, we aim to derive depth-dependent expressions of energy flux. We use the primitive equations for a Boussinesq fluid on an equatorial β-plane (Gill, 1982) appropriate for linear waves propagating in a rotating frame of reference and with zero mean flow. Let x, y, z, and t define independent variables in a Cartesian co-ordinate system and increase eastward, northward, and vertically upward respectively. The quantities u, v and w represent the corresponding three-dimensional components of velocity (a full list of variables is given in Table 2). The equations may then be written as,

$$\frac{\partial u}{\partial t} - fv + \frac{\partial \Phi}{\partial x} = 0, \tag{3.4a}$$

$$\frac{\partial v}{\partial t} + fu + \frac{\partial \Phi}{\partial y} = 0, \tag{3.4b}$$

$$\frac{\partial \Phi}{\partial z} = -g\frac{\rho}{\rho_0}, \tag{3.4c}$$

$$w = \frac{-1}{N^2}\frac{\partial^2 \Phi}{\partial z \partial t}, \tag{3.4d}$$

$$N^2 = -\frac{g}{\rho_0}\frac{d\bar{\rho}}{dz}, \tag{3.4e}$$

$$\frac{\partial u}{\partial x} + \frac{\partial v}{\partial y} + \frac{\partial w}{\partial z} = 0, \tag{3.4f}$$

where $f = f_0 + \beta y$ is the Coriolis parameter, $\Phi = \Phi(x, y, z, t)$ corresponds to geopotential, and $\rho = \rho(x, y, z, t)$ is the perturbation of potential density. The symbols $N = N(z)$ and g are the buoyancy frequency and the acceleration owing to gravity, respectively. The symbols ρ_0 and $\bar{\rho}(z)$ represent the reference density and the background density, respectively. Manipulation of (3.4a)–(3.4f) yields a prognostic equation for potential vorticity (PV: symbolized as q) to read

$$\frac{\partial}{\partial t}\underbrace{\left[\frac{\partial v}{\partial x} - \frac{\partial u}{\partial y} + \frac{\partial}{\partial z}\left(\frac{f}{N^2}\frac{\partial \Phi}{\partial z}\right)\right]}_{\equiv q} + v\beta = 0. \tag{3.5}$$

This relation is generally applicable for waves at all latitudes, such as midlatitude RWs, midlatitude IGWs, and equatorial waves [i.e. equatorial RWs and IGWs, equatorial RGWs (i.e., Yanai waves) and equatorial KWs (Matsuno, 1966; Yanai and Maruyama, 1966), if we applied it to an equatorial β-plane ($f_0 = 0$)]. Equatorial KWs (i.e., $v = 0$) are characterized by $q = 0$. From (3.4a)–(3.4c), the wave energy density may be represented in prognostic fashion by

$$\frac{\partial}{\partial t}\frac{1}{2}\left[\overline{u^2 + v^2 + \frac{1}{N^2}\left(\frac{\partial \Phi}{\partial z}\right)^2}\right] +$$

$$\nabla \cdot \langle\langle \overline{u\Phi}, \overline{v\Phi}, \overline{w\Phi} \rangle\rangle = 0, \tag{3.6a}$$

where $\nabla \equiv \langle\langle \frac{\partial}{\partial x}, \frac{\partial}{\partial y}, \frac{\partial}{\partial z} \rangle\rangle$ and the overbar signifies phase-averaging (i.e., for a sinusoidal wave, $\bar{A} = 0$ for $A = u$, v, w and Φ), or low-pass time filtering (considering this case we retain the local time derivative in (3.6a), thereby permitting slow time variations in the general case). The energy flux vector in (3.6a)

$$\overline{\mathrm{U}\Phi} = \langle\langle \overline{u\Phi}, \overline{v\Phi}, \overline{w\Phi} \rangle\rangle, \tag{3.6b}$$

is codirectional with the group velocity of midlatitude IGWs in the atmosphere and ocean (Gill, 1982). However, the energy flux of (3.6b) is not aligned with the group velocity of midlatitude RWs (Longuet-Higgins, 1964).

In order to obtain an expression of the energy flux that is codirectional with group velocity of all wave types, AGC17 (and also JAS2021) have revisited the equations to define energy flux of both equatorial and midlatitude waves. The derivation is briefly described below using linear waves on an equatorial β-plane and zero mean flow. Let k, m and ω be zonal and vertical wavenumbers and wave frequency. The zonal component of group velocity of equatorial waves may be written as

$$\frac{\partial \omega}{\partial k} = \frac{2\omega^2 + \omega/k}{2\omega^3 m^2/(kN^2) + 1}, \tag{3.7}$$

which has been written in a dimensional form and m denotes vertical wavenumber.

The group velocity times wave energy density is rewritten in a depth-dependent framework as,

$$\frac{\partial \omega}{\partial k} \frac{1}{2} \overline{\left[u^2 + v^2 + \frac{1}{N^2} \left(\frac{\partial \Phi}{\partial z} \right)^2 \right]} = \overline{u\Phi} + \frac{\partial}{\partial y} \left(\frac{\overline{\Phi\varphi}}{2} + \frac{1}{\beta} \overline{\frac{\partial^2 u}{\partial t^2} \varphi} \right), \tag{3.8a}$$

$$\varphi \equiv \frac{-v_\mu}{k + 2\omega^3 m^2/(\beta N^2)}, \tag{3.8b}$$

where the scalar quantity φ may be referred to as pseudo-streamfunction and the subscript μ signifies partial derivative with respect to wave phase. We note that, for any type of

equatorial waves, there is a precise identity between the meridional profile of zonal energy flux on the right hand side of (3.8a) and the quantity $(\partial\omega/\partial k)(\overline{u^2+v^2+\Phi_z^2/N^2})/2$, which is illustrated in JAS2021. The definition of φ in (3.8b) makes use of a Fourier expansion. In a depth-dependent form, (3.8b) can be reformulated such that the parameters k, m and ω are absent, which yields an inversion equation for PV to read

$$\left(\frac{\partial^2}{\partial x^2}+\frac{\partial^2}{\partial y^2}\right)\varphi+\frac{\partial}{\partial z}\left[\left(\frac{1}{N^2}\right)\frac{\partial}{\partial z}\left(f^2\varphi+3\frac{\partial^2}{\partial t^2}\varphi\right)\right]=q, \tag{3.9a}$$

where q has been defined in (3.5). The three-dimensional components of wave energy flux are written in a vector form as,

$$\overline{\mathrm{U}\Phi}+\langle\langle\frac{\partial}{\partial y}\left(\frac{\overline{\Phi\varphi}}{2}+\frac{1}{\beta}\frac{\overline{\partial^2 u}}{\partial t^2}\varphi\right),-\frac{\partial}{\partial x}\left(\frac{\overline{\Phi\varphi}}{2}+\frac{1}{\beta}\frac{\overline{\partial^2 u}}{\partial t^2}\varphi\right),0\rangle\rangle, \tag{3.9b}$$

whose horizontal component is referred to as the level-0 (i.e. exact) expression for waves at all latitudes. The vertical component of (3.9b) represents rough approximation and exact expression for the vertical group velocity times equatorial and midlatitude wave energy, respectively. See JAS2021 for the details of (3.9a)–(3.9b).

AGC17 considered eliminating the term representing the second order time derivative from their exact inversion equation for PV. This corresponds to (3.9a) in the present study. Let φ^{app} be the solution of the approximated PV inversion equation to read,

$$\left(\frac{\partial^2}{\partial x^2}+\frac{\partial^2}{\partial y^2}\right)\varphi^{app}+\frac{\partial}{\partial z}\left(\frac{f^2}{N^2}\frac{\partial}{\partial z}\varphi^{app}\right)=q, \tag{3.10a}$$

which may be solved using the set of a Dirichlet boundary condition ($\varphi^{app}=0$) at coastlines and bottom topography and a Neumann boundary condition ($\partial\varphi^{app}/\partial z=0$) at the sea surface. What AGC17 have called the level-2 (i.e. approximate) expression for energy flux is extended here to a depth-dependent form as,

$$\overline{\mathrm{U}\Phi}+\langle\langle\frac{\partial}{\partial y}\left(\frac{\overline{\varphi^{app}\Phi}}{2}\right),-\frac{\partial}{\partial x}\left(\frac{\overline{\varphi^{app}\Phi}}{2}\right),0\rangle\rangle, \tag{3.10b}$$

which has been used in the overall model analyses of the present study.

Equation (3.10b) may be applied also to equatorial KWs for which $\overline{U\Phi}$ becomes identical to the product of group velocity and wave energy density. Namely, no term for additional rotational flux is present. A characteristic of KWs is $v = 0$, which yields $q = 0$ following (3.5). Since the right hand side of (3.10a) vanishes, the expression of energy flux for KWs given in (3.10b) reduces to $\overline{U\Phi}$. This result is consistent with the nature of gravity waves.

We consider the Helmholtz decomposition of the level-2 wave energy flux to read,

$$-\frac{\partial}{\partial y}R - \frac{\partial}{\partial x}D = \rho_0\overline{u\Phi} + \rho_0\frac{\partial}{\partial y}(\overline{\varphi^{app}\Phi}/2), \tag{3.11a}$$

$$+\frac{\partial}{\partial x}R - \frac{\partial}{\partial y}D = \rho_0\overline{v\Phi} - \rho_0\frac{\partial}{\partial x}(\overline{\varphi^{app}\Phi}/2), \tag{3.11b}$$

where the scalar quantities R corresponds to the rotational component of energy flux and is referred to as energy-flux streamfunction. The quantity D in (3.11a)–(3.11b) is associated with the divergent components of energy flux and is referred to as energy-flux potential. The energy-flux potential becomes positive in regions where winds supply wave energy. The energy-flux potential becomes negative in regions where wave energy is dissipated. As shown by LA20, the distribution of potential is smooth and nicely shows large-scale characteristics, in contrast to the distributions of the wind-input and dissipation terms that manifest small-scale and locally sign-indefinite signals. This is the reason why the present study recommends to use the distribution of the energy-flux potential, instead of its pre-inversion terms. We shall show the distribution of the energy-flux potential and streamfunction, as given by (3.11a)–(3.11b), in the IO later in the manuscript.

Wave energy equation (3.6a) should include wind-forcing and dissipation terms. These terms yield the energy-flux potential defined in (3.11a)–(3.11b) in a climatologically equilibrium state of wave energy. The depth-integral of the wind forcing term is written as

$$u(x,y,0,t)\tau^x + v(x,y,0,t)\tau^y = \sum_n \frac{\alpha^{(n)}}{\sqrt{h_{mix}H_{bottom}}}[u^{(n)}(x,y,t)\tau^x + v^{(n)}(x,y,t)\tau^y], \quad (3.12)$$

which is referred to as wind-input (see contours in Figs. 3.8a, b and color shading in Fig. 3.9).

3.3 Result and discussion

3.3.1 Simulated results

We first briefly outline some key features from the LOM experiment. The model reproduces the SC, which flows along the East African coast and is driven by large-scale seasonal monsoonal winds, and the Wyrtki (1973) jet (e.g., Nagura and McPhaden, 2010a), which represents an along-equator response to semi-annual westerly winds during the monsoon transition period (Fig. 3.2). To investigate how the monsoon circulation affects velocity variability, we have constructed the longitude-depth sections of zonal velocity along the equator (left panels in Fig. 3.3) and the latitude-depth sections of zonal velocity at 70°E (right panels in Fig. 3.3). Semiannual winds induce east-upward tilt in the phase line of zonal velocity (yellow line in Figs. 3.3a and 3.3e), which can explain the formation of the Wyrtki jet in the following monsoon transition period. A semi-annual variation of baroclinic flow is dominant below about 200 m depth along the equator in response to the surface-layer Wyrtki jets. An eastward undercurrent near 150 m depth along the equator in February (Fig. 3.3a), referred to as Equatorial Undercurrent, is generated by equatorial KWs and long RWs, as investigated by Chen *et al.* (2015a, 2019). Simulated zonal velocity along 70°E is trapped at the equator with a vertical phase propagation, which coincides with the latitude-depth plots of climatological zonal currents along 80°E using ocean reanalysis data in Huang *et al.* (2018b). They pointed out that vertically propagating RWs generated by the reflection of wind-forced KWs at the eastern boundary of IO are responsible for the vertical phase propagation of mid-depth zonal currents on the basis of mooring and reanalysis data and this conclusion was

further confirmed by Zanowski and Johnson (2019) using velocity and isotherm displacement obtained from Argo floats.

We compare the seasonal anomalies of current and wind stress derived from OFES (Figs. 3.5a, b) and our climatological model experiments (Figs. 3.5c, d). The Hovmöller longitude-time diagrams along the equator at the sea surface indicate that the eastward-propagating KW signals are less pronounced in surface zonal velocity and more pronounced in geopotential anomaly (Figs. 3.5a, c, e). Semiannual winds cause velocity reversals four times per year. This is consistent with Yu and McPhaden (1999), Ding *et al.* (2009) and Nagura and McPhaden (2010a, 2010b), who pointed out that variability in surface zonal velocity along the equator is dominated by RWs, and that in SSH by equatorial KWs. Geopotential anomalies are positive near the surface during boreal spring and fall, which are associated with wind-forced downwelling KWs. Both the horizontal section at the surface (Figs. 3.5a, c) and the vertical section in the upper 2000 m (Figs. 3.5b, d) of zonal velocity derived from OGCM (Figs. 3.5a, b) and simulated by LOM (Figs. 3.5c, d) show upward phase signals and reversals of zonal currents four times per year with a noticeable semiannual cycle. These results agree with Huang *et al.* (2018a) and Chen *et al.* (2020), who demonstrated that the semiannual cycle is the predominant feature of mid-depth zonal currents in the equatorial IO. Geopotential anomalies (colors in Fig. 3.5f) are also characterized by the semiannual cycle with an upward phase propagation, which is attributable to wind-generated upwelling (during the monsoon seasons) and downwelling (during the monsoon transition period) KWs. The propagation of waves has a deterministic role on the vertical profile of geopotential anomalies (Figure 3.1). The semiannual signals of geopotential anomalies are weaker than that of zonal velocity, which are attributed to the interaction between KWs and RWs in the central IO (Yuan and Han, 2006). The upward phase signals of both zonal velocity and geopotential anomaly shift gradually in depth, and

variability in the deeper layer leads to that in the upper layer. This is regarded as the indication of downward energy transfers by oceanic waves (McCreary, 1984; Miyama *et al.,* 2006; Pujiana and McPhaden, 2020).

3.3.2 Transfer routes of wave energy

This chapter presents results from the first oceanic application of the depth-dependent version of the AGC17 scheme. In the following, all results associated with the AGC17 scheme were obtained using this extended version. We use the pressure flux (hereafter PF) scheme, as given by $\rho_0\overline{U\Phi}$, for comparison with AGC17 scheme, which is identical to flux defined by Eq. (3.5b) except for ρ_0. While the PF scheme yields meridionally alternating energy flux vectors (Fig. 3.6a), the AGC17 scheme is able to show basin-wide cyclonic patterns, which represent the depth-integrated transfer routes of KW and RW energy (Fig. 3.6b). These waves are driven by wind energy input in the vicinity of the Maldives (from 60°E to 80°E), the Arabian Sea and the southern Bay of Bengal (SBoB), as shown by the positive values of energy-flux potential (indicated by the contours of Fig. 3.6b). Near the African coasts, energy-flux streamfunction derived from the AGC17 scheme (color shadings in Fig. 3.6b) reveals cyclonic circulation that is localized in nature, whereas on the east side of the basin, the cyclonic circulation develops on significantly larger spatial scales in each hemisphere, as identified by LA20.

In terms of model performance at the key depths of 550 m and 1100 m, the PF scheme fails to reveal important energy fluxes with distinct eastward KW signatures and similarly misses a series of westward signals associated with midlatitude RWs (Figs. 3.6c, e). In contrast, the AGC17 scheme is able to show the eastward transfer of wave energy along the equator associated with equatorial KWs and also the westward transfer of wave energy in off-equatorial regions associated with midlatitude RWs (Figs. 3.6d, f). Note that pressure variability along the equator represents KWs and zonal velocity variability along the equator

are caused by RWs (Yu and McPhaden, 1999; Ding *et al.,* 2009; Nagura and McPhaden, 2010a, 2010b). The AGC17 scheme is appropriate when tracking the group velocity of baroclinic waves at all latitudes, particularly as it incorporates a realistic smooth transitioning between the tropical and subtropical regions. The contours in Figs. 4d and 4f show the vertical component of energy flux. Note that downward energy propagation is large in magnitude in the SBoB, the south Arabian Sea and the region between the equator and 5°S in 55°–75°E. In particular, the downward transfer of wave energy reaches its greatest depth in SBoB, as is described below.

Along the latitude-depth plane at 70°E, the westward flux of RW energy is symmetrically distributed across the equator (color shading in Fig. 3.7a). The vertical flux of wave energy at 90°E (contours in Fig. 3.7b) reaches a deep level at around 3°–5°N, corresponding to the downward flux of RW energy in the SBoB (Figs. 3.6d, f). The characteristics of this downward flux[1] are investigated by comparing time-depth diagrams at 70°E and 90°E along 3°N (Figs. 3.7c, d). The zonal component of energy flux based on the AGC17 scheme shows negative peaks four times per year, which is more distinct at 90°E than at 70°E (color shadings in Figs. 3.7c and 3.7d). The vertical component of energy flux at 90°E (contours in Fig. 3.7d) also shows negative peaks four times per year that become deepest in November–December. These features can be generated by either wind forcing in the SBoB or by the reflection and diffraction of equatorial KWs as they encounter the eastern boundary, as will be discussed in the next paragraph. The time-depth diagrams of the energy

[1] The vertical energy flux at 103°E, 6°S shows a similar deepest reaching pattern in November-December (not shown), which indicates that the reflection and diffraction of equatorial KWs affects both Northern and Southern Hemispheres.

flux at 70°E and 90°E on the equator (Figs. 3.7e, f) show peaks of eastward energy flux when zonal velocity exhibits upward phase propagation (Fig. 3.5d).

The Hovmöller longitude-time plots at the equator (panels on the left in Fig. 3.8) and at 3°N (panels on the right) shows zonal energy flux derived from the AGC17 scheme (color shadings). Zonal energy flux along the equator shows four beams per year at both the surface and at 550 m depth, which suggests a group velocity consistent with the second baroclinic mode KWs (blue solid lines). In contrast, the westward transfers of wave energy at the equator and at 3°N indicate group velocities consistent with both reflected equatorial RWs and diffracted midlatitude RWs. The surface eastward flux along the equator, which is intense in both February and May, is associated with upwelling and downwelling KWs, respectively (Fig. 3.8a). Energy input rate by wind forcing (Fig. 3.9) is predominant along the African coast during the northeast monsoon and southwest monsoon than that of during boreal spring and fall. Monsoonal winds excite the upwelling KWs along the African coast and bring the divergence towards the equator. It is consistent with the remarkable energy input by wind forcing at the African coast during boreal winter and summer at the equator and 3°N at the surface. In contrast, the eastward flux at 550 m depth along the equator is intense in both May and August (Fig. 3.8c) and reaches 1100 m depth in November (Fig. 3.8e), as shown by the time-depth diagram of Fig. 3.7e.

The poleward diffraction of equatorial KWs at the eastern boundary of the IO, followed by the radiation of off-equatorial RWs four times per year, is clearer at 550 m depth (Fig. 3.8d) than at the surface (Fig. 3.8b). This is because energy fluxes at the surface are forced by winds (contours in Fig. 3.8a and 3.8b) and represent the superposition of forced and freely propagating waves. Energy input by winds is more significant at 3°N than at the equator, which may be confirmed by the distribution of energy flux potential (contours in Fig. 3.6b). Returning to the issue of the SBoB downward energy flux that peaks in

November–December, we note that energy input by winds peaks in February and June between 80–90°E (Fig. 3.8b). It is less likely that wind forcing is the primary factor to generate SBoB downward flux in November–December. We note that the SBoB downward flux is induced by the boundary diffraction of mid-depth equatorial KW beam which peaks in August (Fig. 3.8c). As explained in the previous paragraph, eastward energy fluxes along the equator at 550 m depth lag behind those at the surface by 3 months.

This is further investigated using snapshots of energy fluxes in the longitude-depth sections along the equator (Fig. 3.10, left) and along 3°N (Fig. 3.10, right). Zonal energy flux at the equator propagates eastward at depths between 300 m and 1000 m in August (colours in Fig. 3.10e). This eastward peak in the western basin is followed by the development of an eastward energy flux in the central basin at around 900 m depth in November (Fig. 3.10g). These results indicate that the southwest monsoon over the African coast directly causes the August maximum in eastward energy flux at 550 m depth in Fig. 3.8c. Southwesterly winds over the Arabian Sea drive a strong northward EACC along the continental coasts. The current crosses the equator and is accelerated by winds in July, while the divergence of the surface flow excites upwelling KWs along the equator. The eastward transfer of KW energy is amplified by the southwest monsoon and appears not only at the sea surface but also at mid-depth. The boundary-diffracted RWs associated with these equatorial KWs dominate the downward penetration of wave energy in the SBoB, with signals reaching the greatest depths in November–December. Contours in Fig. 3.10 show the vertical component of energy flux. At 3°N (right panels), energy flux is downward all the year and represents an intense westward energy flux associated with off-equatorial RWs around 75°–90°E. Both westward and downward energy fluxes reach greatest depths in November (Fig. 3.10h). The above results highlight propagation and reflection of oceanic waves and clearly determine their origins. Thus the depth-dependent version of the AGC17 scheme is able to reveal the

properties of waves at subsurface and provides a better understanding of the processes governing the transfer of wave energy.

3.4 Conclusions

In order to study the effect of annual and semi-annual wind forcing on wave propagations in mid-depth in the tropical IO, we have estimated wave energy flux using output from a linear model driven by climatological wind-forcing. We have compared the performance of the PF scheme to that of the depth-dependent version of the AGC17 scheme summarized herein. The PF scheme represents meridionally alternating signals through the basin at the surface and shows neither eastward KW energy flux along the equator nor the westward transfer of energy flux related to off-equatorial RWs. The AGC17 scheme provides a better treatment of energy flux of both equatorial KWs and RWs and smoothly links the tropical and subtropical regimes.

Eastward energy flux shows distinct semiannual variations along the equator at subsurface, peaking four times per year, which indicate that energy given by surface monsoonal winds reaches below the pycnocline. The eastward flux at the surface on the equator is intense in both February and May associated with upwelling and downwelling KWs forced by semiannual winds, respectively. Eastward flux at 550 m depth at the equator is intense in both May and August and reaches down to 1100 m depth in November. In off-equatorial regions, westward energy flux associated with RWs exhibits four clearly-defined peaks.

The SBoB is the region where wave energy penetrates deepest. This downward energy flux is clearest at around 3°–5°N, 90°E that we attributed to the downward flux of RW energy. The energy input due to wind forcing at 3°N peaks between 80–90°E in February and June and cannot account for downward energy flux in November–December. An alternative explanation is that the boundary diffraction of mid-depth equatorial KWs is

responsible for the downward penetration of energy in the SBoB. The AGC17 scheme has shown that eastward energy flux at 550 m depth at the equator peaks in August, which induces boundary-diffracted RWs at this depth at 3°N in November–December. The peak in August may in part be due to the maximum of eastward energy flux in May at the surface on the equator. The maximum mid-depth eastward flux lags behind that of the surface eastward flux by 3 months, suggesting a downward propagation of wave energy.

A further important contribution is made by winds of the southwest monsoon in the Arabian Sea, which generates the divergence of energy at the surface near the equator along the African coastline and excites upwelling equatorial KWs in July. This process can have a direct impact on the formation of the peak in eastward energy flux associated with KWs in August below 300 m depth. These equatorial KW packets are diffracted poleward along the eastern boundary and become the source of off-equatorial RWs. The latter is responsible for the downward flux of wave energy which reaches greatest depth in November–December in the SBoB.

The advanced analytical and numerical techniques developed in this study can be extended to interannual timescales. Horii *et al.* (2008) found that the subsurface signals preceded the surface signals by 3 months during the initial stage of the positive IO dipole event (Saji *et al.,* 1999) in 2006, which hints a vertical propagation. The subsurface upwelling phase of wind-forced KWs potentially affects the development of the IO dipole by altering sea surface temperature (Chen *et al.,* 2016). The propagation and reflection process of these wave energy is also responsible for the significant intraseasonal oscillation in the equatorial eastern IO (Chen *et al.,* 2015b) and within the Bay of Bengal (Chen *et al.,* 2018). Future work in this direction will enhance our knowledge of the highly influential interactions and exchanges between the tropical and extratropical regions (particularly during

active phases of the IO dipole) and will therefore contribute to a better understanding of climate variation.

Table 3.1 List of experiment parameters. The basin-mode period is defined as $4L/c^{(n)}$ where L= 6110 km is the zonal distance of the Indian Ocean at the equator (from 45°E–100°E). The wind-coupling thickness is defined as $\sqrt{H_{mix}H_{bottom}}/\alpha^{(n)}$, where H_{mix} =35 m and H_{bottom} =5500 m.

baroclinic mode	1st	2nd	3rd	4th	5th	6th
gravity wave speed (m/s)	2.63	1.57	0.956	0.706	0.557	0.467
equatorial deformation radius (km)	339	262	205	176	156	143
equatorial inertial period (day)	9.4	12.1	15.6	18.1	20.4	22.3
basin-mode period (year)	0.29	0.49	0.81	1.1	1.39	1.66
$\alpha^{(n)}$ (non-dimensional)	0.39	0.41	0.27	0.29	0.23	0.22
wind-coupling thickness (m)	1123	1062	1644	1505	1933	1955

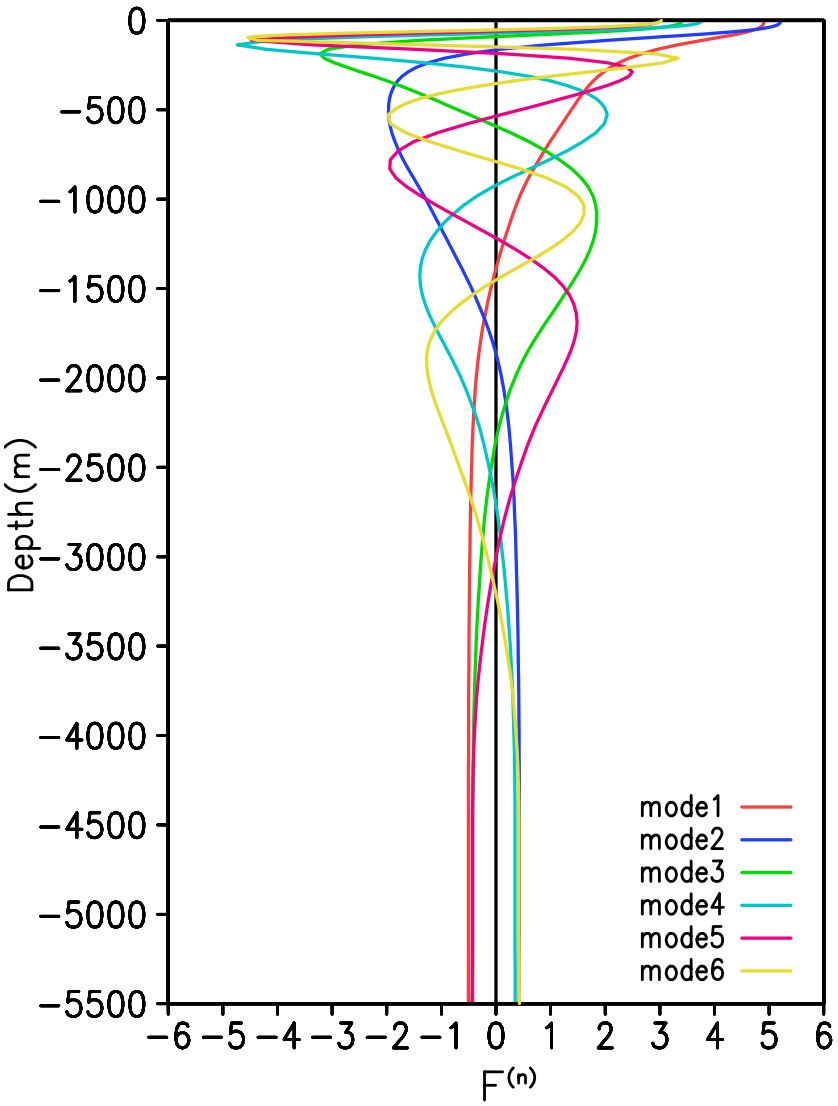

Figure 3.1 The vertical profiles of eigenfunctions $F^{(n)}$ associated with fundamental six baroclinic modes in the tropical Indian Ocean, calculated by solving the Sturm-Liouville problem.

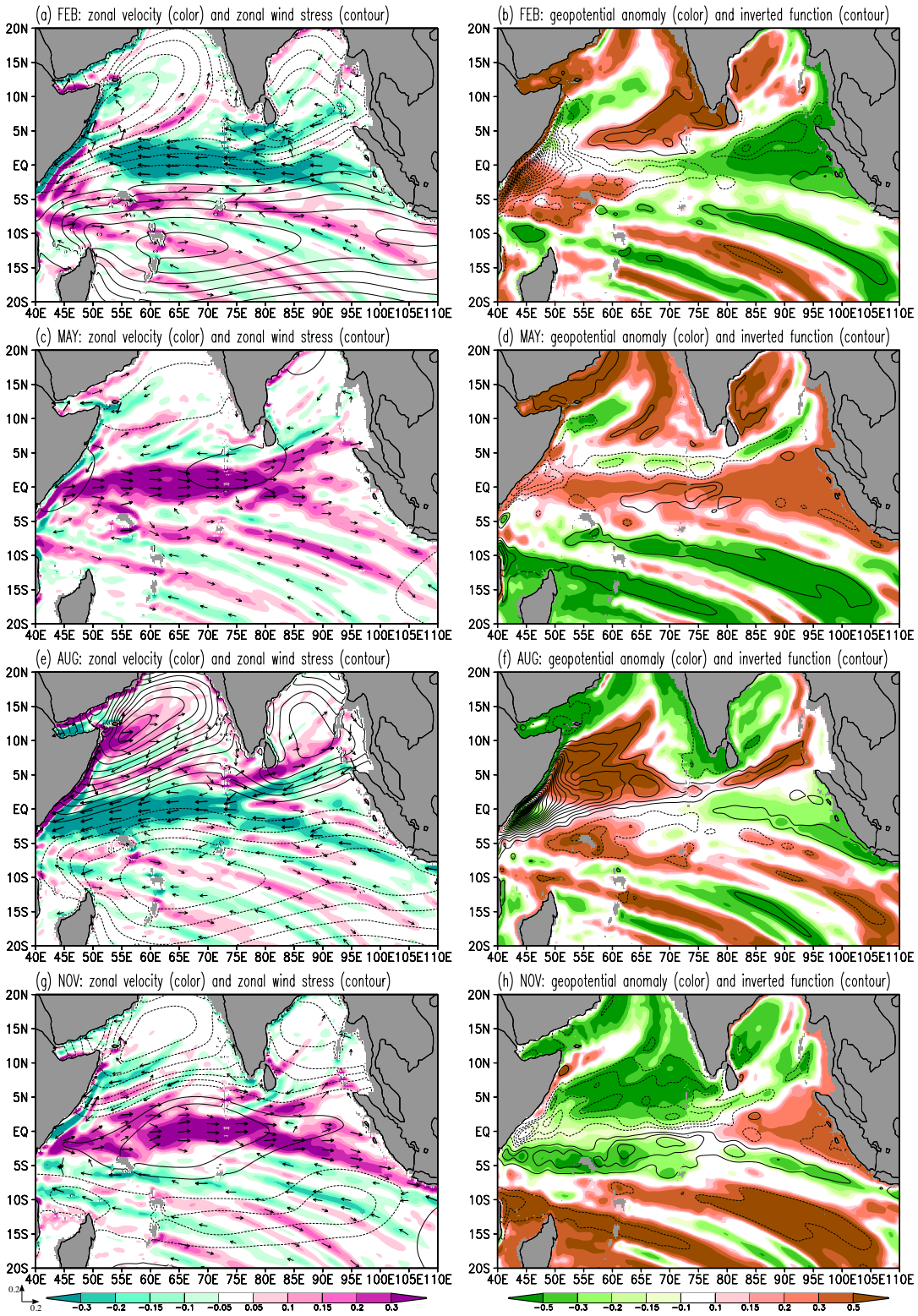

Figure 3.2 Left panels: the zonal component of simulated velocity at the sea surface (color shading with a unit of m/s), the zonal component of wind stress in the model (solid and dotted contours for eastward and westward anomalies, respectively, with an interval of 0.02 N/m^2), and the velocity vector (arrows in units of m/s) in the middle of (a) February, (c)

May, (e) August, and (g) November from "Year 20" of our climatological model experiments. When under 0.2 m/s, the magnitude of simulated velocity vectors in left panels is indicated either by arrow length or, for greater values, by heavy arrows of uniform length. Right panels (b, d, f, and h): same as left panels except for simulated sea surface geopotential anomaly (color shading with a unit of m^2/s^2) and PV-inverted function at the sea surface (solid and dotted contours represent positive and negative values, respectively, with an interval of 20,000 m^2/s). The PV-inverted function may be interpreted as geostrophic streamfunction in off-equatorial regions. The sea surface quantities have been reconstructed from the model results of fundamental six baroclinic modes.

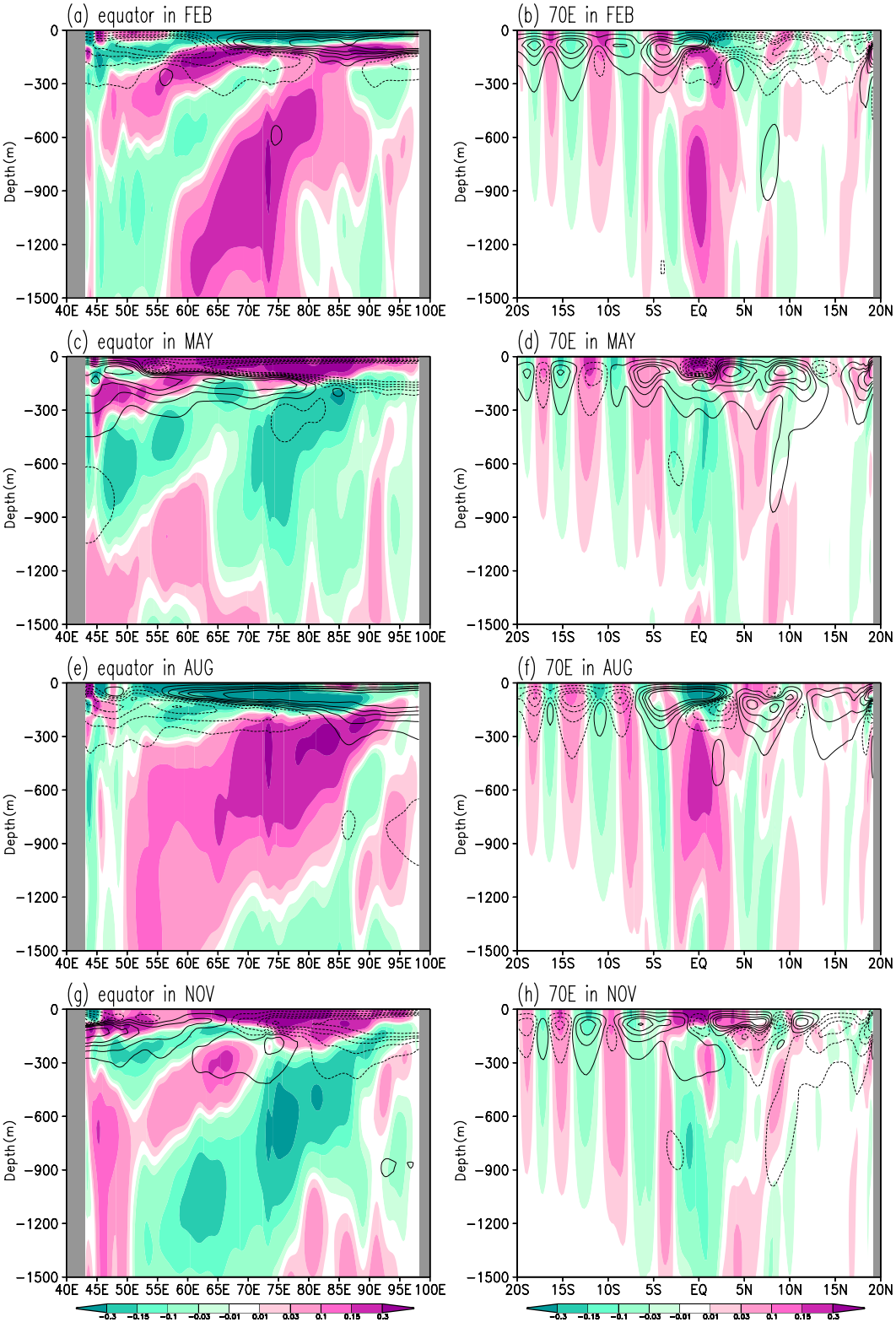

Figure 3.3 The zonal component of simulated velocity (color shading with a unit of m/s) and the vertical component of simulated velocity (solid- and dotted-contours indicate positive and negative values, respectively, at magnitude levels of 0.1, 0.4, 0.8, 1.2, 2 $\times 10^{-10}$ m/s) shown by

snapshots in the middle of (a, b) February, (c, d) May, (e, f) August, and (g, h) November from “Year 20” of our climatological model experiments. Zonal-vertical section at the equator (left panels) and meridional-vertical section at 70°E (right panels).

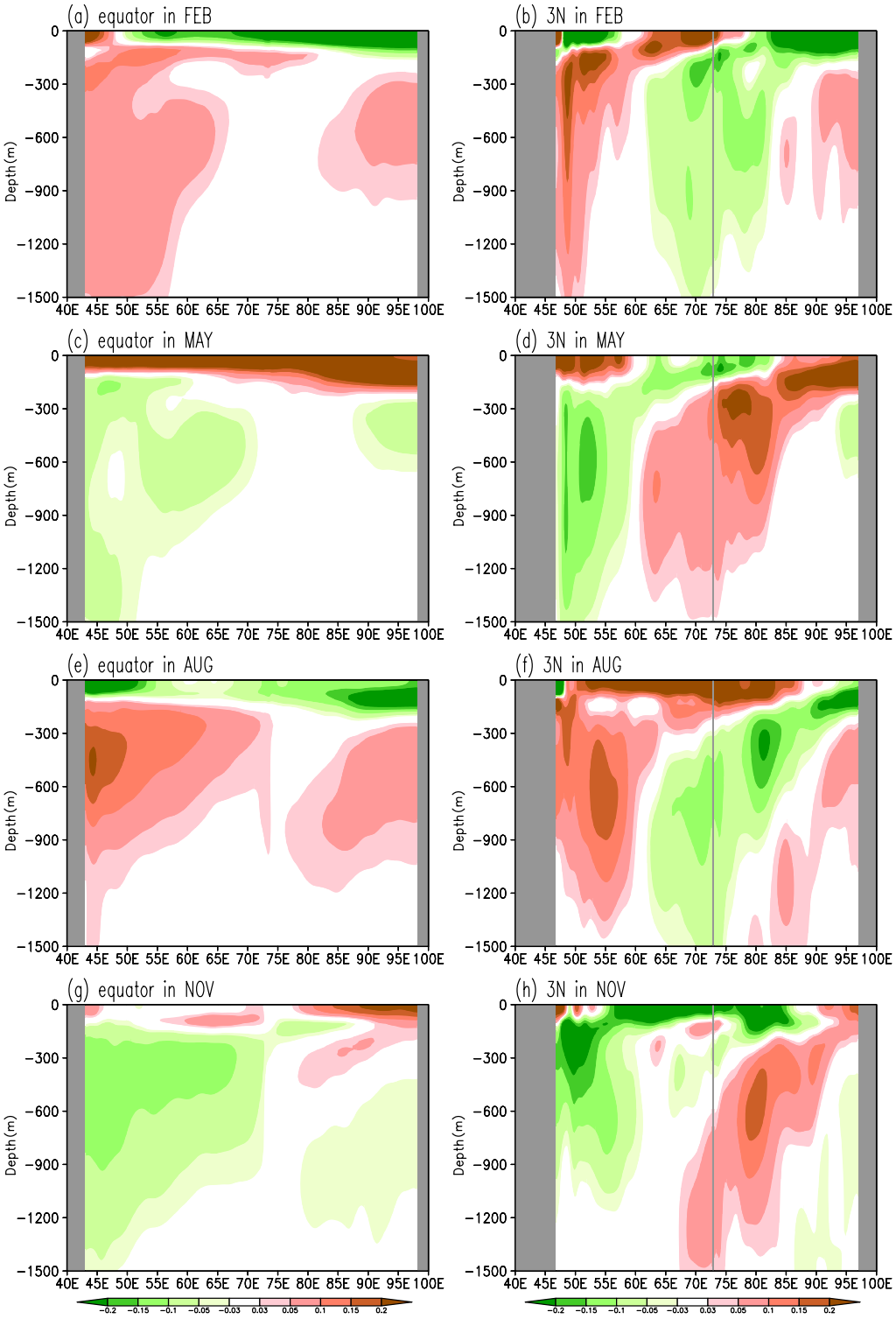

Figure 3.4 Simulated geopotential anomaly (color shading with a unit of m^2/s^2) in zonal-vertical sections at the equator (left) and at 3°N (right) from "Year 20" of our climatological model experiments: (a, b) mid-February, (c, d) mid-May, (e, f) mid-August, and (g, h) mid-November.

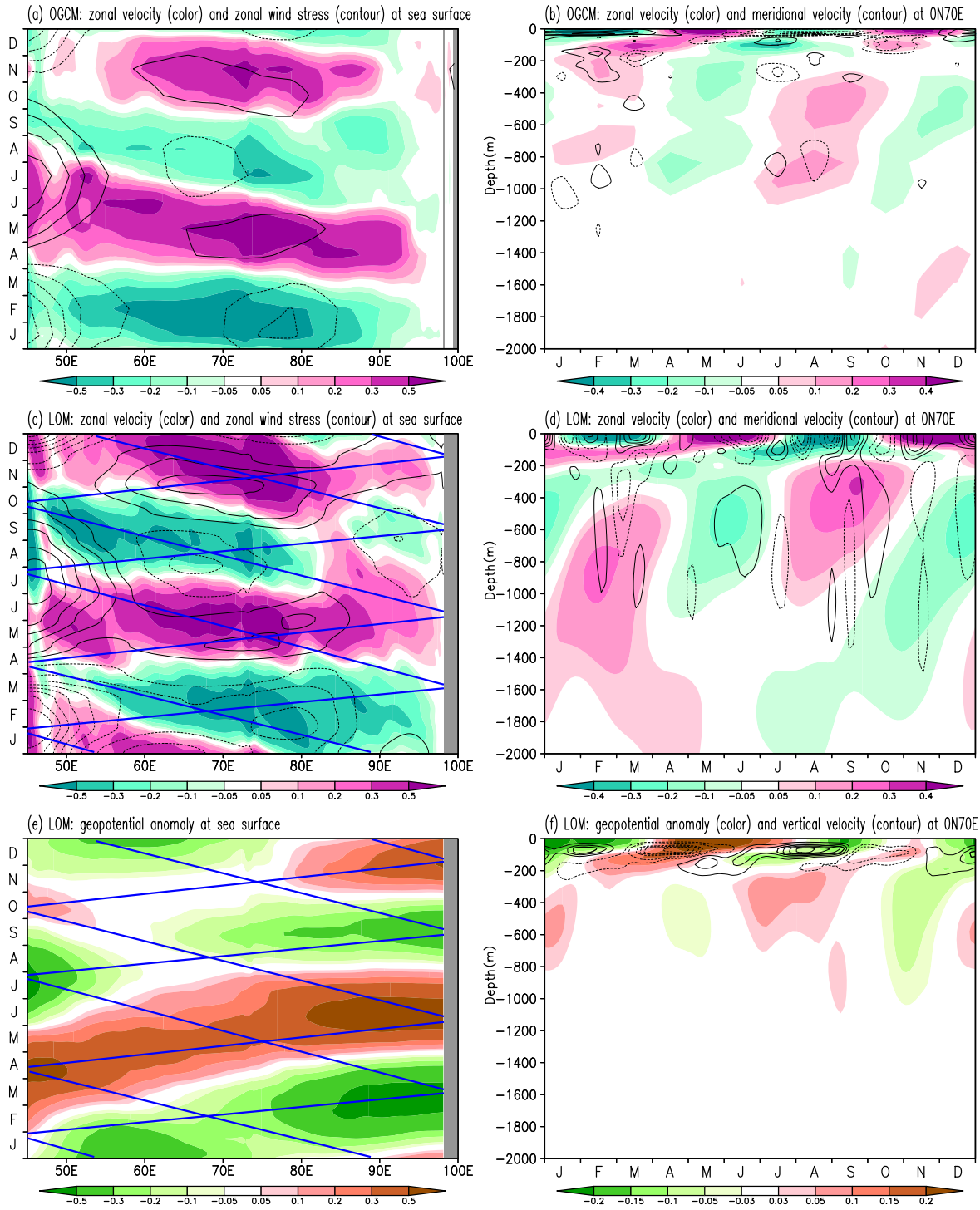

Figure 3.5 Hovmöller zonal-time diagrams at the sea surface of the equator (left panels) and depth-time diagrams at 70°E of the equator (right panels) from OGCM OFES (a, b) and "Year 20" of our climatological model experiments (c–f), respectively. Color shading in the panels (a-d) shows the output of zonal component of velocity based on OGCM (a, b) and LOM (c, d) with a unit of m/s. Color shading in the panels (e–f) shows simulated

geopotential anomaly with a unit of m^2/s^2. Panel (a, c) includes the zonal component of wind stress (solid- and dotted-contours for positive and negative values, respectively, with an interval of 0.1 N/m^2) from OGCM and LOM, respectively. Panel (b, d) includes the meridional component of velocity based on OGCM and LOM (solid- and dotted-line contours for positive and negative values, respectively, with an interval of 0.02 m/s). Panels (f) includes the vertical component of simulated velocity (solid- and dotted-contours for positive and negative values, respectively, with an interval of 0.05 m/s). Solid blue lines in the panels (c, e) indicate the theoretical phase speeds of both KWs and equatorial long RWs in the second baroclinic mode.

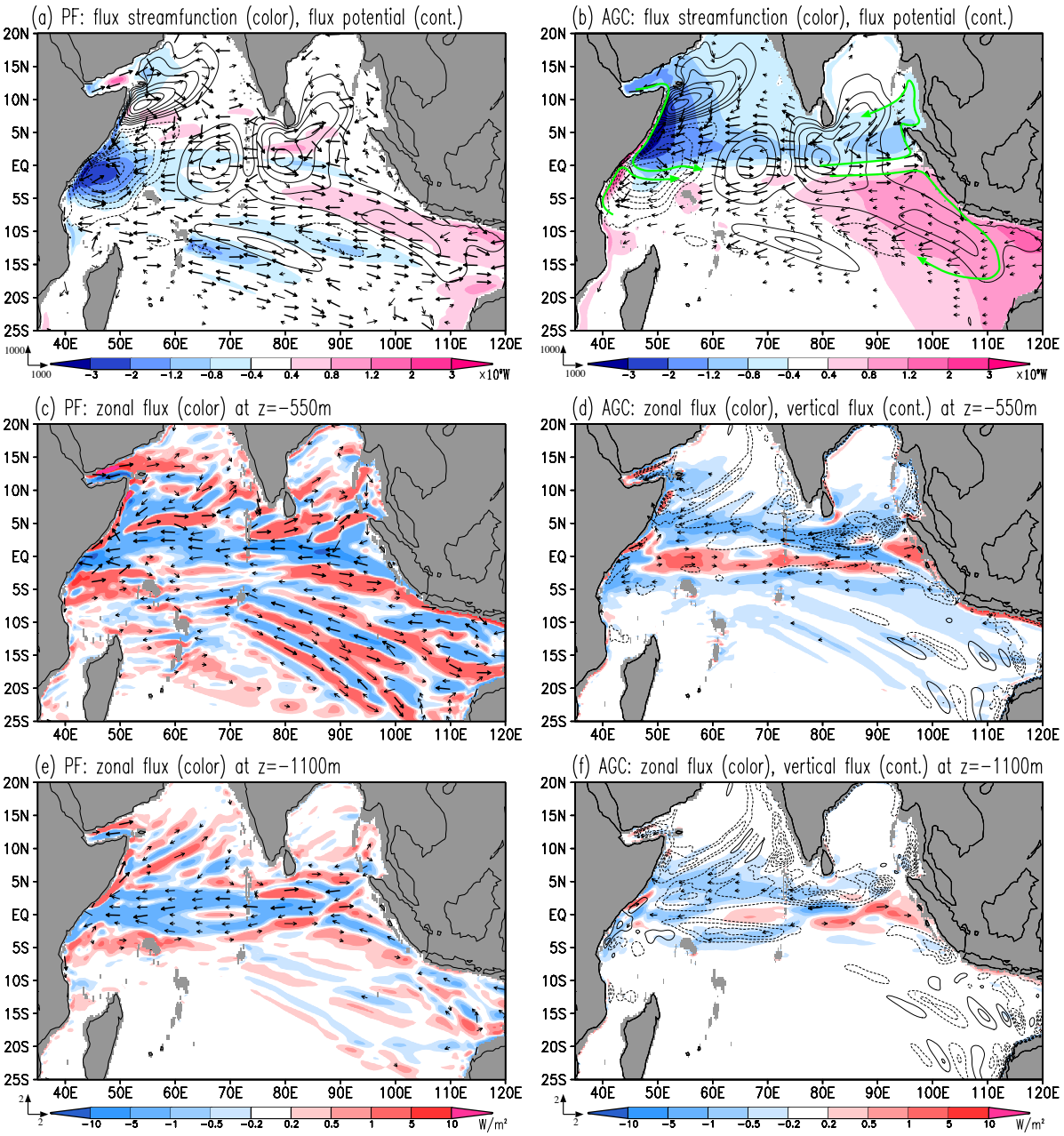

Figure 3.6 (a, b) Depth-integrated energy-flux streamfunctions (color shaded in units of 10^9 W=GW), depth-integrated energy-flux potentials (solid contours for positive values and dotted-contours for negative values; contour interval = 0.05 GW), and depth-integrated energy-flux vectors (arrows in units of W/m). (c, d) The zonal component of the energy-flux (color shaded in units of W/m^2) and the energy-flux vector (arrows in units of W/m^2) at 550 m depth. (e, f) Same as (c, d) except that depth is now 1100 m. All quantities represent annual mean values taken from "Year 20" of the model experiments, and estimated by the

pressure-flux scheme (left panels) and the depth-dependent version of the Aiki, Greatbatch, and Claus Level-2 scheme (right panels). Panel (b) includes two groups of cyclonic circulations of wave energy shown by green arrows that are demonstrated in LA20. Panels (d) and (f) include the vertical component of the energy flux, shown by contours (solid for positive and dotted for negative values) at intervals of 3×10^{-10} W/m^2 at 550 m depth and 0.5×10^{-10} W/m^2 at 1100 m depth. When under 1000 W/m, the magnitude of the depth-integrated energy-flux vectors in (a, b) is indicated either by arrow length or, for greater values, by heavy arrows of uniform length. Arrows in the series (c), (d), (e) and (f) are displayed in a similar fashion to (a) and (b), with the magnitude of the energy flux indicated either by arrow length (when under 2 W/m^2) or by heavy arrows of uniform length for greater values.

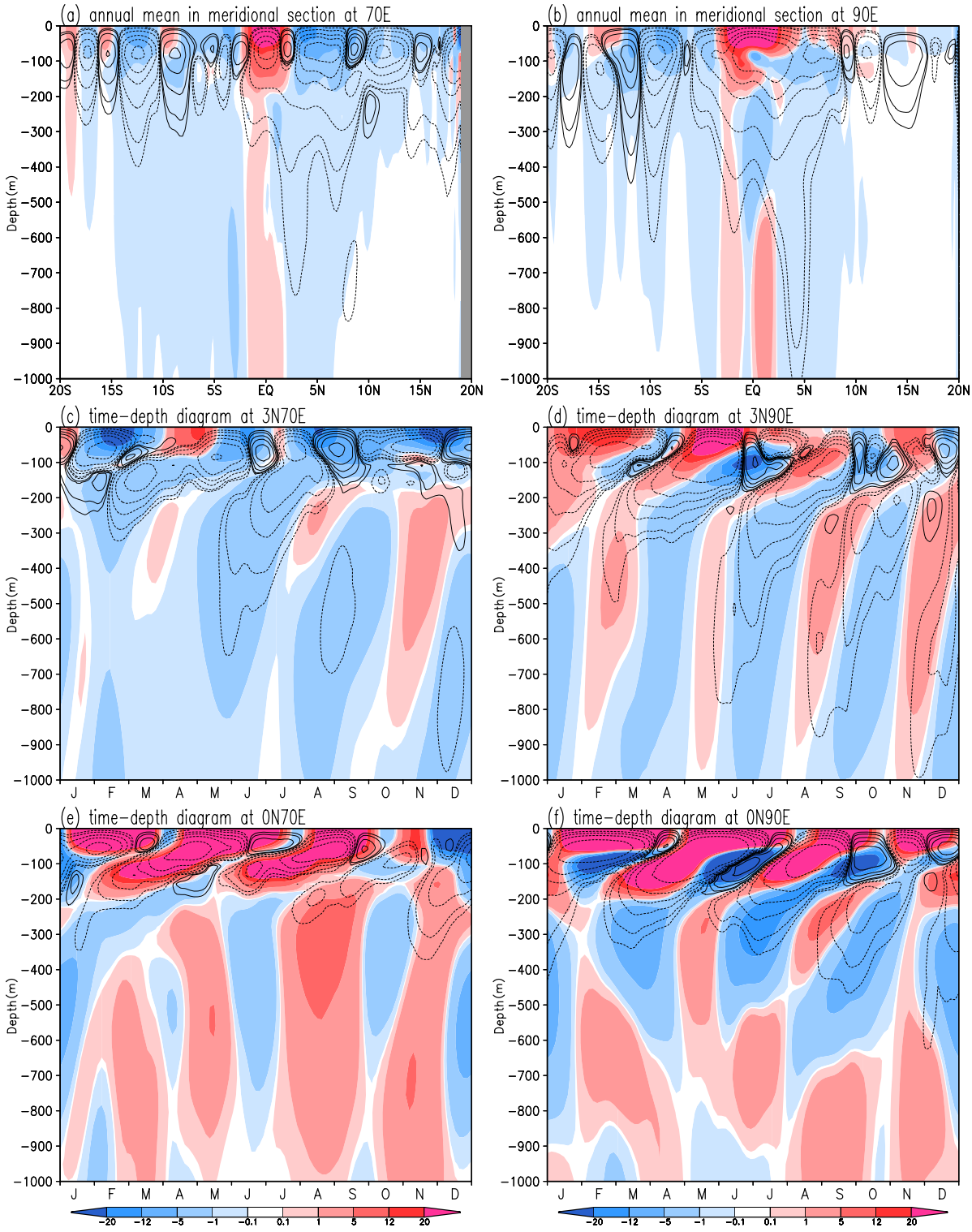

Figure 3.7 The zonal component of the energy flux (color shaded in units of W/m^2) and the vertical component of the energy flux (solid contours for positive values and dotted-contours for negative values) at magnitude levels of 1, 2, 5, 10, 20, 50 $\times 10^{-8}$ W/m^2) as estimated from the depth-dependent version of the Aiki, Greatbatch, and Claus Level-2

scheme, as given by (3.10b). Annual means in the meridional-vertical sections are shown in (a) at 70°E and (b) at 90°E. Hovmöller time-depth diagrams at 3°N for (c) 70°E and (d) 90°E and on the equator for (e) 70°E and (f) 90°E. All quantities are derived from “Year 20” of the climatological model experiments associated with first six fundamental baroclinic modes.

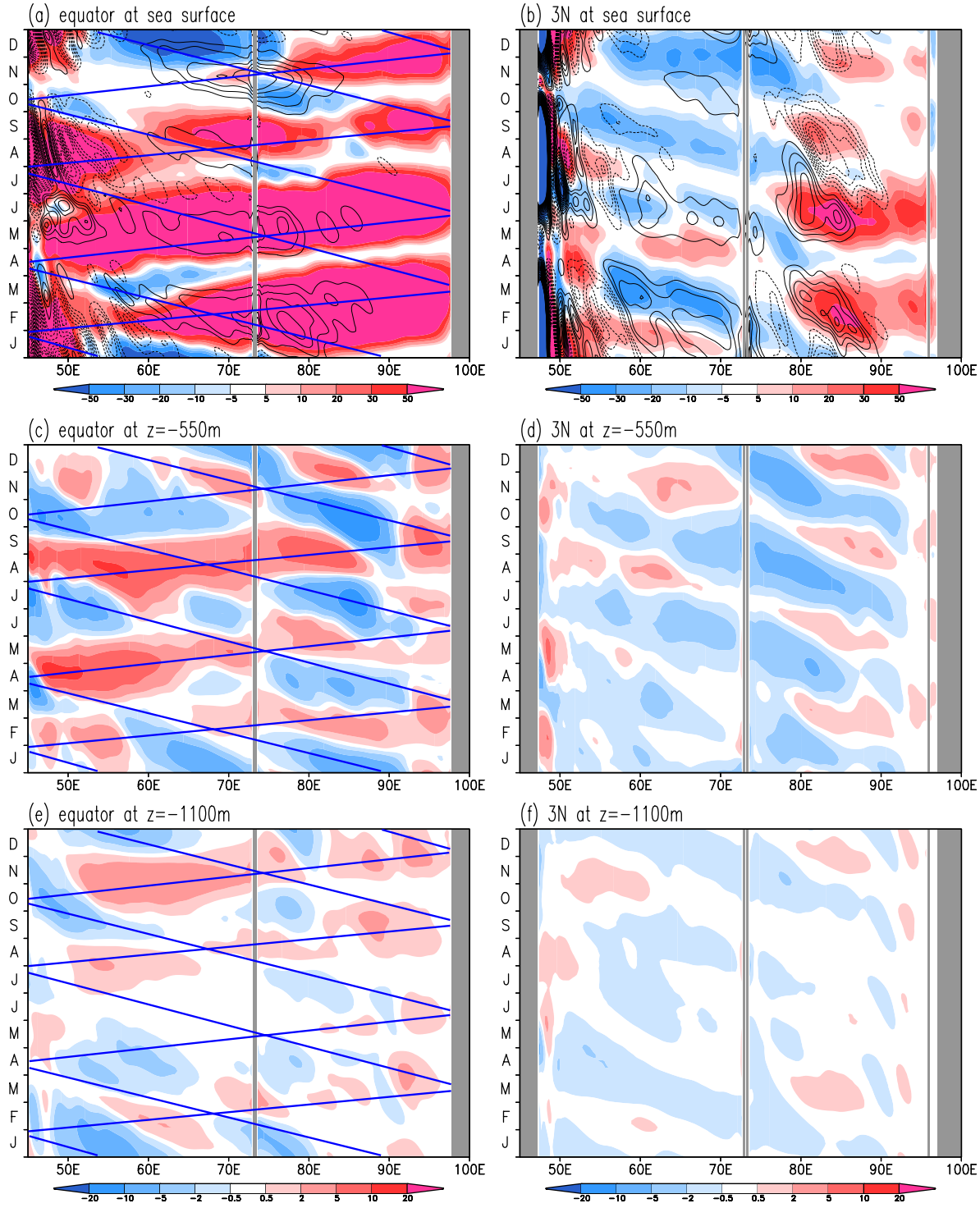

Figure 3.8 Hovmöller zonal-time diagrams for the zonal component of energy flux (color shaded in units of W/m^2) at (a, b) sea surface, (c, d) 550 m depth, and (e, f) 1100 m depth. Left panels show the equatorial behavior while right panels are for 3°N. Energy flux has been estimated using the depth-dependent version of the Aiki, Greatbatch, and Claus Level-2 scheme, as given by (3.10b). Panels (a, b) include wind-forced wave energy input (solid

contours for positive values, dotted contours for negative values; contour interval = 0.002 W/m^2) following (3.12). All quantities are from "Year 20" of the model experiments associated with first six fundamental baroclinic modes. In the left-hand panels, theoretical phase speeds calculated for both KWs and equatorial long RWs are shown as solid blue lines.

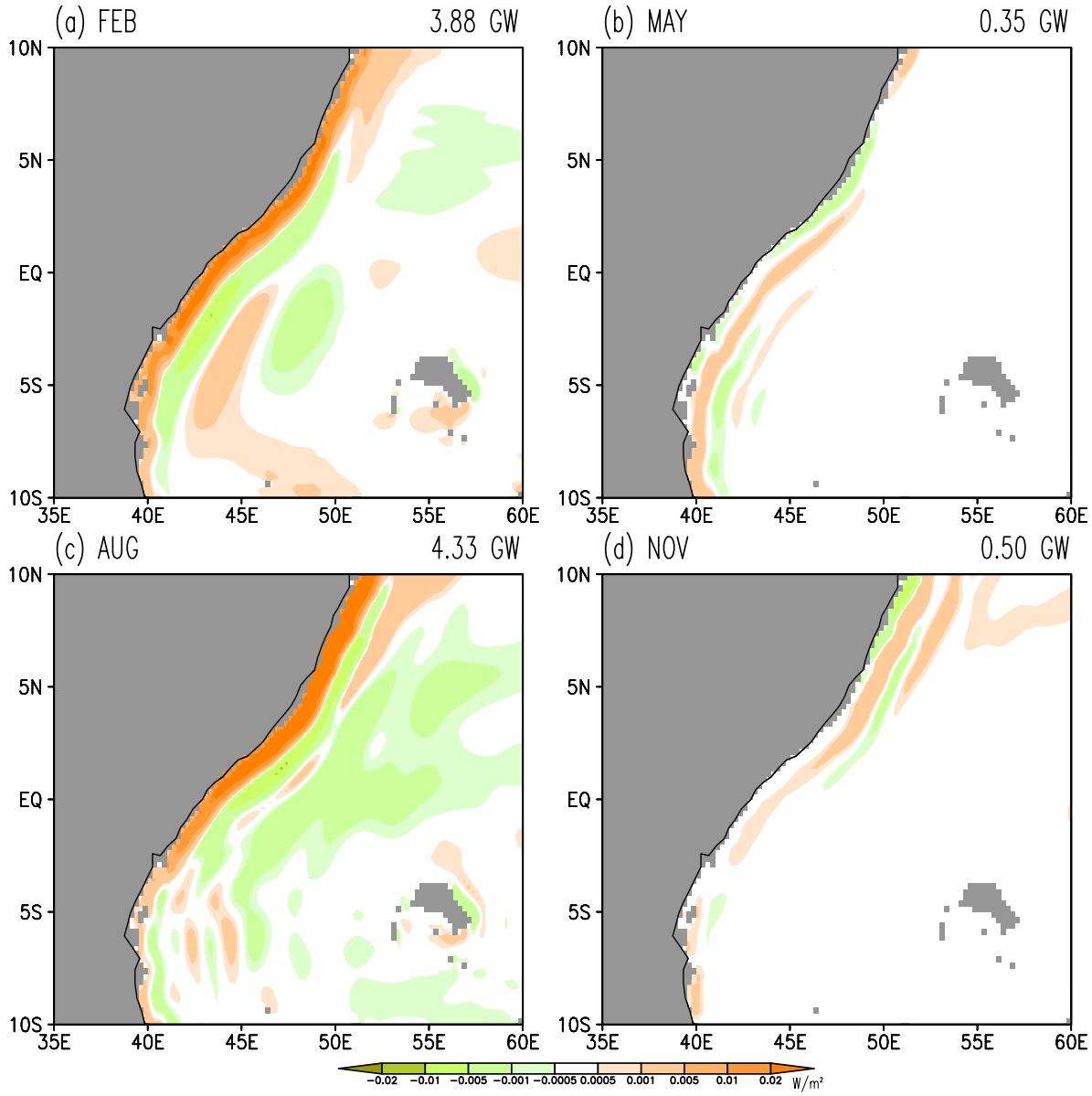

Figure 3.9 Energy input rate by wind forcing (W/m^2) near the African coast from "Year 20" of our climatological model experiments associated with sum of six baroclinic modes: (a) mid-February, (b) mid-May, (c) mid-August, and (d) mid-November. Spatially integrated values (35°E–60°E, 10°S–10°N) of the wind input rate are shown in the title (10^9 W = GW).

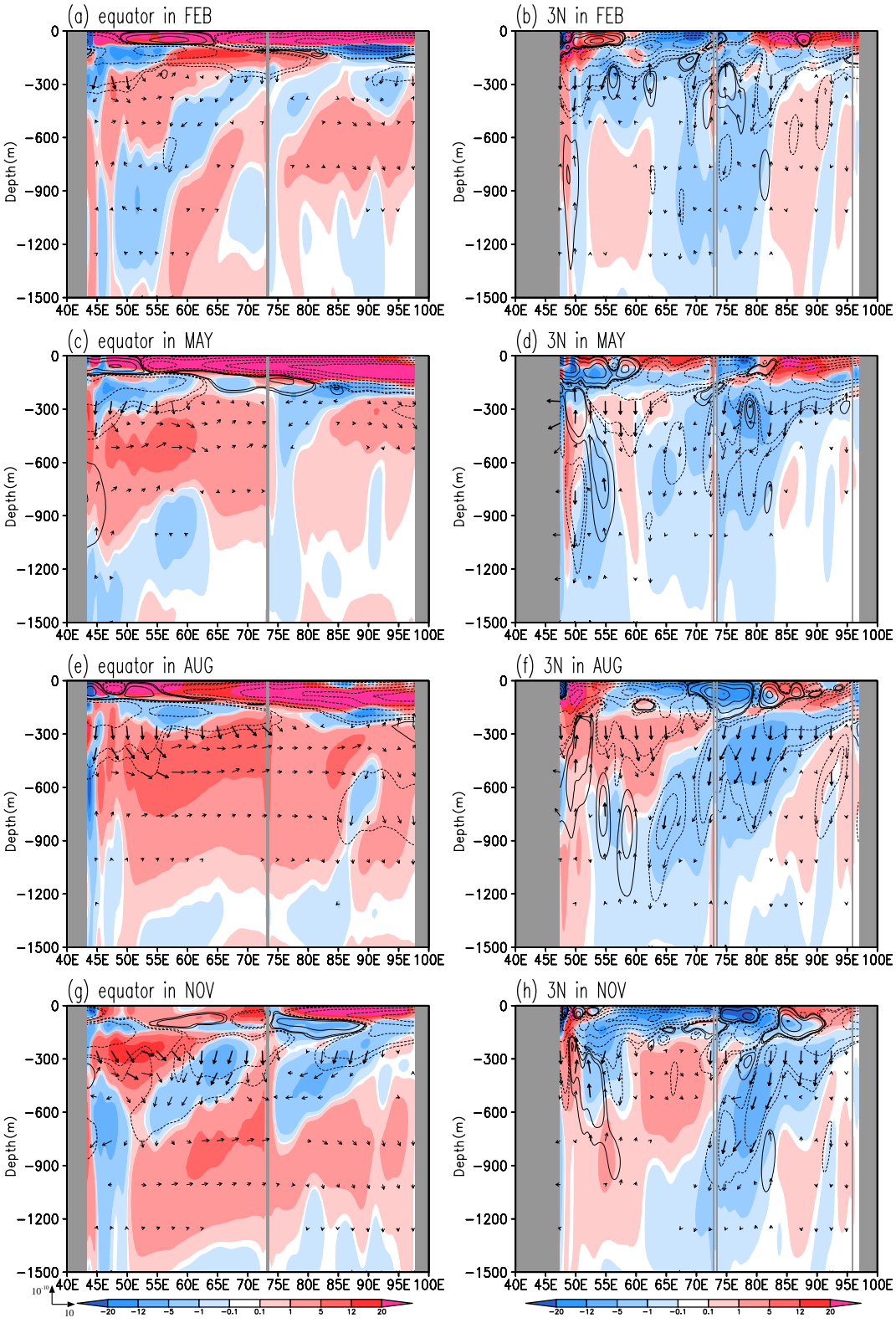

Figure 3.10 Zonal-vertical sections at the equator (left) and at 3°N (right) from "Year 20" of our climatological model experiments: (a, b) mid-February, (c, d) mid-May, (e, f) mid-August, and (g, h) mid-November. The zonal component of the energy flux (color shaded in

units of W/m^2), the vertical component of the energy flux (solid contours for positive values, dotted contours for negative values; contour magnitudes = 0.05, 0.1, 0.5, 2, 5, 10 $\times 10^{-8}$ W/m^2) and the energy-flux vector (arrows in units of W/m^2) estimated from the depth-dependent version of the Aiki, Greatbatch, and Claus Level-2 scheme, as given by (3.10b). When under 10 W/m^2, the magnitude of energy flux is indicated either by arrow length or, for greater values, by heavy arrows of uniform length.

Chapter 4

The 1994 positive Indian Ocean Dipole event as investigated by the transfer routes of oceanic wave energy

4.1 Introduction

The IOD is an important factor for explaining interannual variability of sea surface temperature (SST) in the tropical IO (Saji *et al.,* 1999; Webster *et al.,* 1999). The most dominant interannual variation in the IO is one originating from the ENSO in the Pacific Ocean as manifested by empirical orthogonal function (EOF) analyses of SST anomalies in previous studies. The IOD appears as the second EOF mode representing the zonal dipole structure of SST anomalies with opposite loading on the western and southeastern parts of the IO. The positive phase of IOD is associated with significant upwelling in the large parts of the southeastern basin and downwelling near the western basin. The IOD acts as a major driver for modulating the climate of countries surrounding the IO. For example, the East African regions suffered severe flood in 1994 (Behera *et al.,* 1999), in 1997 (Webster *et al.,* 1999) owing to these two positive IOD events. In Guan and Yamagata (2003), they mentioned that the East Asian countries experienced abnormal hot summer in response to the 1994 positive IOD. In 2010–2011, two severe floods occurred in Australia that are attributed to the 2010–2011 negative IOD event (Brigadier *et al.,* 2016). Another extreme negative IOD event in 2016 contributed to the abnormal precipitation with below average rainfall in the East African and above average rainfall over the eastern IO (Lu *et al.,* 2018). Recently, one of the strongest IOD events in records occurred in 2019. During 2019, a severe drought and catastrophic bushfire occurred in Australia. This extreme climate event is attributed to the two-year consecutive positive IOD and El Niño occurrence (Wang and Cai, 2020).

The IOD is an inherent air-sea coupled mode in the tropical IO, not a part of ENSO (Vinayachandran *et al.,* 1999; Saji and Yamagata, 2003; Ashok *et al.,* 2003; Hong *et al.,* 2008). During the 1994 pure positive IOD event, the southeastern tropical IO experienced the unusual atmospheric and oceanic conditions with cold SST and strong southeasterly surface winds (Behera *et al.,* 1999). Halkides and Lee (2009) and Tanizaki *et al.* (2017) examined the development of cooling SST in the southeastern tropical IO through mixed layer heat budget analyses in 1994. Vinayachandran *et al.* (1999) pointed out that these anomalous easterly winds in 1994 contributed to the weak Wyrtki (1973) jet during boreal spring. The 1994 positive IOD event initiated in May which is earlier than another positive IOD event owing to the intraseasonal disturbances in 1994 (Rao and Yamagata, 2004).

The IOD is associated with thermocline depth anomalies that propagate as large-scale waves. Previous studies have adopted various methods to investigate the characteristics of equatorial KWs and RWs in the IO at interannual timescales. The dynamics of KWs and RWs has a crucial impact on the development and termination of IOD which in turn alters SST (Yamagata *et al.,* 2004; McPhaden and Nagura, 2014; Delman *et al.,* 2016). During the positive phase of IOD, easterly wind anomalies excite an upwelling equatorial KWs propagating eastward, leading to the upwelling off Java and Sumatra coasts (Vinayachandran *et al.,* 2001; Delman *et al.,* 2016; Chen *et al.,* 2016). Huang and Kinter (2002) analyzed heat content to demonstrate the western boundary reflection from RWs to KWs is a pivot in relaxing the SST anomaly in the eastern basin. Rao *et al.* (2002) demonstrated that the subsurface dipole corresponding to the IOD may help reverse the surface dipole through westward propagating RWs. Yuan and Liu (2008) found the western boundary reflection from RWs to KWs provides important negative feedback to the evolution of upwelling currents off the Java coast during the IOD events by analyzing sea level anomaly. Nagura and McPhaden (2010) examined interannual variability in the equatorial IO based on the zonal

velocity and sea surface height (SSH). They demonstrated that the velocity anomalies reverse before the wind anomalies reverse during the decay of IOD events owing to reflected RWs from the eastern boundary. Yan *et al.* (2012) pointed out that the thermocline variation forced by eastward propagation of KWs is crucially important for the development and decay of IOD events. Another important issue is the influence of ENSO during IOD-ENSO concurrent years. It has been demonstrated that El Niño forcing is necessary to strengthen and maintain the westward propagating off-equatorial RWs in the southern tropical IO even after the IOD has demised (Chakravorty *et al.,* 2013, 2014). Du *et al.* (2020) illustrated that the downwelling RWs in the southern tropical IO have a decisive effect on the 2019 extreme positive IOD event. Based on the significance of wave dynamics, it is necessary to analyze the propagation of waves through the view of wave energy which may offer a better understanding of the development of IOD.

The prime objective of the present study is to provide a new perspective for the interannual variability in the tropical IO based on the transfer routes of wave energy using a new scheme of Aiki *et al.* (2017, hereafter AGC17). This scheme has been successfully applied to trace the transfer episodes of wave energy in the IO at intraseasonal timescales (Ogata and Aiki, 2019) and at seasonal timescales (Li and Aiki, 2020, hereafter LA20), in the Atlantic Ocean at annual timescales (Song and Aiki, 2020) and at intraseasonal timescales (Song and Aiki. 2021), and in the Pacific Ocean at interannual timescales (Toyoda *et al.,* 2021). This study represents the first application of the AGC17 scheme in the IO at interannual timescales and may be regarded as a counterpart of Toyoda *et al.* (2021).

The present manuscript is organized as follows. Section 4.2 provides the details of the model, data used, numerical experiments and diagnostic scheme used for the study. Section 4.3 highlights the 1994 pure positive IOD event to illustrate the general features of model output in the IO at interannual timescales. In section 4.4, we analyze the transfer episodes of

wave energy in 1994–1995 and examine the evolution of wave energy by comparing with 1990 as an IOD neutral year. Section 4.5 presents a summary of our major results.

4.2 Materials and Method

4.2.1 Linear Ocean Model

We have performed a set of 61-year hindcast experiments for interannual variability in the IO using a linear ocean model (LOM). The governing equations of the model are shown in (2.1a)-(2.1c). We have applied the same model to simulate the monsoonal variation of wave energy in the IO (LA20) and examine the vertical propagation of waves at seasonal timescales in the IO (Li *et al.,* 2021). The model is forced by monthly wind stress from 1958 to 2018 derived from the Japanese 55-year Reanalysis (JRA-55) 10 m wind velocity with the bulk formula of Large and Pond (1981). The model domain spans from 25ºS to 20ºN, and from 30ºE to 120ºE with realistic coastlines. The model coastlines are derived from 100-m isobath in the General Bathymetric Chart of the Oceans (GEBCO) dataset. The Indonesian Archipelago has been closed. No side friction has been applied at the coastal boundaries of the model domain. Eddy viscosity is as in LA20. The model yields three-dimensional output with a ¼ grid spacing in both zonal and meridional directions. The vertical profile of density in the tropical IO is averaged over 20ºS–20ºN and 40ºE–110ºE extended to 5500 m depth and computed from annual mean salinity and temperature in the World Ocean Atlas 2013. As done by LA20, we have assumed no motion near the ocean bottom and estimated the gravity wave speed of the *n*-th vertical mode $c^{(n)}$ following the bottom-pressure decoupling theory of Tailleux and McWilliams (2001). The vertical mode decomposition indicates gravity wave speeds of 2.99, 1.69, and 1.03 m/s for the first three baroclinic modes, respectively. The model output is separated into 6100 snapshots with an interval of 3.65 days over 61 years.

4.2.2. Diagnostic scheme for wave energy

In the present study, we use a newly proposed diagnostic scheme described by AGC17 to trace the transfer episodes of wave energy by analyzing the directionality of wave group velocity vectors. As compared to previous diagnostic schemes, such as pressure flux schemes (Cummins and Oey, 1997) and the Orlanski and Sheldon (1993) scheme, the AGC17 scheme has the advantage of smooth tropical and subtropical transition for all waves and at all latitudes (Ogata and Aiki, 2019; Song and Aiki, 2020; LA20; Toyoda *et al.,* 2021; Song and Aiki, 2021; Li *et al.,* 2021).

AGC17 have presented an approximated version of the energy flux, which has been referred to as level-2 expression to read,

$$\ll \overline{u^{(n)}p^{(n)}} + (\overline{p^{(n)}\varphi^{app}}/2)_y, \overline{v^{(n)}p^{(n)}} - (\overline{p^{(n)}\varphi^{app}}/2)_x \gg, \tag{4.1a}$$

$$\nabla^2\varphi^{app} - (f/c^{(n)})^2\varphi^{app} = q^{(n)}, \tag{4.1b}$$

where $\nabla^2 = \partial_{xx} + \partial_{yy}$. The quantity φ^{app} is the solution of potential vorticity inversion equation (4.1b).

4.3 Results and Discussion

4.3.1 simulated results

a. Comparison between reanalysis and simulated results

The dipole mode index (DMI) is defined as the difference in sea surface temperature anomalies between the western (10ºS–10ºN, 50ºE–70ºE) and southeastern (10ºS–0º, 90ºE–110ºE) parts of the tropical IO, which has turned out to be useful for identifying the occurrence of IOD (Saji *et al.,* 1999). We have validated simulated sea surface geopotential anomalies against 20°C isotherm depth anomalies in the European Centre for Medium-Range Weather Forecasts (ECMWF) ocean reanalysis (ORAS3). Figure 4.1a shows the time series of DMI between model output and reanalysis results during 1959–2009. The depth of 20°C

isotherm manifests the variability of thermocline. When the IOD is under the positive phase, the thermocline becomes anomalous shallow in the eastern IO corresponding to the upwelling near the Sumatra coast. In contrast, the thermocline deepens anomalously in the western IO corresponding to anomalous downwelling near the African coast. The simulated index (red line in Fig. 4.1a) is based on the model output of sea surface geopotential associated with the sum of three baroclinic modes in our hindcast experiments. Classification of IOD years in the present study is based on Saji *et al.* (1999). The IOD was under the positive phase during 1961, 1966, 1967, 1972, 1982, 1994, 1997–98, and 2006. Following the definition of ENSO events in Trenberth, (1997), the 1961, 1966, 1967, and 1994 positive IOD events develop independent of ENSO, which are referred to as the pure IOD events (yellow shaded columns in Fig. 4.1a). The 1972, 1982, 1997–98 and 2006 positive IOD events co-occur with strong El Niño in the Pacific (green shaded columns in Fig. 4.1a). We have calculated lead-lag correlation coefficients between model output and reanalysis results (Fig. 4.1b) and obtained the highest correlation coefficient of 0.825 at no lag in the period of 1959–2009 and particularly up to 0.95 during 1994 (figure not shown). While the positive lags signify that LOM leads ORAS3. These results suggest that our model has done reasonable work in simulating the interannual variability associated with the IOD.

b. General features of simulated results during 1994 positive IOD event

We have investigated the energy transfer episodes during the 1994 pure positive event. The results in the following sections are during the period 1994–1995. First we examine how good the model simulation is able to reproduce or differs from the previous understanding of the development process of IOD events. Figures 4.2 and 4.3 show a set of Hovmöller diagrams at the equator for the first three baroclinic modes during 1990 and 1994–95, respectively, the former of which represents a neutral year in terms of IOD. The magnitude of the second baroclinic mode is greater than that of the first and third baroclinic

modes in both periods (Tommy, 1993; Polito and Liu, 2003; Nagura and McPhaden, 2010; Iskandar *et al.,* 2014; Ogata and Aiki, 2019; LA20; Chen *et al.,* 2020). The result shows that during the neutral year of 1990, zonal velocity and geopotential anomaly are phase-locked to the seasonal cycle along the equator in the second baroclinic mode (Figs. 4.2c, d). The zonal velocity along the equator reverses direction four times per year (Fig. 4.2c). During boreal spring and fall, westerly winds induce eastward currents referred to as Wyrtki jet, while the northeast and southeast monsoon winds trigger the westward currents during boreal summer and winter. The geopotential anomaly shows positive signals (indicating thermocline deepening) during boreal spring and fall and negative signals (indicating thermocline shallowing) during boreal summer and winter (Fig. 4.2d). Along the equator, the westerly component of wind stress is dominant during boreal spring and fall, while the easterly component of wind stress appears during boreal summer and winter.

In contrast, during 1994 along the equator, anomalous easterly winds appear first by May and intensify in the following months then attain a peak in August–September (Fig. 4.3c). This feature along the equator weakens and terminates by March 1995. These easterly winds derived from southeastern IO are restricted to the central-eastern equatorial IO. During the fall of 1994, easterly winds along the equator induce westward currents, corresponding to the predominant energy input by wind forcing (negative contours in Fig. 4.4e). A slightly slower pulse of zonal currents appears in the western basin (November 1994–April 1995) as compared with that of normal months that are associated with westward propagating RWs. These easterly winds in the positive phase induce westward transport coincident with the negative signals off Sumatra during the positive IOD. These negative geopotential anomalies are associated with upwelling KWs and resulting anomalous thermocline shoaling (Fig. 4.3d).

Figures 4.4 and 4.5 show the time evolution of geopotential anomaly during 1990 and 1994, respectively. Geopotential anomaly in 1990 is characterized by seasonal cycle in the tropical IO. Upwelling signals appear during boreal winter and summer, while downwelling signals appear during boreal spring and fall in the central eastern equatorial IO. Wind stress vectors in February and August coincide with northeast and southwest monsoon winds, respectively. As compared to the neutral year, southeasterly winds initiate from May and dominate over the southeastern IO in May–October during 1994. These anomalously strong winds induce upwelling in the central-eastern tropical IO from June–December. The southeasterly winds become weak from November and terminate in December.

4.3.2 transfer routes of wave energy

We now trace the transfer routes of wave energy through the directionality of wave group velocity vectors using the AGC17 scheme to examine the interannual variability in the IO based on the results of our hindcast experiments. In the following paragraphs, the results of energy-flux vectors are based on the second baroclinic mode and the results of energy-flux streamfunction and energy-flux potential are based on the sum of the first three baroclinic modes.

a. 1994 positive IOD event

Figure 4.6 shows a set of Hovmöller diagrams along 3°N, equator, and 3°S for the second baroclinic mode during 1990 and 1994–95. During the neutral IOD year of 1990, the equatorial KWs appear four times per year, which is consistent with the life-cycle of wave energy determined by LA20. The westerly winds during boreal spring and fall at the central equator generate downwelling KWs that propagate eastward toward Sumatra coast. Upwelling KWs along the equator during boreal summer and winter are triggered by the southwest monsoon and northeast monsoon, respectively. The energy flux at both 3°N and 3°S during 1990 (Figs. 4.6a, c) is characterized by seasonal variation. During 1994, the

continuous easterly winds extending from the southeastern IO along the equator dominate from April 1994–March 1995 and induce upwelling KWs which propagate eastward, as manifested by the negative signals of geopotential anomaly (Fig. 4.3d) in the eastern basin of the equatorial IO. The absence of westerly winds at the central equator during the monsoon transition period (Fig. 4.3c) results in the absence of energy input by westerly wind at the central equator during boreal spring and fall (Fig. 4.6e). Considering the generation of wave energy, the absence of westerly winds at the central equator may account for the weak eastward signals of equatorial KWs at the central-eastern basin in April–May of 1994 (Vinayachandran *et al.,* 1999) and the absence of equatorial KWs at the central-eastern basin in October–November of 1994. The easterly winds were sustained until early 1995 along the equator. Meanwhile, upwelling KWs during January–March of 1995 are basically in response to these easterly winds along the equator instead of being forced by the northeast monsoon.

The traveling period of a packet of KWs propagating eastward and then back as boundary-reflected equatorial long RWs propagating westward across the equatorial IO (from 45ºE to 100ºE) is referred to as basin mode period (Jensen, 1993; Han *et al.,* 1999). It takes 0.26, 0.46, and 0.75 years for the first three baroclinic modes, respectively. Given that the basin mode period of the second baroclinic mode is about half a year and the theoretical phase speed of equatorial KWs is 3 times faster than that of equatorial long RWs. Equatorial KWs and long RWs take about 1.5 and 4.5 months, respectively, to cross the basin. During 1994, it seems that the traveling period for one round trip of KWs and RWs across the equatorial IO extends roughly to 8 months (August 1994–March 1995) in the second baroclinic mode (Fig. 4.4e). Since the eastward transfer of energy flux associated with the equatorial KWs takes 1.5 months (July–August in 1994) to cross the zonal extent of the equatorial IO as usual, the longer traveling period is attributed to the propagation of westward

energy flux. At the central-eastern basin along the equator, the phase speed of RWs is consistent with the theoretical phase speed of equatorial long RWs (green solid line in Fig. 4.6e, August–October in 1994). This set of westward energy flux is attributed to the reflected equatorial RWs at the eastern boundary. At the central-western basin, the group velocity of westward transfer of energy flux is slightly slower (pink line in Fig. 4.6e) than at the central-eastern basin. For the formation of this slower set of westward energy flux, we first considered the possibility that the anomalous easterly winds at the equator may be responsible for this slower westward transfer of energy flux. Zonal currents from September 1994 to March 1995 are accelerated by the easterly winds, indicating the predominant energy input by wind forcing (negative contour in Fig. 4.6e). This may generate and intensify the westward transfer of energy flux associated with RWs at the equator. The eastward transfer of energy flux associated with KWs forced by these easterly winds in February–March of 1995 has the same phase as the theoretical second baroclinic mode of KWs. Thus these easterly winds could not generate the different group velocities of westward energy flux associated with RWs at the equator. We have then examined whether the off-equatorial RWs from the southeastern basin are the possible factor for the formation of this slower set of westward energy flux or not. Based on the Hovmöller diagrams of energy flux along 3ºS, equator, and 3ºN during 1994–95 based on the AGC17 scheme (Figs. 4.6d–f), we note that the eastward signals related to KWs at the equator during July–August of 1994 are attributed to these abnormal easterly winds. As these KWs arrive at the eastern boundary, they are reflected and diffracted to equatorial and off-equatorial RWs, respectively. Energy flux at 3ºN is characterized by the seasonal cycle rather than interannual variation (Fig. 4.6d). The westward energy flux at 3ºN does not influence the group velocity of westward energy flux at the equator in the other periods. Meanwhile, since the westward transfer of energy flux at 3ºN forced by local wind forcing near 83ºE is in phase with the seasonal cycle, and may not be in

charge of the slower group velocity of westward energy flux at the equator. In the southeastern IO, the slightly slower phase signals of westward energy flux appear along 3ºS (pink line in Fig. 4.6f) as compared to the general group velocity of westward energy flux in the other seasons and neutral year (black line in Figs. 4.6c, f). These are off-equatorial RWs forced by the southeasterly winds in the southeastern IO with the predominant energy input by wind forcing at the central-eastern region of 3ºS (contour in Fig. 4.6f). This packet of westward RWs shifts towards the equator from the southeastern IO (Schopf *et al.,* 1981) in response to the influence of southeasterly winds and is intensified by easterly winds at the equator. This could account for the appearance of a slightly slower phase speed of RWs at the central-western equatorial IO. There exists another slower group velocity of westward energy flux during November 1994–June 1995 also induced by the extended southeasterly winds. However, energy input by wind forcing weakens from November and disappears in December at 3ºS, indicating the demise of southeasterly winds in the southeastern IO. This packet of off-equatorial RWs propagates westward along 3ºS towards the African coasts. In brief, the results illustrate the different group velocities of westward transfer of energy flux associated with RWs co-occurs with the anomalous southeasterly winds in the southeastern IO. Namely, the southeasterly winds trigger the slightly slower group velocity of westward transfer of energy flux associated with RWs that is connected to the equator and to the western IO.

To examine the development process of wave energy during the 1994 IOD event, we use the Helmholtz decomposition of the AGC17 level-2 energy flux:

$$-R_y - D_x = \rho_0 \overline{u^{(n)} p^{(n)}} + \rho_0 (\overline{p^{(n)} \varphi^{app}}/2)_y, \tag{4.2a}$$

$$+R_x - D_y = \rho_0 \overline{v^{(n)} p^{(n)}} - \rho_0 (\overline{p^{(n)} \varphi^{app}}/2)_x, \tag{4.2b}$$

where the scalar quantities R and D correspond to the rotational and divergent components of the energy flux, respectively (with a unit of W/m). The distributions of R (referred to as

energy-flux streamfunction) and D (referred to as energy-flux potential) are shown in Figs. 7 and 8, respectively. The positive contours and negative contours indicate wind input and energy dissipation in the corresponding region, respectively.

We have investigated evolution in 1990 (Fig. 4.7) and 1994 (Fig. 4.8) by analyzing the energy-flux streamfunction and potential based on a monthly mean. Both the northwest monsoon in February 1990 (Fig. 4.7a) and the southwest monsoon in August 1990 (Fig. 4.7c) generate the upwelling KWs near the African coasts propagating eastward. Westerly winds at the central equator induce downwelling KWs propagating toward the Sumatra coast (Figs. 4.7b, d). After these KWs arrive at the eastern boundary, they will bifurcate poleward. This is consistent with two sets of cyclonic circulations of wave energy in each hemisphere during the normal monsoon year demonstrated by LA20. Figure 4.8 shows the developing process of the 1994 pure positive IOD event where the westward signals of energy-flux streamfunction together with the moderate signals of wind input first appear by May in the southeastern IO (Fig. 4.8a). These features, such as westward signals and predominant wind input, intensify and migrate westward to the equator along the Indonesian archipelago during June–July (Figs. 4.8b, c). These westward signals are associated with the off-equatorial RWs and positive contours are attributed to energy input by southeasterly winds. These features reach the peak in August and are restricted in the southeastern regions (Fig. 4.8d). The intense westward signals and predominant wind input maintain power until September (Fig. 4.8e). With the weakening of southeasterly winds in the southeastern IO, the westward signals associated with off-equatorial RWs and energy input by southeasterly winds become weaker from October (Fig. 4.8f) and are about to terminate in November (Fig. 4.8g). This dipole event has a rapid demise in December (Fig. 4.8h).

4.3.3 EOF analysis

We have performed the combined EOF analysis for the anomalies of energy-flux streamfunction and potential. Here we have removed the climatological component of monthly data to examine the interannual variability of wave energy in the IO. The first combined EOF mode explains about 27% of the total variance of energy-flux streamfucntion and potential in the IO. The spatial pattern of the first EOF mode (Fig. 4.9a) shows that the westward signals related with the off-equatorial RWs appear in the southeastern IO. Simultaneously, the positive signals of energy-flux potential corresponding to the predominant wind input are dominated in the southeastern IO indicating the energy supplied by southeasterly winds. This kind of pattern appears as the most dominant mode and is consistent with the distinct features during a dipole event year, such as the well-developed pattern in August 1994 (Fig. 4.8d). Temporal projection of leading combined EOF mode represents interannual variations and is coincident with the results of 61-year hindcast experiments. The times series of the first combined EOF mode represents some positive peaks during 1961, 1982, 1994, 1997, and 2006 (yellow and green shaded columns in Fig. 4.9c) that are consistent with the reproduced major positive IOD events as shown in Fig. 1a. The 1966, 1967, and 1972 positive IOD events described in Fig. 4.1a are less pronounced in temporal projection of the first EOF mode. Note that the 1964, 2010, and 2016 peaks are related to the negative IOD events.

The second and third combined EOF modes explain about 21.8% (Figs. 4.9b, d) and 10.63% (figure not shown) of the total energy-flux streamfunction and potential variance in the IO, respectively. The energy-flux streamfunction in the second mode shows the typical interannual behavior in the spatial pattern. The powerful westward transfer of wave energy related to the off-equatorial RWs is prevailing in the southeastern IO. The spatial pattern of energy-flux potential (Fig. 4.9b) in the second dominant mode shows positive loading in the

eastern equatorial IO and negative loading in the Arabian Sea. The positive value of energy-flux potential indicates the wind input peak in the eastern equatorial IO. This intense energy input by anomalous winds in an IOD event plays a leading role in triggering the wave energy transfer. The energy-flux potential becomes negative in the Arabian Sea where wave energy is dissipated owing to eddy viscosity. The time evolution of combined EOF second mode (Fig. 4.9d) agrees with the 1994 and 2006 positive IOD events.

4.4 Conclusions

The present study has investigated the transfer routes of wave energy during the 1994 positive IOD event, in an attempt to examine the applicability of the AGC17 scheme to phenomena at interannual timescales. We have conducted 61-year hindcast experiments in the IO to offer a good comparison with the reanalysis results of 20°C isotherm depth in ECMWF ORAS3. Analyzing the time evolution of energy flux along the equator during the 1994 pure positive IOD event, we have found two sets of westward transfer signals associated with RWs. The first set has the phase speed in agreement with the linear theory of equatorial RWs. This set is attributed to the boundary-reflected equatorial RWs at the eastern basin of the IO from equatorial KWs. The second set is slightly slower than the theoretical phase speed of equatorial RWs. This set is found to be given by off-equatorial RWs originating from southeasterly winds initiated from the southeastern IO, which may be responsible for the appearance of a slightly slower group velocity of westward energy flux along the equator. The energy flux along 3ºN during 1994 is characterized by the seasonal cycle, while that along 3ºS exhibits interannual variations under the influence of extended southeasterly winds.

We have examined the development process of wave energy during 1994 using the AGC17 scheme based on the monthly mean of 3.65-day snapshots. In the leading month, the positive signals of energy-flux streamfunction together with positive contours of energy-flux

potential appear in the southeastern IO. The positive curl in the southeastern IO is in response to energy input by southeasterly winds. These signals develop and shift westward toward the equator along the Indonesian archipelago. Westward transfer signals of energy-flux streamfunction are coincident with the westward off-equatorial RWs generated by southeasterly winds. It has a markedly rapid peaking of the powerful off-equatorial RWs and predominant wind input in August and is maintained until September. Whether or not this slower RW propagation is also identified from reanalysis data with realistic thermocline distribution and with atmospheric heat forcing is subject to investigation in a future study using the AGC17 scheme. Southeasterly winds become weak leading to the cut-off of westward propagation signals from October. This dipole event ceased at the end of 1994. Using the combined EOF analysis of energy-flux streamfunction and potential, we have shown that the features during a positive IOD event, such as the intense westward signals associated with wind-generated off-equatorial RWs and predominant wind input by southeasterly winds in the southeastern IO, appear as the most dominant mode.

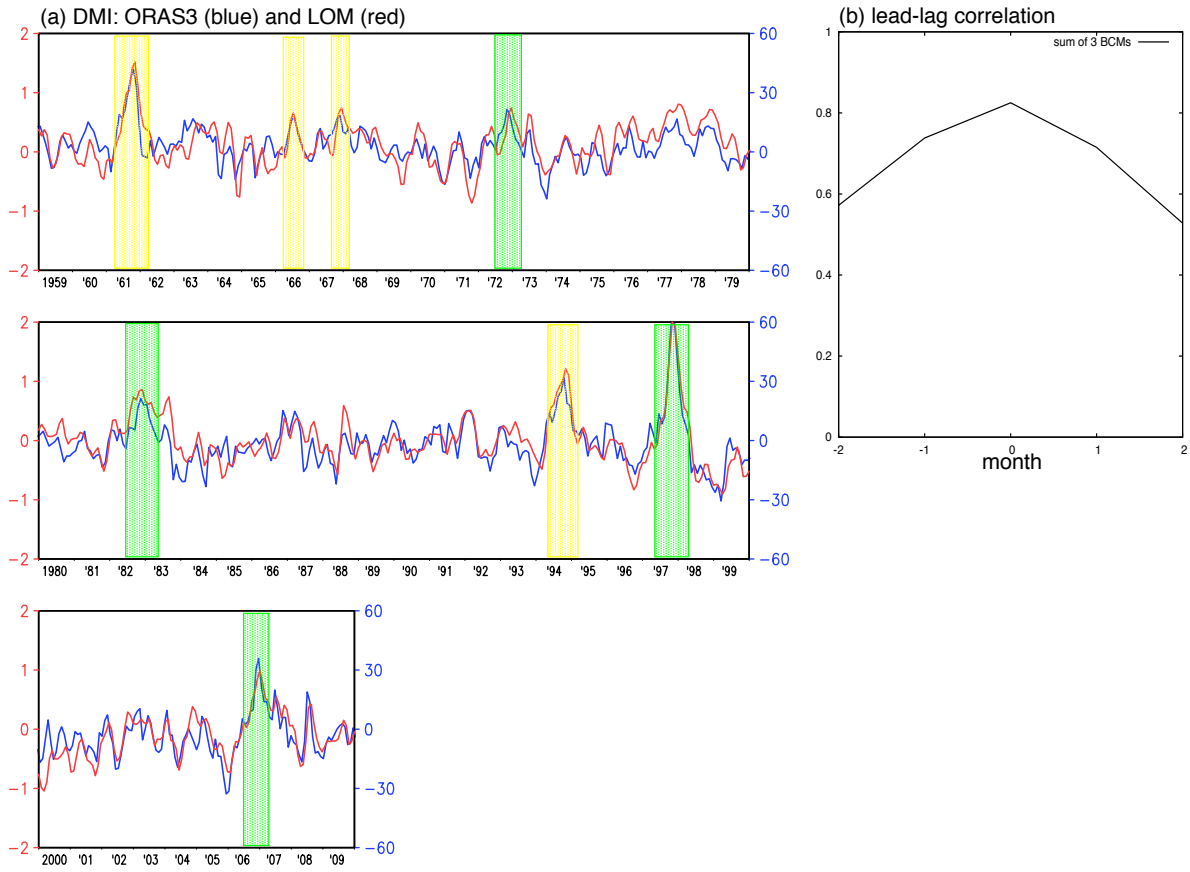

Figure 4.1 (a) Comparisons of Dipole Model Index during 1959–2009. Blue line represents 20°C isotherm depth (with a unit of m shown by the vertical axis tics on the right) from ECMWF ORAS3. Red line represents sea surface geopotential simulated by linear ocean model (LOM, with a unit of m^2/s^2 as shown by the vertical axis tics on the left). Yellow shaded columns indicate pure positive IOD events and green shaded columns indicate IOD-ENSO concurrent positive IOD events. (b) Lead-lag correlation between reanalysis results (blue line) and model output (red line). The simultaneous correlation coefficient of is 0.825. The positive lags signify that LOM leads ORAS3.

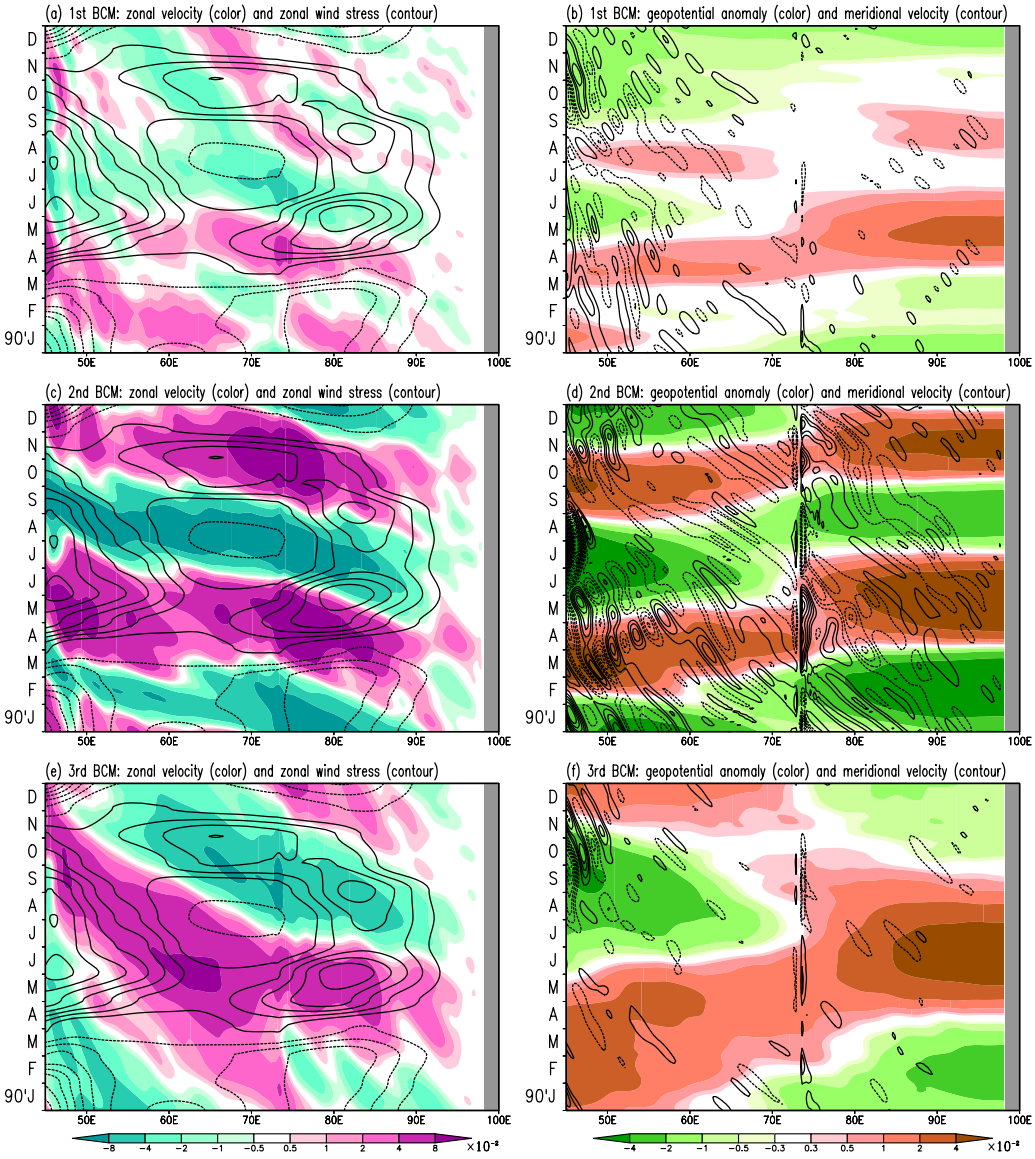

Figure 4.2 Hovmöller diagrams along the equator for the simulated results during 1990 of our hindcast experiments associated with the first (a, b), second (c, d), and third (e, f) baroclinic modes. Left panels (a, c, e) represent simulated zonal velocity (color shading, m/s) and wind stress (solid and dashed contours for westerly and easterly wind stress, respectively, with an interval of 0.005 N/m^2). Right panels (b, d, f) represent simulated geopotential anomaly (color shading with a unit of m/s, rescaled as $p^{(n)}/c^{(n)}$ to follow the definition of gravitational potential energy) and meridional velocity (solid and dashed contours for northward and southward currents, respectively, with an interval of 0.01 m/s).

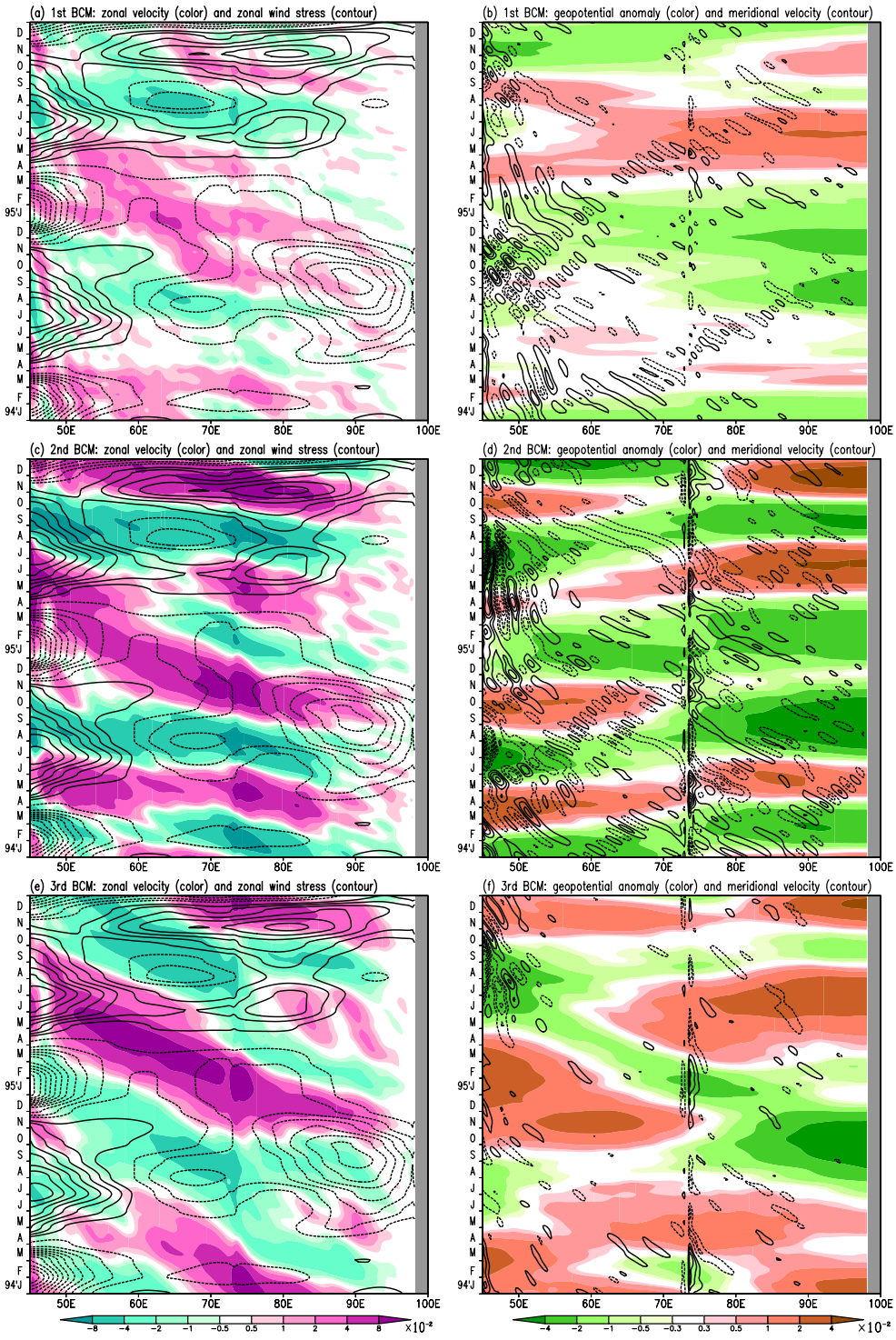

Figure 4.3 Same as Fig. 4.2, except for 1994–95.

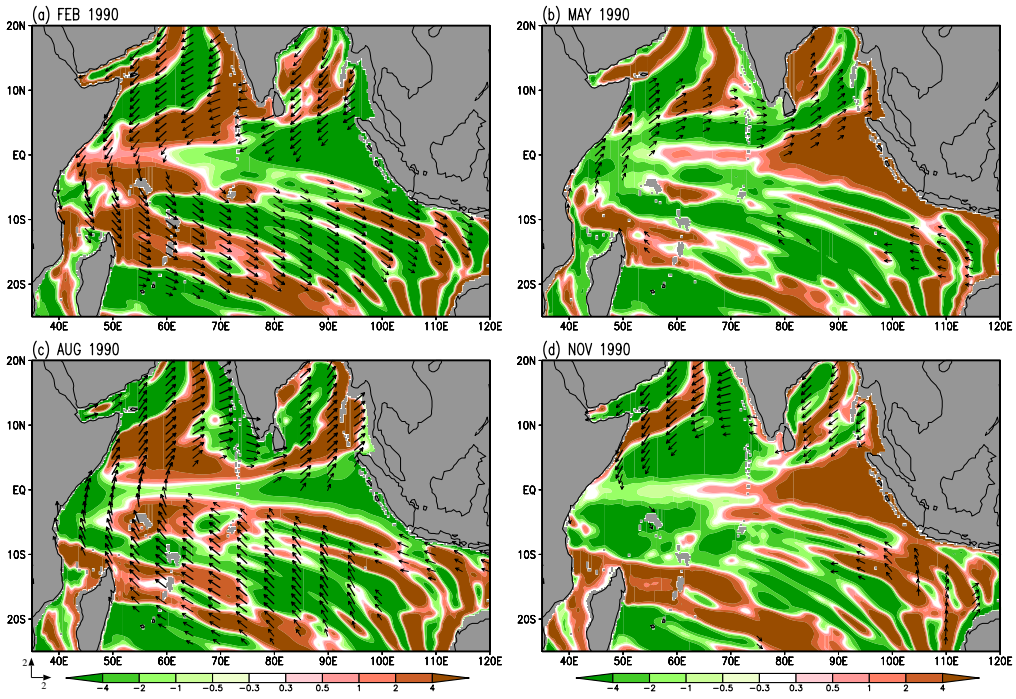

Figure 4.4 Seasonal evolution of geopotential anomaly (color shading, m^2/s^2) and wind stress vector (arrows, N/m^2) for the simulated results in February, May, August, and November of 1990 of our hindcast experiments associated with the second baroclinic mode.

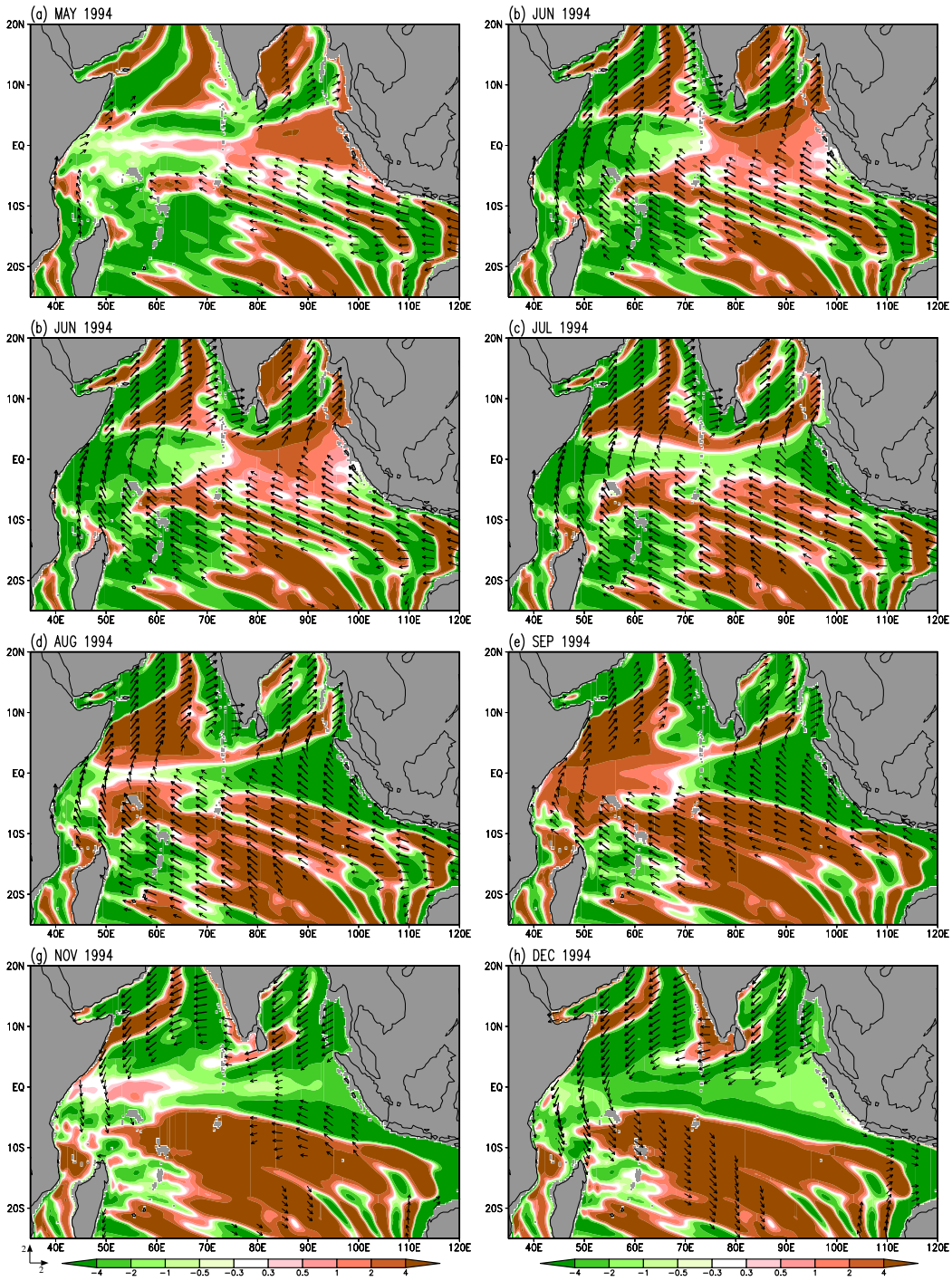

Figure 4.5 Same as Fig. 4.4, except for 1-month interval from May 1994 to December 1994.

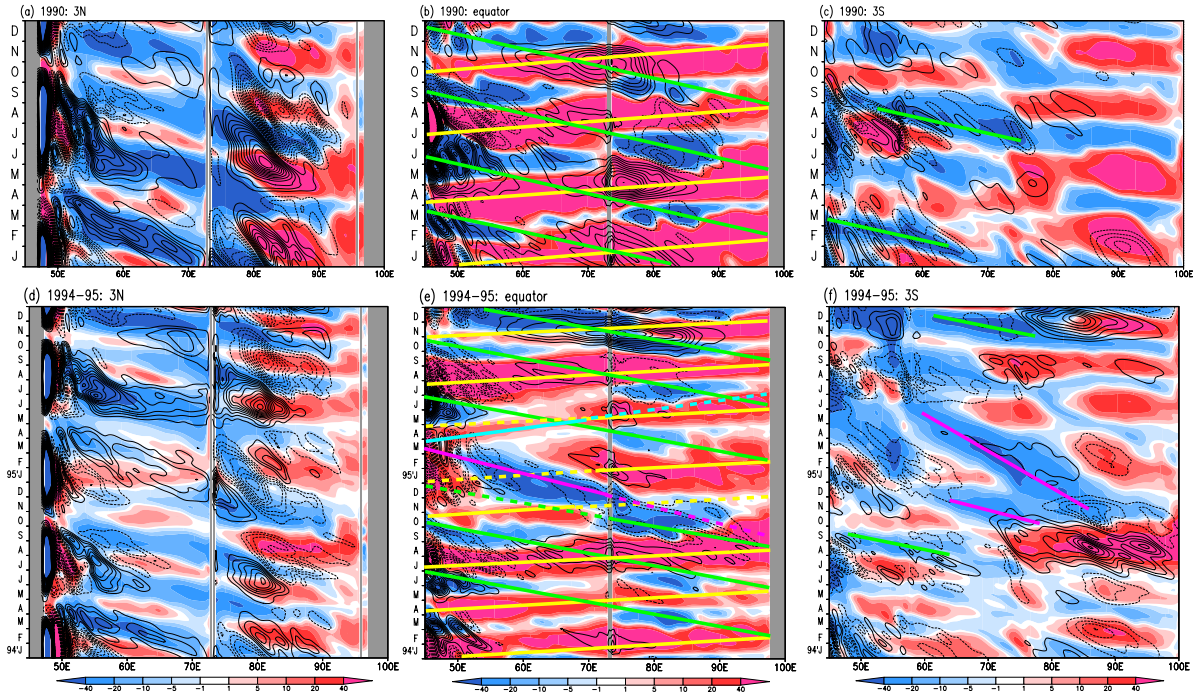

Figure 4.6 Hovmöller diagrams along 3°N (left panels), the equator (middle panels), and 3°S (right panels) for the results (a, b, c) during 1990 and (d, e, f) 1994–95 of our model experiment with the second baroclinic mode. Color shading shows the energy-flux (W/m) with positive and negative values indicating eastward and westward, respectively, as estimated by the AGC17 scheme. Contours show the energy input by wind forcing with an interval of 0.001 W/m with positive value indicating the westward currents accelerated and negative value indicating the eastward currents decelerated by easterly winds. Yellow and green lines indicate the theoretical phase speed of KWs and RWs, respectively. Light blue and magenta lines represent the slower phase speed of KWs and RWs, respectively. The solid and dashed lines correspond to the actual existence and nonexistence of KWs and RWs, respectively.

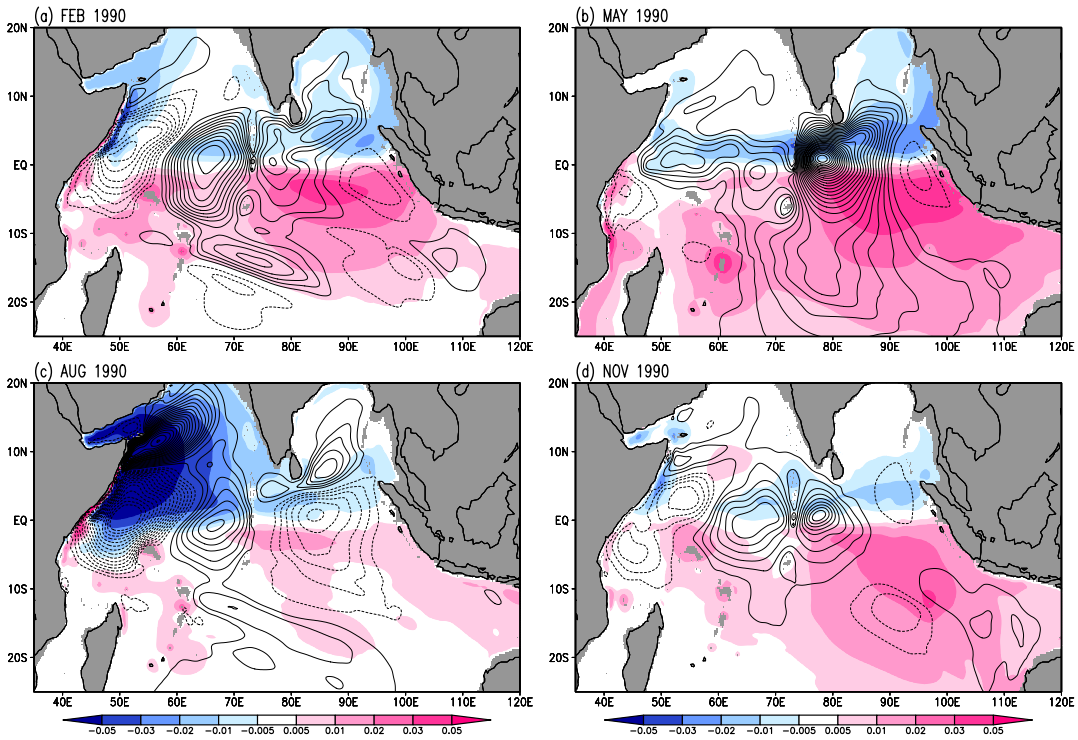

Figure 4.7 Monthly evolution of energy-flux streamfunction R (color shading, unit 10^9 W = giga watts) and energy-flux potential D (contour, unit 10^6 W) in February, May, August, and November of 1990 computed using the AGC17 scheme (4.2a)–(4.2b) based on the monthly mean. The results are associated with the sum of the first three baroclinic modes.

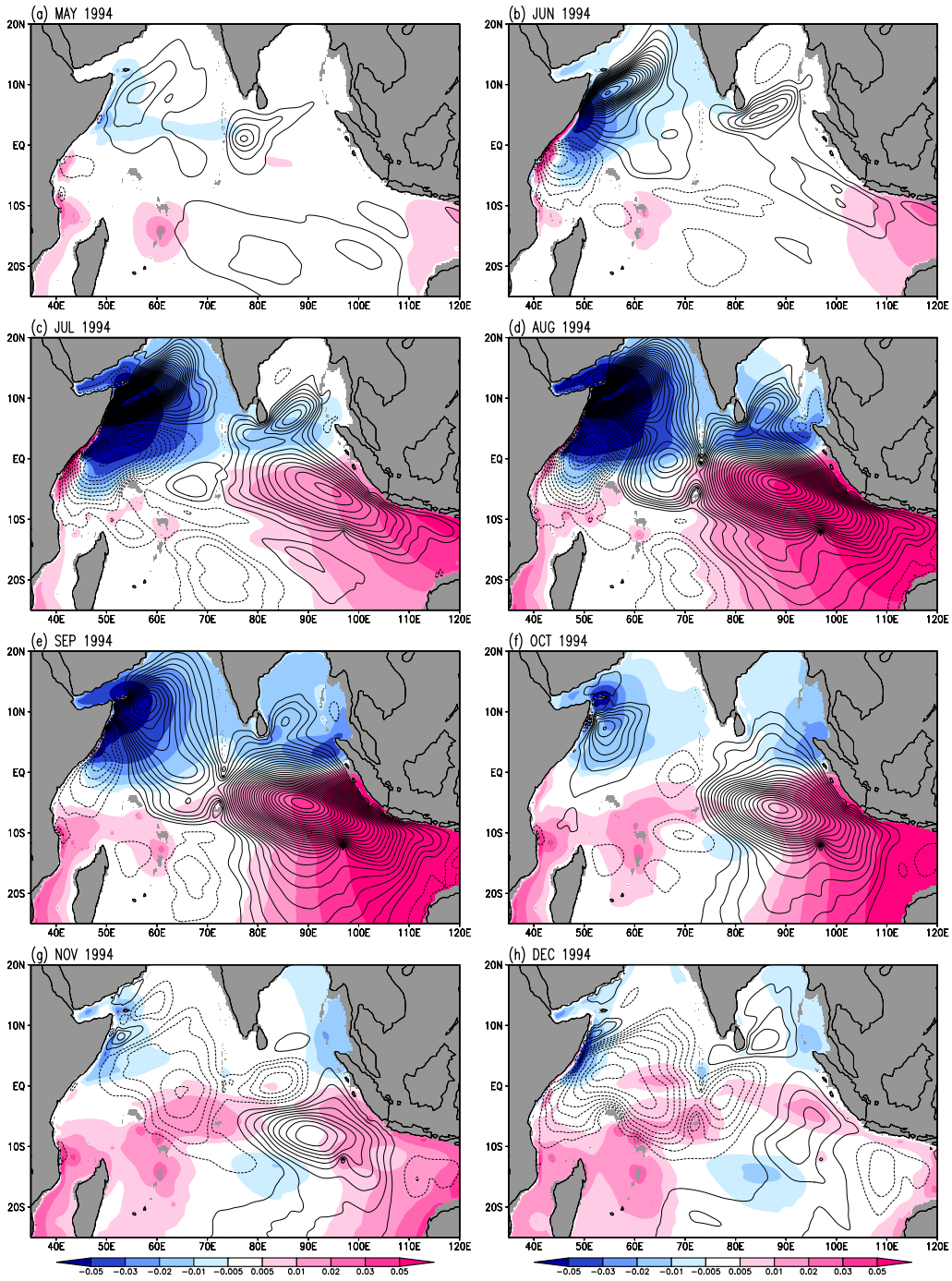

Figure 4.8 Same as Fig. 4.5, except for 1-month interval from May 1994 to December 1994.

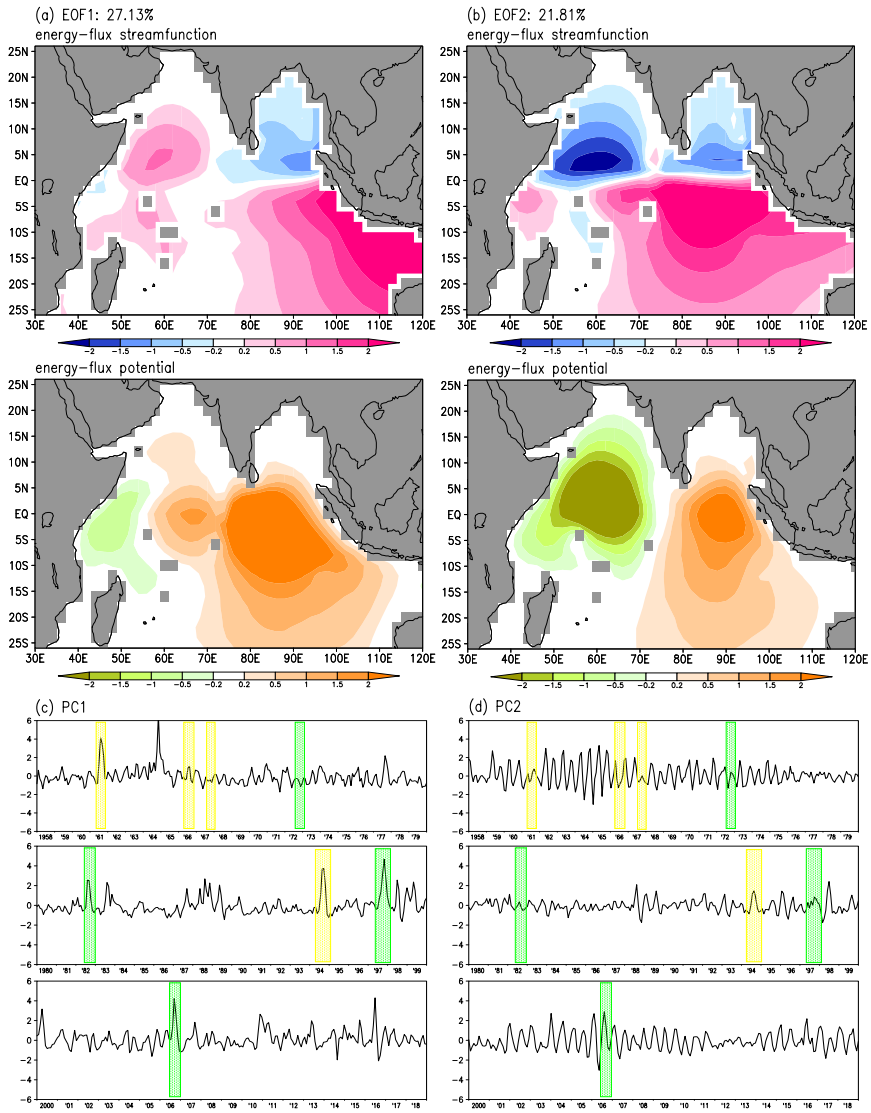

Figure 4.9 Results of the combined EOF analysis for energy-flux streamfunction (upper panels: color shading for positive values in pink and negative values in dark blue, unit 10^9 W = giga watts) and energy-flux potential (middle panels: color shading for positive values in orange and negative values in green, unit 10^6 W) computed using the AGC17 scheme. (a), (b), and (c) horizontal patterns and (d), (e), and (f) temporal patterns associated with the first, second, and third modes, respectively. All results are associated with the sum of the first three baroclinic modes during 61-year hindcast model experiments. Yellow and green shaded columns are same as in Fig. 4.1a.

Chapter 5

General Discussion

There are several scientifically interesting phenomena, such as seasonal monsoons and IOD, that occur in the IO. The distribution and development process of wave energy excited by these phenomena are poorly understood owing to the lack of applicable approaches. The present study provides a new perspective on the variations in the IO by tracing the transfer routes of wave energy. This approach is an insight into the atmosphere-ocean interactions. There have at least three diagnostic schemes for calculating group velocity vectors. Chapters 2 and 3 compare the capacity for tracing the transfer episodes of energy flux of three schemes, the pressure flux scheme, OS93 scheme, and the newly proposed AGC17 scheme at the horizontal and vertical structure, respectively. The pressure flux scheme (Cummins and Oey, 1997) is appropriate for the identification of inertia-gravity waves but fails to trace the off-equatorial RWs. The OS93 scheme makes up for the insufficient of mid-latitude RWs but is unable to show the direction of group velocity vectors near equatorial regions. AGC17 scheme is a seamless diagnostic scheme, which can offer a good expression of directional group velocity vectors for all waves with a smooth transition between equatorial and off-equatorial regions. The above results suggest that the AGC17 scheme is a well-documented approach to investigate the generation, propagation, reflection, diffraction, and dissipation of wave energy at all latitudes in both horizontal and vertical sections.

The simulated results, such as zonal velocity and geopotential in chapters 2–4 using linear ocean model based on the numerical experiments are in accordance with most basic features of the climatological and interannual circulations in response to the seasonal monsoonal winds and IOD, respectively. We validate the model by comparing the output

with the OGCM OFES data at seasonal timescales and ORAS3 at interannual timescales. The results, the similar distribution pattern and high lead-lag correlation coefficient of 0.806, suggest our model is an effective approach to reproduce the monsoonal variations and IOD events in the IO. Concerning the basin mode period is nearly half a year in the second baroclinic mode, it is suitable for analyzing the seasonal variations of equatorial IO (Nagura and McPhaden, 2010). The SC driven by the southwest and northeast monsoon flowing along the East African coast in charge of upwelling signals and the Wyrtki jet forced by westerly winds along the equator during the monsoon transition period associated with downwelling signals is well reproduced in the second baroclinic mode. The zonal velocity and geopotential anomaly change directions four times per year in the second baroclinic mode in both horizontal and vertical structures are the evidence for these phenomena. The zonal velocity shows the four sets of westward signals associated with equatorial RWs but KWs are slightness. The geopotential anomaly has the capacity to show the propagation of the equatorial KWs but fails to show RWs. These raw quantities can show the evident seasonal variations but have the disadvantage for show the transfer routes of wave energy. To fill the gap of insufficient understanding of the wave energy transfer, we use the AGC17 scheme to trace the horizontal and vertical transfer of wave energy driven by the monsoonal wind forcing. The propagation of wave energy in both surface and depth planes is characterized by the seasonal cycle. The equatorial KWs appear four times along the equator with powerful wind put signals in response to the southwest and northeast monsoon at both surface and depth plane. Considering the formation mechanism of the SC, the western basin forms a localized cyclonic circulation at the sea surface during boreal winter and summer. The beams of KWs sustain in May and August at 550 m depth and in November at 1100 m depth, indicating the 3 months lead-lag between surface and mid-depth. These sets of KWs reflect diffract both equatorial and off-equatorial RWs. This forms the symmetrical distribution of

westward energy flux of RWs in the latitude-depth plane and the basin-scale cyclonic circulation of wave energy considering the rotational and divergent components of wave energy at the eastern basin in the surface plane. The north branch of diffraction of equatorial KWs transfers westward off-equatorial RWs to BoB. The vertical component of this westward energy flux reaches the deepest depth in SBoB (3°–5N, 90°E) in November–December. Concerning the generation of this set of RW, it is strongly associated with the downwardly propagating equatorial KWs instead of the wind forcing at the sea surface.

The present study is the first application of the AGC17 scheme at interannual timescales in the IO described in chapter 4, we pick up a pure positive IOD event that occurred during 1994. By comparing with a neutral year like 1990, when IOD is in a positive phase in 1994, the abnormal easterly winds appear by May and sustain until the end of the year, which excites the persistent upwelling over central-eastern IO in July–December. These winds get a peak in August–September and weaken from November leading to the termination of IOD in December. Theoretically, the equatorial KWs are 3 times faster than equatorial RWs and take 6 months for one round trip to cross the zonal equatorial IO. In the second baroclinic mode of 1994 positive IOD, the period for equatorial KWs and reflected equatorial RWs takes 8 months. This is attributed to the existence of two sets of westward energy flux of RWs along the equator. At central-eastern IO, the general equatorial RWs is generated by the boundary reflection of equatorial KWs in August–October. It is worth noting that an extra set of westward transfer of energy flux appear near the central-western basin during positive IOD in November 1994–March 1995, which shows a slightly slower group velocity than the theoretical equatorial RWs. It is necessary to estimate the disturbance of abnormal wind forcing and interactions between the tropical and subtropical IO. The results suggest that off-equatorial RWs are the key factor for the appearance of the slower phase speed of RWs transfer rather than the abnormal southeasterly winds.

An EOF analysis for SST anomaly (Behera *et al.*, 2006) in the tropical IO shows that the IOD is independent of ENSO the former and latter of which appears in the EOF second and first modes. We conduct a combined EOF analysis for energy-flux streamfunction and potential based on the monthly mean in the IO. The most dominant mode shows the pattern of westward transfer of wave energy excited by the wind forcing of southeasterly winds over the central-southeastern IO. This pattern is the unique distribution of interannual features of a positive IOD.

Chapter 6

General Conclusion

6.1 Concluding remarks

There are several climate variability modes in the global atmosphere-ocean system, such as ENSO in the Pacific Ocean, the IOD, and the Madden-Julian Oscillation in the IO. This study focuses on investigating the seasonal and interannual variations in the IO through an energetic view. The mechanism of the variations in the IO is closely linked to the characteristics of equatorial KWs and RWs in the ocean. Based on the analysis of raw quantities, the westward propagation signals of RWs are visible in the seasonal pattern of zonal velocity whereas eastward propagation signals of KWs are unclear. The present study provides a new interpretation of the mechanism of oceanic dynamics in the tropical IO based on the linear ocean model driven by different components of wind forcing. To trace the transfer routes of wave energy, we apply a new diagnostic scheme recently proposed in AGC17. We have compared the performance of previous schemes and the new scheme in horizontal and vertical structures, respectively, to find suitable diagnostic techniques. The results show that the AGC17 scheme is more appropriate for tracing the processes of all waves, such as wave reflection at the boundaries and diffraction at the coastal regions through all latitudes. According to the results of group-velocity vectors calculated by applying the AGC17 scheme, the present study quantifies the significance of the transfer episodes of wave energy at seasonal and interannual timescales with a smooth transition between the tropical and subtropical regions in the IO.

An important point is why the present study focuses on the IO. As compared to the Atlantic and Pacific Oceans, the IO has more seasonal variations than interannual variations. In response to the monsoonal winds, the wave circulations in the IO have been defined in a

horizontal structure. In boreal winter and summer, the localized cyclonic energy circulation is formed in each hemisphere near the western basin of the IO in relation to the southwesterly winds. While, near the eastern basin of the IO, it shows a basin-scale cyclonic energy circulation in the monsoon transition period is closely linked to the wave reflection and diffraction at the eastern boundary forced by the westerly winds along the equator. Eastward energy flux is in the phase of seasonal variations at the surface which has four peaks related to the upwelling KWs in boreal winter and summer and downwelling KWs in boreal spring and fall. In the view of vertical structure, these packets of wave energy generated by monsoonal winds along the equator at the surface will transfer energy downwardly and lead 3 months before mid-depth. Particularly, the deepest penetration of wave energy appears in SBoB regions in November–December, which shows the most apparent signals at 3°–5°N, 90°E associated with the downward energy flux of RWs derive from the boundary reflection and diffraction of mid-depth equatorial KWs in August.

Based on the findings at seasonal timescales, we further apply the AGC17 scheme at the interannual timescales in the tropical IO. This study first focuses on the 1994 pure positive IOD event. Two sets of westward transfer signals of energy flux are found along the equator with different phase speeds during 1994 positive IOD. One set is reflected by equatorial KWs at the eastern boundary, which has the same phase speed as the theoretical equatorial RWs. The other set is transferred from the off-equatorial RWs, which propagates slower along the equator than the theoretical equatorial RWs. We analyzed the development process of 1994 positive IOD by tracing the transfer routes of wave energy. The westward signals of wave energy with wind input by southeasterly winds start in May and develop in June–July. These features of a positive IOD get a peak in August and maintain power until September. From October, the southeasterly winds weaken, which will the strength of westward propagating wave energy. This contributes to the termination of the dipole event at the end of 1994.

The application of the approach of this study to the analysis of the variability's teleconnection in the tropical IO can help general citizens have a better understanding of the forecast/nowcast/hindcast in the world's climate centers, such as Europe Centre for Medium-Range Weather Forecasts, National Centers for Environmental Prediction in USA, and Japan Meteorological Agency.

6.2 Suggestions for future research

The present study pays attention to the seasonal and interannual variabilities of wave energy in the tropical IO by applying the AGC17 scheme. The preliminary application of the AGC17 scheme to analyze the dynamics of IO provides a set of unveiled views for the geographical distribution of wave energy transfer and is a new metric for looking at the interrelationship of waves and circulations in the IO.

To examine the interannual variability of wave energy, the chapter 4 preliminarily focuses on a pure positive IOD event, the important of oceanic waves perturbations in negative phase is also a necessary consideration. It is well known that SSTa evolution pattern show opposite loading on western and eastern basin of IO during positive and negative IODs and the heat budget of tropical IO during IOD play an important role on the initiation and termination of an IOD event. The evolution of wave energy of negative IOD events should be further understood whether it has the opposite pattern of wave energy as SSTa or not.

It is worth noting that the IO is unique in that it is connected to the Pacific Ocean through over Indonesian Archipelago. There exists a unique phenomenon, Indonesian Throughflow, which is an important process of exchange between the Pacific Ocean and the IO. Out of a set of constituents missed in our model setup, the present study reminds the possible importance of the Indonesian Archipelago. The KWs could transfer energy eastwardly into the Pacific Ocean by Indonesian Throughflow. This flow also includes the westward propagating wave energy related to the RWs from the Pacific Ocean. Future

detailed work is necessary to make clear the importance of Indonesian Throughflow. This may further enrich our understanding of the oceanic tunnel process as well as climate variation.

In addition, energy dissipation is significant in the western basin of the tropical IO. The boundary currents along the African coasts should be considerable. The AGC17 scheme is presently applicable to linear ocean model without a mean flow which is the limitation of this study. Namely, we simulated the perturbation of waves, the model output is not improved with the existence of a mean flow. The details of this lack of baroclinic instability should be further examined in a future study based on regional statistics.

References

Aiki, H., Greatbatch, R. J., & Claus, M. (2017), Towards a seamlessly diagnosable expression for the energy flux associated with both equatorial and mid-latitude waves, *Prog. Earth Planet Sci.*, **4**(11), https://doi.org/10.1186/s40645-017-0121-1.

Aiki, H., Fukutomi, Y., Kanno, Y., Ogata, T., Toyoda, T., & Nakano, H. (2021), The energy flux of three-dimensional waves in the atmosphere: Exact expression for a basic model diagnosis with no equatorial gap, *J. Atmos. Sci.*, **78**(11), 3745–3758, https://doi.org/10.1175/JAS-D-20-0177.1.

Ashok, K., Guan, Z., & Yamagata, T. (2003), A look at the relationship between the ENSO and the Indian Ocean Dipole, *J. Meteor. Soc. Japan*, **81**, 41–56, https://doi.org/10.2151/jmsj.81.41.

Beal, L., Hormann, V., Lumpkin, R., & Foltz, G. (2013), The response of the surface circulation of the Arabian Sea to monsoonal forcing, *J. Phys. Oceanogr.*, **43**(9), 2008–2022, https://doi.org/10.1175/JPO-D-13-033.1.

Behera, S. K., Krishnan, R., & Yamagata, T. (1999), Unusual ocean-atmosphere conditions in the tropical Indian Ocean during 1994, *Geophys. Res. Lett.*, **26**, 3001–3004. https://doi.org/10.1029/1999GL010434.

Behera, S. K., Luo, J. J., Masson, S., Rao, S. A., Sakuma, H., & Yamagata, T. (2006), A CGCM Study on the interaction between IOD and ENSO, *J. Clim.*, **19**(9), 1688–1705, https://doi.org/10.1175/JCLI3797.1

Brandtm, P., Eden, C. (2005), Annual cycle and interannual variability of the mid-depth tropical Atlantic Ocean, *Deep-Sea Res.*, **52**(2),199–219, https://doi.org/10.1016/j.dsr.2004.03.011.

Brigadier, L., Ogwang, B. A., Ongoma, V., Ngonga, C., & Nyasa, L. (2016), Diagnosis of the 2010 DJF flood over Zambia, *Natural Hazards*, **81**, 189–201,

https://doi.org/10.1007/s11069-015-2069-z.

Cai, W., Meyers, G., & Shi, G. (2005), Transmission of ENSO signal to the Indian Ocean, *Geophys. Res. Lett.*, **32**, L05616, https://doi.org/10.1029/2004GL021736.

Cane, M. A., Gent, P. R. (1984), Reflection of low-frequency equatorial waves at arbitrary western boundaries, *J. Mar. Res.*, **42**, 487–502, https://doi.org/10.1357/002224084788505988.

Chakravorty, S., Chowdary, J. S., & Gnanaseelan, C. (2013) Spring asymmetric mode in the tropical Indian Ocean: role of El Niño and IOD, *Clim. Dyn.*, **40**, 1467–1481, https://doi.org/10.1007/s00382-012-1340-1.

Chakravorty, S., Gnanaseelan, C., Chowdary, J. S., & Luo, J. J. (2014), Relative role of El Niño and IOD forcing on the southern tropical Indian Ocean Rossby waves, *J. Geophys. Res.*, **119**, 5105–5122, https://doi.org/10.1002/2013JC009713.

Chelton, D. B., Schlax, M. G. (1996), Global observations of oceanic Rossby waves, *Science*, **272**(5259), 234–238, https://www.jstor.org/stable/2889630.

Chen, G., Han, W., Li, Y., Wang, D., & McPhaden, M. J. (2015a), Seasonal-to-interannual time-scale dynamics of the equatorial undercurrent in the Indian Ocean, *J. Phys. Oceanogr.*, **45**, 1532–1553, https://doi.org/10.1175/JPO-D-14-0225.1.

Chen, G., Han, W., Li, Y., Wang, D., & Shinoda, T. (2015b), Intraseasonal variability of upwelling in the equatorial Eastern Indian Ocean, *J. Geophys. Res.*, **120**, 7598–7615, https://doi.org/10.1002/2015JC011223.

Chen, G., Han, W., & Li Y. (2016), Interannual variability of equatorial eastern Indian Ocean upwelling: Local versus Remote Forcing, *J. Phys. Oceanogr.*, **49**, 1573–1596, https://doi.org/10.1175/JPO-D-15-0117.1.

Chen, G., Han, W., Li, Y., McPhaden, M. J., Chen, J., Wang, W., & Wang, D. (2017), Strong Intraseasonal variability of meridional currents near 5°N in the eastern Indian

Ocean: Characteristics and Causes, *J. Phys. Oceanogr.*, **47**(5), 979–998. https://doi.org/10.1175/JPO-D-16-0250.1.

Chen, G., Li, Y., Xie, Q., & Wang, D. (2018), Origins of eddy kinetic energy in the Bay of Bengal, *J. Geophys. Res.*, **123**, https://doi.org/10.1002/2017JC013455.

Chen, G., Han, W., Li, Y., Yao, J., & Wang, D. (2019), Intraseasonal variability of the Equatorial Undercurrent in the Indian Ocean, *J. Phys. Oceanogr.*, **49**, 85–101, https://doi.org/10.1175/JPO-D-18-0151.1.

Chen, Z., Wang, X., & Liu, L. (2020), Reconstruction of three-dimensional ocean structure from sea surface data: an application of isQG method in the southwest Indian Ocean, *J. Geophys. Res. Oceans*, **125**, e2020JC016351. https://doi.org/10.1029/2020JC016351.

Cummins, P. F., Oey L.Y., (1997), Simulation of barotropic and baroclinic tides off northern British Columbia, *J. Phys. Oceanogr.,* **27**, 762–781, https://doi.org/10.1175/1520-0485(1997)027%3C0762:SOBABT%3E2.0.CO;2.

Delman, A. S., Sprintall, J., McClean, J. L., & Talley, L. D. (2016), Anomalous Java cooling at the initiation of positive Indian Ocean Dipole events, *J. Geophys. Res.*, **121**, 5805–5824, https://doi.org/10.1002/2016JC011635.

Dewitte, B., Reverdin, G. (2000), Vertically propagating annual and interannual variability in an OGCM simulation of the tropical Pacific Ocean in 1985–94, *J. Phys. Oceanogr.*, **30**, 1562–1581, https://doi.org/10.1175/1520-0485(2000)030%3c1562:VPAAIV%3e2.0.CO;2.

Ding, H., Keenlyside, N. S., & Latif, M. (2009), Seasonal cycle in the upper equatorial Atlantic Ocean, *J. Geophys. Res.*, **114**, C09016, https://doi.org/10.1029/2009JC005418.

Drushka, K,. Sprintall, J., Gille, S., & Brodjonegoro, I. (2010), Vertical structure of Kelvin

waves in the Indonesian Throughflow, *J. Phys. Oceanogr.*, **40**,1965–1987, https://doi.org/10.1175/2010JPO4380.1.

Du, Y., Zhang, Y., Zhang, L. Y., Tozuka, T., Ng, B., & Cai, W. (2020), Thermocline warming induced extreme Indian Ocean dipole in 2019, *Geophys. Res. Lett.*, **47**, e2020GL090079, https://doi.org/ 10.1029/2020GL090079.

Düing, W., Schott, F. (1978), Measurements in the source region of the Somali current during the monsoon reversal, *J. Phys. Oceanogr.*, **8**, 278–289, https://doi.org/10.1175/1520-0485(1978)008%3C0278:MITSRO%3E2.0.CO;2.

Fukutomi, Y., Yasunari, T. (2002), Tropical-extratropical interaction associated with the10–25-day oscillation over the western Pacific during the northern summer, *J. Meteo. Soc. Japan*, **80**, 311–331, https://doi.org/10.2151/jmsj.80.311.

Fu, L. L. (2007), Intraseasonal variability of the equatorial Indian Ocean observed from sea surface height, wind, and temperature data, *J. Phys. Oceanogr.*, **37**, 188–202, https://doi.org/10.1175/JPO3006.1.

Gent, P. R., O'Neill, K., & Cane, M. A. (1983), A model of the semiannual oscillation in the equatorial Indian Ocean, *J. Phys. Oceanogr.*, **13**(12), 2148–2160, https://doi.org/10.1175/1520-0485(1983)013%3C2148:AMOTSO%3E2.0.CO;2.

Gill, A. E. (1982), Atmosphere-ocean dynamics. *Academic Press*, London, pp 662.

Guan, Z., Yamagata, T. (2003) The unusual summer of 1994 in East Asia: IOD teleconnections, *Geophys. Res. Lett.*, **30**, 1544, https://doi.org/10.1029/2002GL016831.

Halkides, D. J., Lee, T. (2009), Mechanisms controlling seasonal-to-interannual mixed layer temperature variability in the southeastern tropical Indian Ocean, *J. Geophys. Res. Oceans*, **114**, C02012. https://doi.org/10.1029/2008JC004949.

Han, W., McCreary, J. P., Anderson, J. D. L. T., & Mariano, A. J. (1999), On the dynamics

of the eastward surface jets in the equatorial Indian Ocean, *J. Phys. Oceanogr.*, **29**, 2191–2209, https://doi.org10.1175/1520-0485(1999)029%3c2191:DOTESJ%3e2.0.CO;2.

Han, W. (2005), Origins and dynamics of the 90-day and 30–60-day variations in the equatorial Indian Ocean, *J. Phys. Oceanogr.*, **35**, 708–728, https://doi.org/10.1175/JPO2725.1.

Hayes, S. P., Milburn, H. B. (1979), On the vertical structure of velocity in the eastern equatorial Pacific, *J. Phys. Oceanogr.*, **10**, 633–635, https://doi.org/10.1175/1520-0485(1980)010%3c0633:OTVSOV%3e2.0.CO;2.

Hong, C. C., Lu, M. M., & Kanamitsu, M. (2008), Temporal and spatial characteristics of positive and negative Indian Ocean dipole with and without ENSO, *J. Geophys. Res.*, **113**, D08107, https://doi.org/10.1029/2007JD009151.

Horii, T., Hase, H., Ueki, I., & Masumoto, Y. (2008), Oceanic precondition and evolution of the 2006 Indian Ocean dipole, *Geophys. Res. Lett.*, **35**, L03607, https://doi.org/10.1029/2007GL032464.

Huang, B., Kinter, J. L. (2002), Interannual variability in the tropical Indian Ocean, *J. Geophys. Res.*, **107**, 3199, https://doi.org/10.1029/2001JC001278.

Huang, K., Han, W., Wang, D., Wang, W., Xie, Q., Chen, J., & Chen, G. (2018a), Features of the equatorial intermediate current associated with basin resonance in the Indian Ocean, *J. Phys. Oceanogr.*, **48**, 1333–1347, https://doi.org/10.1175/JPO-D-17-0238.1.

Huang, K., McPhaden, M. J., Wang, D., Wang, W., Xie, Q., Chen, J., Shu, Y., Wang, Q., Li, J., & Yao, J. (2018b), Vertical propagation of mid-depth zonal currents associated with surface wind forcing in the equatorial Indian Ocean, *J. Geophys. Res.*, **123**, 7290–7307, https://doi.org/10.1029/2018JC013977.

Huang, K., Wang, D., Han, W., Feng, M., Chen, G., Wang, W., Chen, J., & Li, J. (2019).

Semiannual variability of middepth zonal currents along 5°N in the eastern Indian Ocean: Characteristics and causes, *J. Phys. Oceanogr.*, **49**, 2715–2729, https://doi.org/10.1175/JPO-D-19-0089.1.

Iskandar, I., McPhaden, M. J. (2011), Dynamics of wind-forced intraseasonal zonal current variations in the equatorial Indian Ocean, *J. Geophys. Res.*, **116**, C06019, https://doi.org/10.1029/2010JC006864.

Iskandar, I., Masumoto, Y., Mizuno, K., Sasaki, H., Affandi, A. K., Setiabudidaya, D., & Syamsuddin F., 2014: Coherent intraseasonal oceanic variations in the eastern equatorial Indian Ocean and in the Lombok and Ombai Straits from observations and a high-resolution OGCM, *J. Geophys. Res. Oceans*, **119**, 615–630, https://doi.org/10.1002/2013JC009592.

Ishizaki, H., Nakano, H., Nakano, T., & Shikama, N. (2014), Evidence of equatorial Rossby wave propagation obtained by deep mooring observations in the western Pacific Ocean, *J. Oceanogr.*, **70**(6), 463–488, https://doi.org/10.1007/s10872-014-0247-3.

Johnson, G. C. (2011), Deep signatures of southern tropical Indian Ocean annual Rossby waves, *J. Phys. Oceanogr.*, **41**(10), 1958–1964, https://doi.org/10.1175/JPO-D-11-029.1.

Kessler, W. S., McCreary, J. P. (1993), The annual wind-driven Rossby-wave in the subthermocline equatorial Pacific, *J. Phys. Oceanogr.*, **23**, 1192–1207, https://doi.org/10.1175/1520-0485(1993)023%3c1192:TAWDRW%3e2.0.CO;2.

Khadami, F., Suprijo, T., & Iskandar, I. (2018), Semiannual variation of zonal current along the equatorial Indian Ocean, *IOP Conf. Ser: Earth Environ. Sci.*, **162**, 012015, https://doi.org/10.1088/1755-1315/162/1/012015.

Knox, R. A. (1976), On a long series of measurements of Indian Ocean equatorial currents Near Addu Atoll, *Deep-Sea. Res.*, **23**, 211–221,

https://doi.org/10.1016/0011-7471(76)91325-5.

Kutsuwada, K., McPhaden, M. J. (2002), Intraseasonal variations in the upper equatorial Pacific Ocean prior to and during the 1997–98 El Niño, *J. Phys. Oceanogr.*, **32**, 1133–1149, https://doi.org/10.1175/1520-0485%282002%29032%3c1133%3AIVITUE%3e2.0.CO%3B2.

Large, W. G., Pond, S. (1981), Open ocean momentum flux measurements in moderate to strong winds, *J. Phys. Oceanogr.*, **11**, 324–336, https://doi.org/10.1175/1520-0485(1981)011%3c0324:OOMFMI%3e2.0.CO;2.

Li, Z., Aiki, H. (2020), The life cycle of annual waves in the Indian Ocean as identified by seamless diagnosis of the energy flux, *Geophys. Res. Lett.*, **47**, e2019GL085670, https://doi.org/10.1029/2019GL085670.

Li, Z., Aiki, H., Nagura, M., & Ogata, T. (2021), The vertical structure of annual wave energy flux in the tropical Indian Ocean, *Prog. Earth Planet Sci*, **8**, 43 https://doi.org/10.1186/s40645-021-00432-9.

Longuet-Higgins, H. C. (1964), On group velocity and energy flux in planetary wave motion, *Deep-Sea. Res.*, **11**, 35–42, https://doi.org/10.1016/0011-7471(64)91080-0.

Lu, B., Ren, H., Scaife, A. A., Wu, J., Dunstone, N., Smith D., Wan, J., Eade, R., MacLachlan, C., & Gordon M., (2018), An extreme negative Indian Ocean Dipole event in 2016: dynamics and predictability, *Clim. Dyn.*, **51**, 89–100, https://doi.org/10.1007/s00382-017-3908-2.

Lucas, R., Firing, E. (1985), The annual Rossby wave in the central equatorial Pacific Ocean, *J. Phys. Oceanogr.*, **15**(1), 55–67, https://doi.org/10.1175/1520-0485(1985)015%3c0055:TARWIT%3e2.0.CO;2.

Luyten, J. R., Roemmich, D. H. (1982), Equatorial currents at semiannual period in the Indian-Ocean, *J. Phys. Oceanogr.*, **12**, 406–413,

https://doi.org/10.1175/1520-0485(1985)015%3c0055:TARWIT%3e2.0.CO;2.

Luyten, J. R., Swallow, J. C. (1976), Equatorial undercurrents, *Deep-Sea Res*., **23**, 999–1001, https://doi.org/10.1016/0011-7471(76)90830-5.

Mark, R.J., Huang, B. (2004), The Rossby wave as a key mechanism of Indian Ocean climate variability, *Deep-Sea Res.*, *Part I*, **51**, 2123–2136, https://doi.org/10.1016/j.dsr.2004.06.005.

Masumoto, Y. et al. (2004), A fifty-year eddy-resolving simulation of the world ocean: Preliminary outcomes of OFES (OGCM for the Earth Simulator), *J. Earth Simulator*, **1**, 35–56.

Matsuno, T. (1966), Quasi-geostrophic motions in the equatorial area, *J. Meteo. Soc. Japan*, **44**, 25–43, https://doi.org/10.2151/jmsj1965.44.1_25.

McCreary, J. P. (1984), Equatorial beams, *J. Mar. Res.*, **42**, 395–430, https://doi.org/10.1357/002224084788502792.

McPhaden, M. J. (1982), Variability in the central equatorial Indian-Ocean. I: Ocean Dynamics, *J. Mar. Res.*, **40**, 157–176.

McPhaden, M. J., Nagura, M. (2014), Indian Ocean dipole interpreted in terms of recharge oscillator theory, *Climate Dyn*., **42**, 1569–1586, https://link.springer.com/article/10.1007%2Fs00382-013-1765-1.

McPhaden, M. J., Ripa, P. (1990), Wave-mean flow interactions in the equatorial ocean, *Annu. Rev. Fluid Mech.*, **20**, 167–205, https://doi.org/10.1146/annurev.fl.22.010190.001123.

Miyama, T., McCreary, J. P., Sengupta, D., & Senan, R. (2006), Dynamics of biweekly oscillations in the equatorial Indian Ocean, *J. Phys. Oceanogr.*, **36**, 827–846, https://doi.org/10.1175/JPO2897.1.

Nagura, M., Masumoto, Y. (2015), A Wake due to the Maldives in the Eastward Wyrtki Jet,

J. Phys. Oceanogr., **45**(7), 1858–1876, https://doi.org/10.1175/JPO-D-14-0191.1.

Nagura, M., McPhaden, M. J. (2010a), Wyrtki Jet dynamics: Seasonal variability, *J. Geophys. Res.*, **115**, C07009, https://doi.org/10.1175/JPO-D-14-0191.1.

Nagura, M., McPhaden, M. J. (2010b), Dynamics of zonal current variations associated with the Indian Ocean dipole, *J. Geophys. Res.*, **115**, C11026, https://doi.org/10.1029/2010JC006423.

Nagura, M., McPhaden, M. J. (2016), Zonal propagation of near-surface zonal currents in relation to surface wind forcing in the equatorial Indian Ocean, *J. Phys. Oceanogr.*, **46**, 3623–3638, https://doi.org/10.1175/JPO-D-14-0191.1.

Nagura, M. (2018), Annual Rossby waves below the pycnocline in the Indian Ocean, *J. Geophys. Res.*, **123**, 9405–9415, https://doi.org/10.1029/2018jc014362.

Ogata, T., Aiki, H. (2019) The pathway of intraseasonal wave energy in the tropical Indian Ocean as identified by a seamless diagnostic scheme, *SOLA*, **15**, 262–267, https://doi.org/10.2151/sola.2019-047.

Orlanski, I., Sheldon, J. (1993), A case of downstream baroclinic development over western north America, *Mon. Wea. Rev.*, **121**, 2929–2950, https://doi.org/10.1175/1520-0493(1993)121%3C2929:ACODBD%3E2.0.CO;2.

Philander, S. G. H. (1989), El Niño, La Niña, and the Southern Oscillation, *Academic Press*, *London*.

Polito, P. S., Liu, W. T. (2003), Global characterization of Rossby waves at several spectral bands, *J. Phys. Oceanogr.*, **108**, https://doi.org/10.1029/2000JC000607.

Pujiana, K., McPhaden, M. J. (2020), Intraseasonal Kelvin waves in the equatorial Indian Ocean and their propagation into the Indonesian seas, *J. Geophys. Res.*, **125**, e2019JC015839, https://doi.org/10.1029/2019JC015839.

Qiu, Y., Li, L., & Yu, W. (2009), Behavior of the Wyrtki Jet observed with surface drifting

buoys and satellite altimeter, *Geophys. Res. Lett*., **36**, L18607, https://doi.org/10.1029/2009GL039120.

Rahul, P. C. R., Salvekar, P. S., Deo, A. A., & Ganer, D. W. (2004), Westward propagating twin gyres in the equatorial Indian Ocean, *Geophys. Res. Lett.*, **31**, L01304, https://doi.org/10.1029/2003GL018615.

Rao, S. A., Behera, S. K., Masumoto, Y., & Yamagata, T. (2002), Interannual subsurface variability in the tropical Indian Ocean with a special emphasis on the Indian Ocean dipole, *Deep-Sea Res.*, *Part II: Topical Studies in Oceanography*, **49**, 1549–1572, https://doi.org/10.1016/S0967-0645(01)00158-8.

Rao, S. A., Yamagata, T. (2004), Abrupt termination of Indian Ocean dipole events in response to intra-seasonal oscillations, *Geophys. Res. Lett.*, **31**, L19306, https://doi.org/10.1029/2004GL020842.

Rao, R. R., Girish, Kumar, M. S., Ravichandran, M., Rao, A. R., Gopalakrishna, V. V., & Thadathil, P. (2010), Interannual variability of Kelvin wave propagation in the wave guides of the equatorial Indian Ocean, the coastal Bay of Bengal and the southeastern Arabian Sea during 1993–2006, *Deep-Sea Res.*, *Part I*, **57**, 1–13, https://doi.org/10.1016/j.dsr.2009.10.008.

Reppin, J., Schott, F. A., & Quadfasel, D. (1999), Equatorial currents and transports in the upper central Indian Ocean: Annual cycle and interannual variability, *J. Geophys. Res.*, *Oceans*, **104**(C7), 15495–15514, https://doi.org/10.1029/1999JC900093.

Rothstein, L. M., Moore, D. W., & McCreary, J. P. (1985), Interior reflections of a periodically forced equatorial Kelvin wave, *J. Phys. Oceanogr.*, **15**(7), 985–996, https://doi.org/10.1175/1520-0485(1985)015%3c0985:IROAPF%3e2.0.CO;2.

Saji, N. H., Goswami, B. N., Vinayachandran, P. N., & Yamagata, T. (1999), A dipole mode in the tropical Indian Ocean, *Nature*, **401**, 360–363, https://doi.org/10.1038/43854.

Saji, N. H., Yamagata, T. (2003), Structure of SST and Surface Wind Variability during Indian Ocean Dipole Mode Events: COADS Observations, *J. Clim.*, **16**, 2735–2751, https://doi.org/10.1175/1520-0442(2003)016<2735:SOSASW>2.0.CO;2.

Schopf, P. S., Anderson, D. L. T., Smith, R. (1981), Beta-dispersion of low-frequency Rossby waves, *Dyn. Atmos. Oceans*, **5**, 187–214, https://doi.org/10.1016/0377-0265(81)90011-7.

Song, Q., Aiki, H. (2020), The climatological horizontal pattern of energy flux in the tropical Atlantic as identified by a unified diagnosis for Rossby and Kelvin waves, *J. Geophys. Res.*, **125**, e2019JC015407, https://doi.org/10.1029/2019JC015407.

Song, Q., Aiki, H. (2021), Horizontal energy flux of wind-driven intraseasonal waves in the tropical Atlantic by a unified diagnosis, *J. Phys. Oceanogr.*, **51**(9), 3037–3050 https://doi.org/10.1175/JPO-D-20-0262.1.

Schott, F. (1986), Seasonal variation of cross-equatorial flow in the Somali Current, *J. Geophys. Res.*, **91**, 10581-10584, https://doi.org/10.1029/JC091iC09p10581.

Schott, F. A., McCreary, J. P. (2001), The monsoon circulation of the Indian Ocean, *Prog. Oceanogr.*, **51**, 1–123, https://doi.org/10.1016/S0079-6611(01)00083-0.

Schopf, P. S., Anderson, D. L. T., & Smith, R. (1981), Beta-dispersion of low-frequency Rossby waves, *Dyn. Atmos. Oceans*, **5**, 187–214, https://doi.org/10.1016/0377-0265(81)90011-7.

Smagorinsky, J., Manabe, S., & Holloway, J. L. (1965), Numerical results from a nine-level general circulation model of the atmosphere, *Mon. Wea. Rev.*, **93**, 727–768, https://doi.org/10.1175/1520-0493(1965)093%3c0727:NRFANL%3e2.3.CO;2.

Swallow, J. C., Schott, F., & Fieux, M. (1991), Structure and transport of the East African Coastal Current, *J. Geophys. Res.*, **96**, 22254–22267, https://doi.org/10.1029/91JC01942.

Tailleux, R., McWilliams, J. C. (2001), The effect of bottom pressure decoupling on the speed of extratropical, baroclinic Rossby waves, *J. Phys. Oceanogr.*, **31**, 1461–1476, https://doi.org/10.1175/1520-0485(2001)031%3C1461:TEOBPD%3E2.0.CO;2.

Tanizaki, C., Tozuka, T., Doi, T., & Yamagata, T. (2017), Relative importance of the processes contributing to the development of SST anomalies in the eastern pole of the Indian Ocean Dipole and its implication for predictability, *Clim. Dyn*., **49**, 1289–1304, https://doi/org/10.1007/s00382-016-3382-2.

Tailleux, R., McWilliams, J. C. (2001), The effect of bottom pressure decoupling on the speed of extratropical, baroclinic Rossby waves, *J. Phys. Oceanogr.*, **31**, 1461–1476, https://doi.org/10.1175/1520-0485(2001)031<1461:TEOBPD>2.0.CO;2.

Thierry, V., Mercier, H., Treguier, A. M. (2006), Seasonal fluctuations in the deep central equatorial Atlantic Ocean: A data-model comparison, *Ocean Dyn.*, **56**(5–6), 581–593, https://doi.org/10.1007/s10236-005-0045-y.

Toyoda, T., Nakano, H., Aiki, H., Ogata, T., Fukutomi, Y., Kanno, Y., Urakawa, L. S., Sakamoto, K., Yamanaka, G., & Nagura, M. (2021), Energy flow diagnosis of ENSO from an ocean reanalysis, *J. Clim.*, **34**(10), 4023–4042, https://doi.org/10.1175/JCLI-D-20-0704.1.

Ummenhofer, C. C., Biastoch, A., & Böning, C. W. (2017), Multidecadal Indian Ocean variability to the Pacific and implications for preconditioning Indian Ocean dipole events, *J. Clim.*, **30**(5), 1739–1751, https://doi.org/10.1175/JCLI-D-16-0200.1.

Vergara, O., Dewitte, B., Ramos, M., & Pizarro, O. (2017), Vertical energy flux at ENSO time scales in the subthermocline of the southeastern Pacific, *J. Geophys. Res. Oceans*, **122**, 6011–6038, https://doi.org/10.1002/2016JC012614.

Vinayachandran, P. N., Saji, N. H. & Yamagata, T. (1999), Response of the equatorial Indian Ocean to an unusual wind event during 1994, *Geophys. Res. Lett.*, **26**, 1613–1616.

https://doi.org/10.1029/1999GL900179.

Vinayachandran, P. N., Iizuka, S., & Yamagata, T. (2001), Indian Ocean dipole mode events in an ocean General Circulation model, *Deep-Sea Res.*, *Part II*, **49**(7), 1573–1596, https://doi.org/10.1016/S0967-0645(01)00157-6.

Wang, G., Cai, W. (2020), Two-year consecutive concurrences of positive Indian Ocean Dipole and Central Pacific El Niño preconditioned the 2019/2020 Australian "black summer" bushfires, *Geosci. Lett.*, **7**(19), https://doi.org/10.1186/s40562-020-00168-2.

Webster, P. J., Moore, A. M., Loschnigg, J. P., & Leben, R. R. (1999), Coupled oceanic-atmospheric dynamics in the Indian Ocean during 1997-98, *Nature*, **401**, 356–360, https://www.nature.com/articles/43848.

Wyrtki, K. (1973), An equatorial jet in the Indian Ocean, *Scienc*e, **181**, 262–264, http://dx.doi.org/10.1126/science.181.4096.262.

Yamagata, T., Behera, S. K., Luo, J. J., Masson, S., Jury, M. R., & Rao, S. A., (2004), Coupled ocean-atmosphere variability in the tropical Indian Ocean, *Earth's Climate: The Ocean–Atmosphere Interaction*, *Geophys. Monogr*, **147**, 189–212, https://doi.org/10.1029/147GM12.

Yan, D., Liu, K., Zhuang, W., & Yu, W. (2012), The Kelvin wave processes in the equatorial Indian Ocean during the 2006–2008 IOD events, *Atmos. Ocean. Sci. Lett.*, **5**, 324–328, https://doi.org/10.1080/16742834.2012.11447007.

Yanai, M., Maruyama, T. (1966), Stratospheric wave disturbances propagating over the equatorial Pacific, *J. Met. Soc. Japan*, **44**, 291–294. https://doi.org/10.2151/jmsj1965.44.5_291.

Yu, X., McPhaden, M. J. (1999), Seasonal variability in the equatorial Pacific, *J. Phys. Oceanogr.*, **29**, 925–947. https://doi.org/10.1175/1520-0485(1999)029%3c0925:SVITEP%3e2.0.CO;2.

Yu, L., O'Brien, J.J., & Yang, J. (1991), On the remote forcing of the circulation in the Bay of Bengal, *J. Geophys. Res.*, **96** (C11), 20449–20454, https://doi.org/10.1029/91JC02424.

Yuan, D., Han, W. (2006), Roles of equatorial waves and western boundary reflection in the seasonal circulation of the equatorial Indian Ocean, *J. Phys. Oceanogr.*, **36**, 930–944, https://doi.org/10.1175/JPO2905.1.

Yuan, D., Liu, H. (2008) Long-wave dynamics of sea level variations during Indian Ocean Dipole events, *J. Phys. Oceanogr.*, **39**, 1115–1132, https://doi.org/10.1175/2008JPO3900.1.

Zanowski, H., Johnson, G. C. (2019), Semiannual variations in 1,000-dbar equatorial Indian Ocean velocity and isotherm displacements from Argo data, *J. Geophys. Res. Oceans*, **124**, https://doi.org/10.1029/2019JC015342.

Acknowledgements

Upon the completion of my doctor course, I am grateful to those who have offered me encouragement and support during the life of my PhD period in Nagoya University, Japan.

First of all, the profound gratitude should go to my supervisor Professor Hidenori Aiki. He has given me great instruction and encouragements throughout the process of selecting the research topic, writing the thesis, improving the outline and the argumentation, and correcting the grammatical errors. His insightful comments on every draft, which provide me with many enlightening ideas, have inspired me to a great extent. I could not finish the PhD course without his patient guidance.

Secondly, I want to express my heartfelt thanks to all the teachers who have helped and taught me in this university. I am particularly grateful to Professors Joji Ishizaka, Tetsuya Hiyama, Kengo Sudo, Drs. Takanori Horii, Yoshihisa Mino, Motoki Nagura, Tomomichi Ogata, Yoshiki Fukutomi. Their courses and comments have broadened my horizon and aroused my interest in oceanography.

I also want to thank all the members in the Graduate school of Environmental Studies at the Hydrospheric Atmospheric Research Center of Nagoya University, including Qingyang Song, Yuanli Zhu, Qian Xu, Jutarak Luang-on, Chi Feng, Phattaranakorn Nakornsantiphap, Yifan Zhang, Yifei Wu, Dudsadee Leenawarat, Tokahiro Shimura, Kohei Kameyama, Yuri Kase, Zhenjia Zhou, Yingnan Jiang, Kaiwen Ye, Borui Wu, Muyan Jiang, Haoran Zhang, who once offered me valuable advice and cooperation and inspired me in the entire process of my PhD course. Also, I thank Mrs. Niizuma for taking care of all students very well.

Besides, I am indebted to my parents for supporting me to do whatever I want to and gives me their loving considerations, great confidence and supports me without a word of complaint. I also need to express my gratitude to all my friends. Love you all.

Appendices

1. The life cycle of annual waves in the Indian Ocean as identified by Seamless diagnosis of the energy flux.

Authors: **Z. Li**, H. Aiki

Published in: *Geophysical Research Letters (2020)*, **47**, e2019GL085670,

https://doi.org/10.1029/2019GL085670.

2. The vertical structure of annual wave energy flux in the tropical Indian Ocean.

Authors: **Z. Li**, H. Aiki, M. Nagura, and T. Ogata

Published in: *Progress in Earth and Planetary Science (2021)*, **8**, 43,

https://doi.org/10.1186/s40645-021-00432-9.

3. The 1994 positive Indian Ocean Dipole event as investigated by the transfer routes of oceanic wave energy.

Authors: **Z. Li**, H. Aiki

Published in: *Journal of Physical Oceanography (2022)*, **52**, 459–473,

https://doi.org/10.1175/JPO-D-21-0189.1.